LARGE EDDY SIMULATIONS OF TURBULENT FLAME DEFLAGRATION WITH WALL INTERACTIONS

Vendra Chandra Madhav Rao

THESIS SUBMITTED FOR THE DEGREE OF
DOCTOR OF PHILOSOPHY

FACULTY OF SCIENCE, ENGINEERING AND COMPUTING

KINGSTON UNIVERSITY LONDON

Kingston University
Faculty of Science, Engineering and Computing

PhD Thesis

Academic Year : 2010-2014

Vendra Chandra Madhav Rao

LARGE EDDY SIMUALTION OF TURBULENT FLAME DEFLAGRATION WITH WALL INTERACTIONS

Supervisors :
External
Prof. Jennifer X. Wen
Prof. Kai H. Luo

Internal
Dr. Siaka Dembele
Dr. Baopeng Xu

This thesis is submitted in partial fulfilment of the requirements for the degree of Doctor of Philosophy

Abstract

Large Eddy Simulation (LES) are performed for premixed gas phase turbulent deflagrations in confinements with particular modeling emphasis to capture proper flame behaviour i.e. quenching and acceleration near the obstacles/solid surfaces. Flamelet based Coherent Flame Model (CFM) is adopted for simulating turbulent flame deflagration. Conservation equation for Flame Surface Density (FSD) is considered to account for the non-equilibrium transport of FSD. Modeling improvements in terms of flow-wall and flame-wall interactions are implemented in the governing equations of CFM, which serve as wall boundary closures for numerical combustion simulations with wall interactions. The enthalpy loss factor considering the non-isobaric condition is used in the present study to accurately capture the region where flame is affected by the presence of wall. Model constants for the flame-wall interaction are determined in a posteriori test. The CFM solver along with flow and flame-wall interactions is been developed in OpenFOAM framework. The solver has been first validated for a non-reacting channel flow simulations with the DNS data. Validation study for the flow-wall interaction is performed by considering the periodic hill configuration in a channel. DNS of a 'V'-flame in a channel flow is used as posteriori test to fix the flame-wall model constants. The numerical predictions of the CFM solver with wall interactions are assessed by simulating the turbulent flame deflagrations in a quench mesh, repeated obstructed channel and in a model hydrogen storage facility. Numerical results establish that the wall interaction models have improved the predictions and are able to account for change in characteristics of the turbulent premixed flame and turbulence length scales in the near-wall region.

to my parents

Acknowledgements

I wish to express my sincere gratitude to my supervisors Prof. Jennifer Wen and Prof. Kai H. Luo for all their guidance and support bestowed to me. Project related discussions with both the Professors were always enlightening and their systematic approach of tackling a problem was remarkable.

I profoundly thank Dr Siaka Dembele and Dr. Baopeng Xu for accepting to be my supervisors, after change in University of my initial supervisory team and for extending their help and advice in completing this thesis.

I also wish to express my sincere gratitude to Prof. T. Sundararajan (IIT Madras), Dr. P. K. Sinha (CDAC), Late Dr. T. Sundararajan (CDAC) for their sincere advice, support and for the encouragement bestowed upon me to pursue my PhD studies.

I would also like to thank my friends and colleagues in the research office at Kingston University for being very friendly and making my stay in the office a memorable one.

I'm also thankful to Ms. Jackie Deacon and the HPC staff at Kingston University and University of Southampton for their kind help in resolving any issues, I had in their purview.

Finally I would like to thank very special people in my life, my parents, wife, sister and brothers for their unconditional affection and support rendered to me during the course of this study and for always.

List of Publications

The work presented in this thesis is discussed in the following publications,

Wen, J. X., Heidari, A., Madhav Rao, V. C., Ferraris, S. A. and Tam, V. H. Y., " Simulating Flame Propagation in Obstructed Channels with OpenFoam", 6th International Seminar on Fire and Explosion Hazards , 11-16 April, 2010, Leeds, UK

V. C. Madhav Rao, J. Wen, V.H.Y. Tam, Numerical simulation of Turbulent Flame-Wall Quenching using Coherent Flame Model, 8th International Symposium on Hazards, Prevention and Mitigation of Industrial Explosions, 5-10 Sept, 2010, Yokohama, Japan.

V. C. Madhav Rao, J. X. Wen, K. H. Luo, "Large Eddy Simulation of Flamelet-Wall interaction in Combustion", 5th European Combustion Meeting, 28 June - 1 July, 2011, Cardiff, UK.

V. C. Madhav Rao, J. Wen, V.H.Y. Tam, Numerical simulation of turbulent flame-wall quenching using coherent flame model, Work in Progress Poster Presentation, 33rd International Symposium on Combustion, 1-6 Aug, 2010, Beijing, China.

V. C. Madhav Rao, J. Wen, V. H. Y. Tam, Large Eddy Simulation of Turbulent Combustion using Coherent Flame Model, Poster presentation, 34th IFRF Topic Oriented Technical Meeting, Cardiff University, 20-21, Oct, 2010

V. C. Madhav Rao, J. Wen, V.H.Y. Tam, Numerical Simulation of turbulent Flame-Wall Quenching using Coherent Flame Model, Work in Progress Presentation, 2nd FM Global Open Source CFD Fire Modeling Workshop, Norwood MA, USA, 29-30 Apr, 2010.

V C Madhav Rao, Wen J X, Tam V H Y, 'Numerical simulation of turbulent flame-wall quenching using a coherent flame model', Journal of Loss prevention in the process industries, 10.1016/j.jlp.2012.04.001, May, 2012.

V. C. Madhav Rao, J. Wen, K. H. Luo, Compressible channel flow simulation using the LES solver in OpenFOAM, Oral presentation , UK Turbulence Consortium Annual Review, 3-4 Sept, 2012, Lancaster University, UK.

Contents

List of Figures

List of Tables

NOMENCLATURE

y^+ - Nondimensional distance from the wall

l_t - Integral length scale

ν - Kinematic viscosity (m^2/s)

Re_t - Turbulent Reynolds number

Re_τ - Friction Reynolds number

Re_Δ - Subgrid scale turbulent Reynolds number

u' - rms turbulent fluctuation velocity (m/s)

ε - Rate of kinetic energy dissipation

k - Kinetic energy

η_k - Kolmogorov length scale

t_k - Kolmogorov time scale

u_k - Kolmogorov velocity

Ma - Mach number

c - Speed of sound

ρ - Density (kg / m^3)

g - Acceleration due to gravity (m^2/s)

p - Pressure (N/m^2)

h - Total enthalpy (kJ/kg)

C_p - Specific heat at constant pressure (kJ/kg K)

R - Universal gas constant (kJ/kg K)

$\bar{\Delta}$ - Subgrid filter size

k_{sgs} - Subgrid kinetic energy

μ_{sgs} - Subgrid viscosity

τ_{ij}^{sgs} - Subgrid stress tensor

π - Hydrodynamic pressure

p_0 - Thermodynamic pressure

δ_{ij} - Kronecker delta

U - Mean velocity (m/s)

T - Temperature (K)

γ - Ratio of specific heats

ϕ - Scalar, equivalence ratio

u_τ - Shear velocity or friction velocity (m/s)

τ_w - Wall shear stress

H – Half channel height (m)

u^+ - Nondimensional velocity

S_l - Unstretched laminar flame speed (m/s)

δ_v - Viscous length scale

Σ - Flame surface area per unit volume – flame surface density

Δh_f^o - Enthalpy of formation (kJ/kg)

Pe - Peclet number

Da -Damköhler number

Ka - Karlovitz number

Acronyms

CFD	Computational fluid dynamics
CFM	Coherent flame model
LES	Large eddy simulations
RANS	Reynolds averaged Navier-Stokes equations
DNS	Direct numerical simulation
BR	Blockage ratio

Chapter 1

INTRODUCTION

1.1 Turbulent combustion

Combustion process is a chemical reaction between fuel and oxidizer releasing heat and combustion byproducts. The primary classification of the combustion process interms of fuel and oxidizer mixing are as premixed, Non-premixed and partially premixed. In premixed mode of combustion, the fuel and oxidizer (together known as reactants) are homogenously mixed well ahead of the combustion zone. Premixed flames propagate towards the fresh mixture with finite velocity termed as burning velocity. In non-premixed mode, the fuel and oxidizer are introduced separately to the combustion zone. The mixing of fuel and oxidizer happens only due to turbulence and diffusion process and the flame tend to stabilize at the interface zone between the fuel and oxidizer streams. When combustion happens between fuels and oxidizer in both premixed and non-premixed mode then it is termed as partially premixed. Non-premixed flame are easy to control by controlling the mixing between the fuel and oxidizer, whereas premixed flames are difficult to control due to their propagating nature.

Combustion processes are further termed as laminar or turbulent combustion based on the characteristics of flow field entering the flame front. Turbulent combustion is encountered in most practical combustion systems such as internal combustion, aircraft engines, industrial burners and furnaces

etc while combustion happening in laminar flows are almost limited to candles, lighters and some domestic furnaces. Turbulent combustion results from the two-way interaction of chemistry and turbulence. When a flame interacts with a turbulent flow, turbulence is modified by combustion because of the strong flow accelerations through the flame front induced by heat release and because of the large changes in kinematic viscosity associated with temperature changes. This mechanism may generate turbulence, called "flame-generated turbulence" or damp it. On the other hand, turbulence alters the flame structure, which may enhance the chemical reaction but also in extreme cases completely inhibit it, leading to flame quenching.

In a premixed cloud the flame can propagate in two different modes through the flammable part of the cloud namely deflagration and detonation. Deflagration is subsonic premixed flame propagations, most common mode of premixed flame propagation (Muckett and Furness, 2007, Sehgal, 2012). The flame propagates by the heat and mass transfer mechanism with pressure wave propagating ahead of the flame front. When the flame propagation speeds are close to sonic speeds, they are termed as fast deflagrations (sonic speed is referred as speed of sound in that medium). Detonations are supersonic premixed flame propagations associated with shock waves. The unburnt mixture is heated by the coupled flame front - shock wave to ignition. The maximum pressure caused by the deflagration is normally limited to the adiabatic constant-volume combustion (AICC) pressure, where as detonation leads to spatially non-uniform pressure that are well in excess of AICC pressures.

Numerical simulations of turbulent reacting flows remain complex and challenging problem as,

- Combustion, even without turbulence is an intrinsically complex process involving a large range of chemical time and length scales. Some of the chemical phenomena controlling flames take place in short times over thin layers and are associated with very large mass fractions, temperature and density gradients.
- Turbulence itself is probably the complex phenomenon in non-reacting fluid mechanics. Various time and length scales are involved and the structure and the description of turbulence remain open questions modeling (Poinsot and Veynante, 2005).

In an accidental/uncontrolled gas explosion scenario of a hydrocarbon-air cloud ignited by a weak source, the flame will normally start out as a slow laminar flame. If the cloud is unconfined and unobstructed (i.e. no equipment or other structures are engulfed by the vapour cloud), the flame is not likely to accelerate and the overpressure (pressures in excess of atmospheric pressure) will be negligible. But in case of confined or with obstacles, the laminar flame will accelerate and transit into a turbulent deflagration (i.e. turbulent flame), as the flow field ahead of the flame front becomes turbulent. The turbulence is caused by the interaction of the flow field with process equipment, piping, structures etc. This turbulent flame can propagate either in deflagration or as detonation in the remaining flammable parts of the cloud, accordingly generating higher overpressures (Bjerketvedt et al., 1997). These overpressures above critical limits cause catastrophic damage to both humans and infrastructure lying with in the vicinity.

1.2 Computational Fluid dynamics

Computational fluid dynamics (CFD) in the field of combustion physics is an emerging numerical technique to obtain detailed analysis of the flame propagation and to predict the consequences of combustion processes. CFD involves numerical evaluation of the partial differential equations governing the fluid flow and combustion process and yield a great deal of information about the flow variables. However, accuracy and reliability of these predictions greatly depend on the employed modeling assumptions and numerics. Classical way of understanding a phenomenon or designing a product through experiments is often time consuming and costly. CFD greatly aided in reducing the number of experimental trials, but cannot replace experiments on whole as predictions still rely on experiments for validations and fine tuning of the numerical models.

Given a problem in CFD, the governing equations can be solved at three levels based on the information required and tradeoffs to computational cost : a) Direct numerical simulations (DNS) b) Large Eddy Simulation (LES) and c) Reynolds Averaged Navier-stokes simulations (RANS). In terms of computation cost, DNS is most expensive - currently limited to few ideal cases, RANS is less compute intensive - details of the flow variables is also limited to mean quantities. LES lies in-between DNS and RANS, with current available computational resources LES can be used for solving industrial problems to a reasonable accuracy levels. The scope of CFD applications is enhanced with the aid of High performance computing (cluster of computing resources with high speed interconnectivity) by enabling large scale simulations which were previously intractable.

1.3 About OpenFOAM

OpenFoam is an open source (FOAM - Field Operation and Manipulation) toolkit to solve continuum mechanics problems. OpenFOAM is written in C++ programming language (Object oriented programming concept) in modules of shared and dynamic libraries, which can then be included/called in an appropriate computer program to form a numerical solver, to solve a particular set of physics like, reacting flows, multiphase flows and so on. Model implementation in present thesis is carried out in OpenFOAM framework leading to development of a new solver based on Coherent Flame Model to solve premixed flame deflagrations.

1.4 Motivation and objective

The turbulent combustion models tend to give better numerical predictions of flame propagations in the region away from the wall boundary, but in common produce nonphysical predictions within the near wall region. The reason being, the turbulent combustion models are often conceptualised based on isotropic turbulence and adiabatic conditions, while in near wall region turbulence quantities are highly anisotropic and flame quenching and heat loss to wall make it nonadiabatic.

The flame-wall interactions (wall effects) become much more important in applications, where flame propagations are in confinements, for instance in Internal combustion engines, gas turbine combustion chambers and flame interaction with obstacles, necessitates additional/modeling corrections to the turbulent combustion models in the near wall region. A proper approach to incorporate wall effects in the turbulent combustion models will be to modify

models near wall using physical arguments and improving the turbulence modeling itself. The Large Eddy Simulation (LES) offers an improved representation of turbulence and the resulting turbulence-flame interaction with respect to classical Reynolds-Averaged Navier-Stokes approaches. Although large eddy simulation of non-reacting flows is somewhat well established, but is still an emerging tool in numerical combustion domain.

The primary goal of this thesis is to develop an improved LES premixed combustion modeling for numerical simulation of gas phase turbulent deflagrations in confinements. The modeling emphasis is particularly on predicting the proper flame behaviour i.e. quenching and acceleration near the obstacles/solid surfaces.

The main objectives of this thesis are summarised as below:

- To develop an LES Coherent Flame Model solver in OpenFOAM framework.
- Provide appropriate Flow-Wall and Flame-Wall interaction models to improve the accuracy of the combustion model in predicting proper flame behaviours near solid walls/obstacles (i.e. flame quenching and acceleration).
- To compare the numerical results of combustion LES with wall interaction to the available experiments for validation studies.
- To make numerical predictions of turbulent flame deflagrations in realistic scenarios.

1.5 Outline of thesis

Following is the brief outline of this thesis, Chapter-2 provides details about numerical turbulence modeling, in particular about Large Eddy Simulation and the Favre-filtered governing equations describing them for compressible reacting flows. Chapter-3 presents the modeling strategies for premixed combustion and more in detail about the Coherent Flame Model formulation in LES context. Chapter-4 presents the Flow-wall modeling in LES and suitability of a particular model to use in the present study. Chapter-5 discusses about the need for the Flame-wall interaction modeling and details of the proposed model for Coherent flame Model in LES method. The numerical simulation results of flame acceleration in quench mesh, purpose built obstructed chamber experiment and hydrogen storage facility are presented to assess the CFM-LES predictions in Chapter-6. The last Chapter-7 deals with conclusions from the present research work and suggestions for likely areas to further the present studies.

Chapter 2

TURBULENCE MODELING

2.1 Introduction

Turbulent flows are very common in many engineering applications. Understanding, controlling and quantifying the turbulence quantities is of crucial importance for improving system efficiency and safety and therefore remains a grand challenge for scientists and engineers. Turbulence is a continuum phenomenon and is intrinsically three-dimensional. It's difficult to provide a unique definition to turbulent flows and hence the usual practice is to describe it in terms of the flow characteristics. Turbulent flows are characterized by irregularities, flow randomness, diffusive and dissipative. Turbulent flow is rotational containing vortices and eddies of different sizes, which continuously change in time and space. These vortices and eddies evolve, stretch, deform and breakup in the fluid flow and are responsible for the high levels of mixing, diffusion of mass and dissipation of heat in turbulent flows. Turbulent flows occur at high Reynolds numbers and depend on flow configuration. The Reynolds number (Re) is a nondimensional number representing the ratio of inertial forces to viscous forces in a given flow condition.

$$\mathrm{Re} = \frac{inertial\ forces}{viscous\ forces} = \frac{\rho U^2 L^2}{\mu UL} = \frac{UL}{\upsilon} \qquad (2.1)$$

where, U is characteristic velocity scale, L is characteristic length scale and υ is kinematic viscosity of the fluid. Turbulence is characterized by fluctuations of all local flow properties. Any fluid property f, is usually split into mean ($\bar{f}$) and fluctuating (f') contributions. The turbulence strength is generally mentioned in terms of the turbulence intensity parameter 'I' which is the ratio between the root mean square of the fluctuations 'f'' and the mean value $\bar{f}$.

The outline of this chapter is following, section 2.2 discuss about the length and time scales of turbulent motion. The numerical turbulent modeling strategies for solving turbulent flows are presented in section 2.3. LES computational method is been adopted in the present study to simulate the turbulent flows. The description about the LES method and filtering is presented in section 2.4. The LES governing equations are presented in all Mach and low Mach number approximation in section 2.5. The modeling of physical properties in the LES solver is presented in section 2.6 and 2.7. The boundary conditions in LES context are presented in section 2.8. The solution method to handle the pressure velocity coupling is discussed in section 2.9. The validation study of governing equations and numerics for LES simulation are given in section 2.10. The final section 2.11 summarizes the topics presented in this chapter.

2.2 Scales of turbulent motion

Mathematical modeling and quantification of turbulence involves identifying the characteristic length and time scales of the turbulent flows. An 'eddy' is a loose concept that is used when discussing the scales of motion in turbulence

and in particular the swirling structures that can be observed in turbulent flow. If an eddy has length scale l_t and velocity scale u' then its time scale is l_t/u'. This is possibly the only firm property of an eddy. The Reynolds number interms of eddy properties is named as turbulent Reynolds number given as

$$\mathrm{Re}_t = \frac{u' l_t}{\upsilon} \tag{2.2}$$

When Re_t is large, the so called energy–bearing eddies are rather large, most intensive eddies, that are directly generated by shear in the mean flow and are in length scales comparable to the domain size. The largest scales in a turbulent flow are mainly controlled by inertia and are not affected by the viscous dissipation (Poinsot and Veynante, 2005). The kinetic energy in the turbulence is concentrated in these eddies. Since the energy-bearing eddies dominate the influence of the turbulence on the mean flow, the scales u' and l_t are used to characterize these eddies and the turbulence itself. The upper bound to these length scales is determined by the dimensions of the flow geometry. In general, l_t is a bit smaller than these upper bounds. The lower bound to the length scales is set by the influence of viscosity. These small eddies are at the viscous cut-off length scale. The mechanism that is generating the turbulence is putting energy into the eddies with scales u' and l_t, but all the viscous dissipation of the energy is taking place in the small eddies (Poinsot and Veynante, 2005).

Kolmogorov theory (1941) also known as 'K41' for homogenous isotropic turbulence assumes that there is a steady transfer of kinetic energy from large scales to the small scales and this energy is being consumed at

the small scales by viscous dissipation into heat. There is an inertial sub-range where the turbulence generating process is independent of the details of the large scales. The integral length and time scales characterize the largest energy containing eddies in the given flow domain. The energy cascade from one scale to another is constant along the scales and is given by the dissipation rate 'ε' of the kinetic energy 'k'. This dissipation is estimated as the ratio of the kinetic energy $u'^2(r)$ divided by the time scale $r/u'(r)$, where r is the characteristic size of the eddy.

$$\varepsilon = \frac{u'^2(r)}{r/u'(r)} = \frac{u'^3}{r} \tag{2.3}$$

The Kolmogorov scale (η_k) are the smallest scale found in the turbulent flow, determined by the viscosity and dissipation rate of turbulent kinetic energy as

$$\eta_k = \left(\frac{\upsilon^3}{\varepsilon}\right)^{1/4} \tag{2.4}$$

accordingly, the Kolmogorov time and velocity scales are defined as

$$t_\eta = \left(\frac{\upsilon}{\varepsilon}\right)^{1/2}, \quad u_\eta = (\upsilon\varepsilon)^{1/4} \tag{2.5}$$

Along the cascade, the Reynolds number $\mathrm{Re}(r)$ goes down from Re_t to values close to unity where inertia and viscous forces balance. Hence Kolmogorov length scale (η_k) corresponds to a unity Reynolds number ($\mathrm{Re}_{\eta_k} = 1$). The ratio of the integral length scale (l_t) to the Kolmogorov length scale (η_k) gives the comparison between the largest and smallest turbulent eddies in a given flow field,

$$\frac{l_t}{\eta_k} = \frac{u'^3/\varepsilon}{(\upsilon^3/\varepsilon)^{1/4}} = \mathrm{Re}_t^{3/4} \tag{2.6}$$

Hence the range of length scales can be estimated using turbulent Reynolds number based on integral length scales. Equation 2.6 also serves as an estimate for requisite computational domain discretisation points. An intermediate scale between the integral and the Kolmogorov scale is named as Taylor length scale λ_t given by the following expression,

$$\lambda_t = \sqrt{15\nu\frac{u'^2}{\varepsilon}} \sim u' t_\eta \tag{2.7}$$

where, the factor 15 originates from consideration for isotropic homogenous turbulence (Peters, 2000). It can be seen that it is proportional to the product of the turnover velocity of the large eddies and the kolmogorov time, therefore λ_t can be interpreted as the distance that a large eddy convects a Kolmogorov eddy during its turnover time t_η.

2.3 Modeling Strategies

The Navier-Stokes equations (NSE) completely describe the turbulent flows. Historically NSE included conservation equations for mass and momentum only. For solving reacting flows, conservation equations for energy and species transport are also required and in general together these equations are called Navier-Stokes equations.

Solving NSE analytically is not possible except for few simplified ideal flows by neglecting some of the terms, due to nonlinear convection term and coupled equations. Computationally is the only means NSE can be solved for any practical flow conditions and can be achieved in mainly three different approaches, namely

- Reynolds Averaged Navier Stokes (RANS) : The governing equation for Reynolds or Favre (mass weighted) averaged quantities are obtained by averaging the instantaneous balance equations. This averaging procedure introduces unclosed quantities that have to be modelled, using turbulent models. Solving these equations provide averaged quantities corresponding to averages over time for stationary mean flows or averages over different realizations (or cycles) for periodic flows.

$$Q=\bar{Q}+Q' \tag{2.8}$$

where, Q is instantaneous field, $\bar{Q}$ is mean field and Q' is fluctuation.

- Large eddy simulations (LES): The balance equations for large eddy simulations are obtained by spatial filtering of the instantaneous balance equations. LES determine the instantaneous position of a "large scale" resolved flow features but a subgrid model is still required to take into account the effects of small turbulent scales (Figure 2.1). Large-eddy simulations are an intermediate tool between DNS and RANS interms of flow variable information and computational cost.

$$Q=Q_{res}+Q_{sgs} \tag{2.9}$$

where, Q is instantaneous field, Q_{res} is resolved field and Q_{sgs} is subgrid field/unresolved field.

- Direct numerical simulations (DNS): The instantaneous Navier-Stokes equations are solved without any model for turbulent motions. All turbulence scales are explicitly determined (Figure 2.2). DNS provides complete information about the instantaneous variables field. With

existing computing resources, DNS methods are mostly limited in terms of parameter range and geometry to academic situations. Most of the computational cost associated with the DNS is spent on resolving the small scale motions. Typically the number of mesh points required in a DNS are in order of ~ $(Re_t)^{9/4}$ for a three dimensional case.

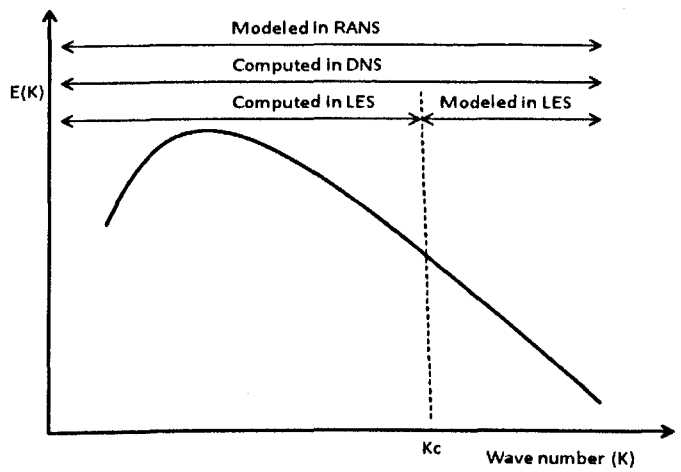

Figure 2.1. Turbulence energy spectrum plotted as a function of wave number in RANS, LES and DNS computations.

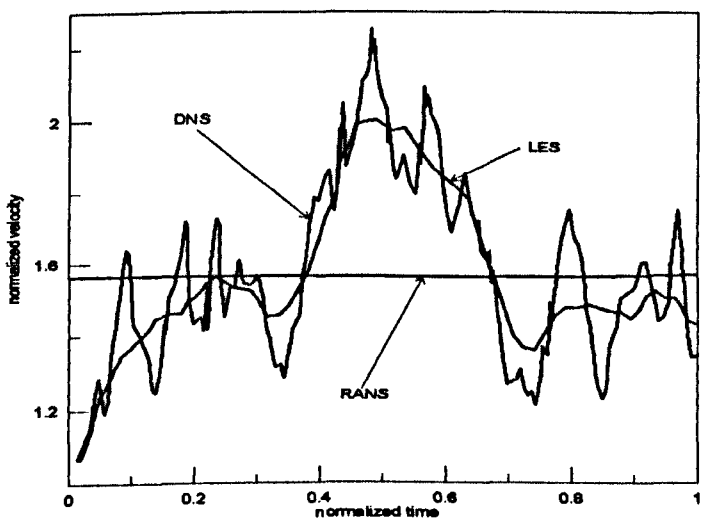

Figure 2.2. Computed field using DNS, LES and RANS methods.

LES approach is been adopted in this thesis to simulate the turbulent flows as this methods provides a better description of turbulent quantities with respect to RANS and is less compute intensive than DNS. Further details of LES method are discussed in the following section.

2.4 Large Eddy Simulation

Large eddy simulation explicitly computes the largest structures of the flow field whereas the effects of the smallest ones are modelled. LES exploits the fact that the large structures in turbulent flows depend on the system geometry whereas small structures are generally assumed to have more universal features. Accordingly, models are probably more suited to describe these small structures. LES can only be used to calculate flow statistics which are essentially determined by the larger scales, such as the mean and second order velocity moments, and often these are quantities required in practice. LES offer access to spatially and temporally dependent flow descriptions, particularly valuable information in complex configurations.

2.4.1 LES filters

The LES filter is low-pass mathematical operation (meaning it filters out the scales associated with high frequencies) intended to remove a range of small scales from the solution to the Navier-Stokes equations. The relevant quantities are filtered in the spectral space or in the physical space. The spatial filtering operation for a flow quantity f is defined in terms of a convolution integral as,

$$\bar{f} = \int f(x')F(x-x')dx' \tag{2.10}$$

where F is the LES filter.

Some of the usual LES filters are listed below :

a) cut-off filter in spectral space

$$F(k) = \begin{cases} 1 & if\ k \le k_c = \pi/\Delta \\ 0 & otherwise \end{cases} \tag{2.11}$$

where k is the spatial wave number. This filter keeps length scales larger than the cut-off length scale 2Δ , where Δ is filter size.

b) Box filter in physical space (moving average or top hat filter)

$$F(x) = F(x_1, x_2, x_3) = \begin{cases} 1/\Delta^3 & if\ |x_i| \le \Delta/2, i = 1,2,3 \\ 0 & otherwise \end{cases} \tag{2.12}$$

where (x_1, x_2, x_3) are spatial coordinates of the location x. This filter corresponds to an average over a cubic box of size Δ.

c) Gaussian filter in physical space

$$F(x) = F(x_1, x_2, x_3) = \left(\frac{6}{\pi\Delta^2}\right)^{3/2} \exp\left[-\frac{6}{\Delta}(x_1^2 + x_2^2 + x_3^2)\right] \tag{2.13}$$

All these filters are normalized, such that

$$\int_{-\infty}^{+\infty}\int_{-\infty}^{+\infty}\int_{-\infty}^{+\infty} F(x_1, x_2, x_3)dx_1dx_2dx_3 = 1 \tag{2.14}$$

For variables density flows, a mass-weighted Favre filtering is used accordingly as,

$$\bar{\rho}\tilde{f}(x) = \int \rho f(x')F(x-x')dx' \tag{2.15}$$

2.5 LES governing equations

Application of the spatial mass weighted filtering procedure to instantaneous Navier-Stokes equations (NSE) results in the Favre-filtered form of the Navier-Stokes equations, governing transport of the mass, momentum, and energy as well as species mass. Favre filter is preferred in compressible flow with density variations to avoid subgrid terms in filtered continuity equations.

In the limit of weak compressibility, the continuity equation becomes extremely stiff necessitating the use of very small time steps. Typically the compressibility effects are negligible if the Mach number (Ma) of the flow is less than 0.3, Mach number (Ma) is a nondimensional number defined as the ratio of flow velocity (U) to the local speed of sound (c), is used in determining if a flow can be treated as compressible,

$$Ma=\frac{U}{c} \tag{2.16}$$

Navier-Stokes equations also fully govern the acoustic wave propagation. In the limits of low velocity flows, the computation time step is restricted by the speed of acoustic waves in the medium (Peric and Ferziger, 2002). The iterative solution method of compressible flows becomes inefficient due to the very small time steps necessary for the tracking of acoustic fluctuations. To overcome this difficulty, one of the methods is to adopt low Mach number approximation of Navier-Stokes equations. In following section the governing equation in LES are presented in both all Mach formulation and low Mach number approximation using index notation, where $x_i (i=1,2,3)$ are Cartesian coordinates and $u_i (i=1, 2,3)$ are Cartesian components of velocity vector u.

2.5.1 All Mach formulation

The conservation of mass yields the continuity equation. $\bar{Q}$ denotes a filtered quantity and $\tilde{Q}$ a mass weighted filtered quantity ($\bar{\rho}\tilde{Q}=\overline{\rho Q}$).

$$\frac{\partial \bar{\rho}}{\partial t}+\frac{\partial}{\partial x_i}(\bar{\rho}\tilde{u}_i)=0 \tag{2.17}$$

The balance of forces corresponds to the so-called momentum equation. It is obtained by equating the acceleration quantity to the body forces plus the surface forces acting upon the external surface of the fluid particle.

$$\frac{\partial \bar{\rho}\tilde{u}_i}{\partial t}+\frac{\partial \bar{\rho}\tilde{u}_j\tilde{u}_i}{\partial x_j}=-\frac{\partial \bar{p}}{\partial x_j}+\frac{\partial}{\partial x_j}\left(\mu_{eff}\frac{\partial \tilde{u}_i}{\partial x_j}\right)+\frac{\partial}{\partial x_j}\left(\mu_{eff}\left(\frac{\partial \tilde{u}_j}{\partial x_i}-\frac{2}{3}\delta_{ij}\frac{\partial \tilde{u}_k}{\partial x_k}\right)\right)+\rho g \tag{2.18}$$

where, the effective dynamic viscosity is given as $\mu_{eff}=\mu_{\text{laminar}}+\mu_{sgs}$

Energy equation (Total enthalpy) is obtained by applying the first principle of thermodynamics to the fluid particle, neglecting radiation heat loss, dissipation by viscous stress and body forces leads to following equation,

$$\frac{\partial \bar{\rho}\tilde{h}}{\partial t}+\frac{\partial \bar{\rho}\tilde{u}_i\tilde{h}}{\partial x_i}=\left(\frac{\partial \bar{p}}{\partial t}+\tilde{u}_i\frac{\partial \bar{p}}{\partial x_i}\right)+\frac{\partial}{\partial x_i}\left(\alpha_{eff}\frac{\partial \tilde{h}}{\partial x_i}\right) \tag{2.19}$$

where, the effective thermal diffusivity is given as $\alpha_{eff}=\alpha_{\text{laminar}}+\alpha_{sgs}$ and total enthalpy is given as sum of chemical and sensible enthalpy

$$h=\Delta h_f^o+\int_{T_0}^{T}Cp(T)\,dT \tag{2.20}$$

Unburnt gas enthalpy equation

$$\frac{\partial \bar{\rho}\tilde{h}_u}{\partial t}+\frac{\partial \bar{\rho}\tilde{u}_i\tilde{h}_u}{\partial x_i}=\left(\frac{\partial \bar{p}}{\partial t}+\tilde{u}_i\frac{\partial \bar{p}}{\partial x_i}\right)\frac{\bar{\rho}}{\bar{\rho}_u}+\frac{\partial}{\partial x_i}\left(\alpha_{eff}\frac{\partial \tilde{h}_u}{\partial x_i}\right) \tag{2.21}$$

To complete the governing equation, it is necessary to introduce an equation

of state relating the density to the pressure. Ideal gas law is been used in the present study.

$$\bar{p} = \bar{\rho} R \tilde{T} \tag{2.22}$$

The closure for subgrid scale viscosity is provided using subgrid scale kinetic energy (k_{sgs}), computed by solving the one equation eddy viscosity model proposed by (Yoshizawa and Horiuti, 1985). A transport equation for subgrid kinetic energy is better suited for non uniform grids and the also accounts for non-equilibrium effects within the source terms. The implementation of this subgrid scale model in OpenFOAM has been already extensively validated by (Fureby et al., 1997).

$$\frac{\partial \bar{\rho} k_{sgs}}{\partial t} + \frac{\partial \bar{\rho} \tilde{u}_i k_{sgs}}{\partial x_j} = \frac{\partial}{\partial x_i}\left(\mu_{eff} \frac{\partial k_{sgs}}{\partial x_i}\right) - \tau_{ij}^{sgs} \frac{\partial \tilde{u}_i}{\partial x_j} - C_e \frac{\bar{\rho} k_{sgs}^{3/2}}{\bar{\Delta}} \tag{2.23}$$

where, the sub-grid stress tensor τ_{ij}^{sgs} is given as

$$\tau_{ij}^{sgs} = \frac{2}{3} k_{sgs} \delta_{ij} - \frac{\mu_{sgs}}{\bar{\rho}}\left(\frac{\partial \tilde{u}_i}{\partial x_j} + \frac{\partial \tilde{u}_j}{\partial x_i} - \frac{2}{3}\delta_{ij} \frac{\partial \tilde{u}_k}{\partial x_k}\right) \tag{2.24}$$

The sub-grid viscosity μ_{sgs} is modelled as

$$\mu_{sgs} = C_k \bar{\rho} k_{sgs}^{1/2} \bar{\Delta}, \tag{2.25}$$

where, $\bar{\Delta} = (\Delta x \Delta y \Delta z)^{1/3}$ is characteristic length scale (Δx, Δy, Δz are mesh size in x, y and z coordinate directions) and model constants are $C_k = 0.094$, $C_e = 1.048$, respectively .

2.5.2 Low Mach formulation

In Low Mach number regime (Ma < 0.3), the local change in density due to pressure influence is negligible. For gas flows involving heat transfer, if the

major contribution of the density change is from the temperature change rather than the pressure change, than such flows also nearly behave as incompressible, hence a Low Mach number approximation can be used in modeling these flow scenarios.

The low Mach number formulation is derived from the compressible flow equations based on asymptotic analysis in the Mach number (Majda and Sethian, 1985, Bell et al., 2007). This analysis leads to a decomposition of the pressure (p) into thermodynamic pressure (p_o) and hydrodynamic pressure (π) with relative magnitude of $p_0/\pi = O(Ma^2)$.

$$p(x,t) = p_0(t) + \pi(x,t) \tag{2.26}$$

Only the thermodynamic pressure appears in the equation of energy and equation of state. The gradient of thermodynamic pressure vanishes, leaving only the gradient of hydrodynamic pressure in the momentum equation. Following are the modifications in the flow governing equations considering the low Mach no. approximation,

Mass

$$\frac{\partial \bar{\rho}}{\partial t} + \frac{\partial}{\partial x_i}(\bar{\rho}\tilde{u}_i) = 0 \tag{2.27}$$

Momentum

$$\frac{\partial \bar{\rho}\tilde{u}_i}{\partial t} + \frac{\partial \bar{\rho}\tilde{u}_j\tilde{u}_i}{\partial x_j} = -\frac{\partial \bar{\pi}}{\partial x_j} + \frac{\partial}{\partial x_j}\left(\mu_{eff}\frac{\partial \tilde{u}_i}{\partial x_j}\right) + \frac{\partial}{\partial x_j}\left(\mu_{eff}\left(\frac{\partial \tilde{u}_j}{\partial x_i} - \frac{2}{3}\delta_{ij}\frac{\partial \tilde{u}_k}{\partial x_k}\right)\right) + \rho g \tag{2.28}$$

Energy equation (Total enthalpy)

$$\frac{\partial \bar{\rho}\tilde{h}}{\partial t} + \frac{\partial \bar{\rho}\tilde{u}_i\tilde{h}}{\partial x_i} = \left(\frac{\partial \bar{p}_0}{\partial t} + \tilde{u}_i\frac{\partial \bar{p}_0}{\partial x_i}\right) + \frac{\partial}{\partial x_i}\left(\alpha_{eff}\frac{\partial \tilde{h}}{\partial x_i}\right) \tag{2.29}$$

Unburnt gas enthalpy equation

$$\frac{\partial \bar{\rho}\tilde{h}_u}{\partial t}+\frac{\partial \bar{\rho}\tilde{u}_i\tilde{h}_u}{\partial x_i}=\left(\frac{\partial \bar{p}_0}{\partial t}+\tilde{u}_i\frac{\partial \bar{p}_0}{\partial x_i}\right)\frac{\bar{\rho}}{\bar{\rho}_u}+\frac{\partial}{\partial x_i}\left(\alpha_{eff}\frac{\partial \tilde{h}_u}{\partial x_i}\right) \tag{2.30}$$

Equation of state

$$\bar{p}_0=\bar{\rho}R\tilde{T} \tag{2.31}$$

The Low Mach approximation decouples the physical acoustic waves from the governing equations and replacing them with a pseudo-acoustic form, the resulting speeds are comparable to the flow velocities (Choi and Merkle, 1993). By modifying the true speed of sound to a lower value, enables the numerical schemes to have much larger timestep still satisfying the numerical stability condition of Courant-Freidrichs-Lewy (CFL) number.

2.6 Sutherland formula

Viscosity is property of a fluid and a strong function of temperature. For liquid, viscosity decreases with increase in temperature but for gases, viscosity increases with increase of temperature. Especially in reacting flows, the change in temperature is large and requires fluid viscosity to be evaluated as a function of temperature. Sutherland's formula is widely accepted correlation given in following forms,

$$\mu=\left(\frac{A_s T^{1/2}}{1+T_s/T}\right) \tag{2.32}$$

where, A_s and T_s are Sutherland coefficient and Sutherland temperature respectively. The typical values used in the present work are listed in the following Table 2.1.

S.No	gas	A_s	T_s
1	Air	1.716 x 10^{-5}	110.4
2	Hydrogen	8.411 X 10^{-7}	273.11
3	Methane	1.20 X 10^{-5}	197.5

Table 2.1. Sutherland's law coefficients

2.7 Thermodynamic properties

The Specific heat at constant pressure (C_p), enthalpy (H) and entropy (S) data for a given fuel-air mixture are computed as a function of temperature (T) using old JANAF tables of thermodynamics (OpenFOAM, 2014) given below,

$$\frac{Cp(T)}{R}=a_0+a_1T+a_2T^2+a_3T^3+a_4T^4 \tag{2.33}$$

$$\frac{H(T)}{RT}=a_0+a_1\frac{T}{2}+a_2\frac{T^2}{3}+a_3\frac{T^3}{4}+a_4\frac{T^4}{5}+\frac{a_5}{T} \tag{2.34}$$

$$\frac{S(T)}{R}=a_0\ln T+a_1T+a_2\frac{T^2}{2}+a_3\frac{T^3}{3}+a_4\frac{T^4}{4}+a_6 \tag{2.35}$$

where $a_0, a_1, a_2, a_3, a_4, a_5$ and a_6 are the numerical coefficients supplied in thermodynamic input files for a specific chemical specie. In the input file following the general convention the seven coefficients are provided in two parts. The first part corresponds to high temperature range of 1000 K to 6000 K and the second part for lower temperature range from 200 K to 1000 K. The JANAF coefficients for fuels used in this thesis are presented in Table 2.2.

Air 200 6000 1000 3.10131 0.00124137 -4.18816e-07 6.64158e-11 -3.91274e-15 -985.266 5.35597 3.58378 -0.000727005 1.67057e-06 -1.09203e-10 -4.31765e-13 -1050.53 3.11239
Methane 200 6000 1000 1.63543 0.0100844 -3.36924e-06 5.34973e-10 -3.15528e-14 -10005.6 9.9937 5.14988 -0.013671 4.91801e-05 -4.84744e-08 1.66694e-11 -10246.6 -4.64132
Hydrogen 200 6000 1000 2.93287 0.000826608 -1.46402e-07 1.541e-11 -6.88805e-16 -813.066 -1.02433 2.34433 0.00798052 -1.94782e-05 2.01572e-08 -7.37612e-12 -917.935 0.68301

Table 2.2. JANAF thermodynamic coefficients (OpenFOAM, 2014)

The Absolute enthalpy ($H(T)$) of a substance represented in the equation 2.34, is defined as,

$$H(T)=\Delta H_{f,298}+[H_T-H_{298}] \tag{2.36}$$

Where, $\Delta H_{f,298}$ is heat of formation and $[H_T-H_{298}]$ is heat content of the substance.

2.8 Boundary conditions

In order to complete the definitions of a fluid flow, proper boundary conditions are to be specified which yield an accurate representation of a well posed problem. The finite volume method requires the boundary fluxes either be known or expressed interms of the known quantities on the boundary and internal cell values. Mathematically the boundary conditions are specified interms of two basic types

a) Dirichlet boundary condition: the value of the variable is prescribed at the boundary.

b) Von Neumann boundary condition: the gradient of the variable normal to the boundary is prescribed at the boundary.

A linear combination of above boundary condition is known as mixed boundary condition. From numerical point of view more general distinction of boundary condition can be made as (Geurts, 2003)

a) Physical boundary condition

b) Artificial boundary condition

Physical boundary conditions represent flow conditions at actual boundaries of the computation domain e.g. wall/solid, whereas the artificial boundary conditions are formulated to represent a truncation of the flow domain and model aspects of flow outside the domain e.g. inlet ,outlet, and symmetric boundaries. Physical and artificial boundary conditions are specified interms of the mathematical boundary conditions.

In LES, the boundary condition specification is much more tedious than that in RANS as it requires proper representation of instantaneous quantities varying spatially and temporally at resolved grid scale. In general care must be taken in specifying velocity and pressure values at a given domain boundary, If one of them is fixed at the boundary then the other quantity should be allowed to have floating value. Fixing both velocity and pressure at particular boundary will lead to an over specification of the boundary condition leading to generation of spurious pressure waves at the boundary as the flow tries to adjust to the internal flow conditions near the boundary. In the following section treatment of individual boundary conditions are presented in detail.

2.8.1 Inlet boundary

In most of the simulation studies the inflow conditions are known more precisely than the outflow and the flow inside the domain is largely influenced by the inflow behaviour. Several methods for producing velocity fluctuations at the inlet of the domain have appeared in the literature (Lee et al., 1992, Lund et al., 1998, Klein et al., 2003, Keating et al., 2004, Kempf et al., 2005, Mathey et al., 2006, Baba-Ahmadi and Tabor, 2009).

A brief review of some these methods is presented recently by (Tabor and Baba-Ahmadi, 2010) categorizing them into precursor simulation and synthetic methods. In precursor simulation method, a separate precursor calculations of a flow are done with cyclic boundary condition to store turbulence data at a plane normal to the streamwise direction with respect to time, later introduced into the domain at the inlet for the main computations. The 'synthetic methods' involve generation of some form of random fluctuations having spatial and temporal correlations and later combined with the mean flow are introduced at the inlet. Some of the synthetic inflow methods in practice are Fourier transform based techniques, digital filter method, principle orthogonal decomposition and vortex method (synthetic eddy method). Each method has convenience and constrains interms of applicability to a particular numerical solution. In the present work, a precursor simulation based named as 'time varying mapped' and a synthetic boundary condition based on digital filter are implemented in OpenFOAM. The time varying mapped boundary condition is adopted to do interpolation of inlet library data both in time and space coordinates so that it can be used for both fine and coarse meshes with respect to the precursor mesh.

In digital filter method, a series of random data with zero mean and unity variance are digitally filtered (convolution) to reproduce first and second order one-point statistics as well as given spatial and temporal correlations of velocity fluctuations. Further Cholesky transformation is carried out to match the desired Reynolds stresses. These velocity fluctuations are superimposed on the given mean turbulent velocity profile to get the actual velocities at the inlet boundary. Initially this method developed by (Klein et al., 2003) for uniform mesh distribution to generate three dimensional flow field using Gaussian shape correlation function and one slice of this field in sequence was applied at the inflow boundary, which was demanding interms of computing power. Later on (Veloudis et al., 2007) proposed for non-uniform mesh and (Xie and Castro, 2008) improved it further for generating only two dimensional flow data and using exponential function instead of Gaussian function for correlation, this considerably reduced the computation cost. The method proposed by (Xie and Castro, 2008) is adopted in the present study and the step by step procedure of generating inflow field using the digital filter method is presented in detail in the Appendix B.

2.8.2 Outlet boundary

The overall mass balance in the domain is maintained by proper specification of the outlet boundary condition. Improper treatment of pressure and velocity at outlet boundary can lead to spurious numerical wave reflections that can seriously pollute the solution. Especially in case of subsonic outflows flows these spurious oscillations can travel back and forth in the computational domain and may cause the calculation to diverge and then crash (Rudy and

Strikwerda, 1981). Whereas when the flow at outlet is supersonic, the wave reflections cannot travel upstream, and will only propagate downstream. As a consequence, subsonic outflow conditions are generally more difficult to handle than supersonic outflow conditions.

Non-reflective pressure boundary condition implemented in OpenFOAM named as 'waveTransmissive' is simplification of Navier-Stokes characteristic boundary condition (NSCBC) proposed by (Poinsot and Lelef, 1992). Input parameters are L_∞ and p_∞, which represent the relaxation length scale from outlet boundary and pressure at L_∞ respectively. The L_∞ governs how reactive the outlet should be; a low value will give a more reactive outlet than a high value. The model begins by calculating the velocity (w) of the outgoing pressure wave,

$$w=\mathrm{U}.\hat{n}+\sqrt{\frac{\gamma}{\varphi}} \tag{2.37}$$

where $\hat{n}$ is unit normal outward to boundary, γ is ratio of specific heats and $\varphi=\frac{\rho}{p}$ is compressibility.

The pressure wave velocity is used to calculate the pressure wave coefficient α and the relaxation coefficient k,

$$\alpha=w\frac{\Delta t}{\delta} \tag{2.38}$$

$$k=w\frac{\Delta t}{l_\infty} \tag{2.39}$$

Where δ is the cell face distance coefficient and Δt is current timestep. Pressure is computed in the following way:

$$p_{temp} = \frac{p_0 + k\, p_\infty}{1+k} \tag{2.40}$$

$$\beta = \frac{1+k}{1+\alpha+k} \tag{2.41}$$

Where p_0 is pressure at the outlet boundary in the previous timestep. Finally the pressure at the outlet is applied as

$$p = \beta\, p_{temp} + (1-\beta)\, p_{cell} \tag{2.42}$$

where p_{cell} is the pressure in the cell attached to the outlet boundary.

The advective outlet boundary condition is applied for rest of the flow variables, which is similar in numerical implementation as that of the 'waveTransmissive' except that only flow velocity is used for convecting the flow properties out of domain and values at the boundary are not relaxed with any far field value as it has been done in the above mentioned pressure outlet boundary condition.

$$\frac{\partial \phi}{\partial t} + c\frac{\partial \phi}{\partial n} = 0 \tag{2.43}$$

where ϕ is any scalar variable or velocity component, c is the convection velocity, and n is the coordinate in the direction of the outward normal at the boundary.

In general, when the outlet boundary is place far away from the region of interest then a simple boundary treat of 'fixed value' can be specified for pressure field and 'zero gradient' can be specified for rest of the flow variables.

2.8.3 Symmetric boundary

The symmetry plane boundary is advantageous in reducing computational effort when some section of simulation domain is geometrically symmetric about a plane section. Although in reality the instantaneous flow quantities are never symmetric about a section but the discrepancies in the results can be greatly reduced by choosing the symmetric plane away from the region of interest. Numerically the component of the gradient normal to the boundary is fixed to zero and the components parallel to it are projected to the boundary face pointing outwardly for the respective flow quantities.

2.8.4 Periodic/Cyclic boundary

Periodic boundaries are to emulate infinite domain in homogenous direction or to take advantage of cyclic symmetry in the flow domain. The care should be taken in choosing the domain size that is larger enough than the individual flow variables correlated distances. Otherwise artificial flow periodicity will be introduced into flow quantities leading to unrealistic solutions. Numerical implementation of this boundary is that the fixed values of the flow variables from one boundary face are mapped/applied to the corresponding coupled boundary faces in the participating cyclic boundaries.

2.8.5 Wall boundary

The velocity of the fluid on the wall is equal to that of the wall itself, hence 'fixed value' boundary conditions is applied for velocity field. Flow near the wall is highly anisotropic due to the presence of wall boundary obstructing the flow. To get the instantaneous velocities on the wall one can resort to

resolving the flow field in the near wall region using refined mesh towards the wall. Turbulent eddies are inherently three dimensional in nature implies the need for similar refinement in the all three directions, which will greatly increase the computational cost making it only feasible for small scale simulation. Further details about the modeling of near wall region are discussed in Chapter 4. Impermeable wall has no mass flux passing through it, therefore pressure and species gradient are set to 'zero gradient'. The boundary condition for temperature field on the wall can be either of the following conditions.

i) Isothermal wall – 'fixed Value'

ii) Adiabatic wall – ' zero Gradient '

iii) Convective heat flux, under this condition the boundary can be specified as

(a) Fixed value of heat flux – 'fixed Gradient'

(b) Energy balance between heat conduction and boundary heat convection given by,

$$-k\left(\frac{dT}{dx}\right)=h(T_{\infty}-T_{w}) \tag{2.44}$$

where, 'k' is the thermal conductivity of the wall material and 'h' is heat transfer coefficient of fluid near wall.

2.9 Pressure-Velocity coupling

The governing equations described in section 2.4 along with the boundary conditions presented in section 2.7 are solved in the segregated manner, where in the equations are solved sequentially by iterative routines. The velocity and pressure coupling is solved by using PISO algorithm which is developed for the computation of unsteady compressible flows, detailed

descriptions of its algorithm can be found in (Issa, 1986) and (Peric and Ferziger). OpenFOAM follows co-located, cell centred variable approach and interpolation scheme is used to compute the variables on the cell face centres. A well known problem associated with the calculation of pressure on co-located meshes is one of `checker boarding' in which velocity and pressure become decoupled (Patankar, 1980). This may result in a physically unrealistic pressure field prediction being made from a correct solution to the momentum and continuity equations. This problem is solved by interpolating the discretised form of the momentum equation onto the cell faces and applying the continuity constraint to the cell face velocities following Rhie and Chow method (Rhie and Chow, 1983).

2.10 Validation study

Three dimensional channel flows is one of the most popular test problems for LES investigation of wall bounded turbulent flows. It was pioneered as a LES test problem by (Moin and Kim, 1982, Kim et al., 1987). The compressible turbulent boundary layer closely follow incompressible pattern as long as the rms fluctuating Mach number is small, which is the case in boundary layers with free stream Mach number less than 5 (Morkovin hypothesis) (Huang et al., 1995). As such the present compressible channel flow simulation results at friction Reynolds number $Re_\tau \sim 180$ are compared with the DNS results of (Kim et al., 1987). For sake of completeness the Morkovin hypothesis is further discussed in section 4.1.2.

Purpose of this validation study is to ascertain the numerical method and schemes in OpenFOAM to carry out rest of the validation/numerical

simulation in this thesis. Apart from this to serve as an inert turbulent channel flow base case for carrying out flame-wall interaction posteriori test of hydrogen-Air 'V'-flame anchored in a channel (in section 5.4).

One equation eddy viscosity model is used for computing sub-grid turbulence kinetic energy. The discretisation scheme for the time derivatives is second order accurate, implicit backward scheme. The convective terms are discretized using second order accurate Gaussian-Gamma bounded scheme. The diffusion terms are discretized using Gaussian linear corrected scheme which is central differencing, with explicit non-orthogonal correction. Finally the gradient terms are solved using Gaussian linear scheme which is also central differencing. Hence the combinations of above mentioned discretisation scheme make the numerical solver second order accurate in both time and space.

2.10.1 Numerical setup

The channel dimensions are 0.021 m X 0.006 m X 0.009 m (7H x 2H x 3H) and orientation is shown in figure 2.3.; Half channel height (H) = 0.003 m.

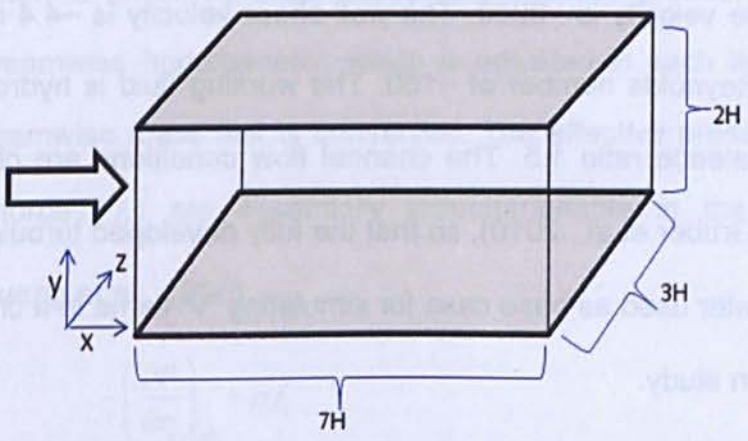

Figure 2.3. Channel layout (x- streamwise, y- wall normal, z-spanwise)

The channel domain is discretised into 260 x 200 x 160 ~ 8 million computational cells and flow near the wall is resolved using very non-uniform mesh distribution in the wall normal direction. The computational grid is stretched in the y-direction by a hyperbolic tangent function

$$y = h - \frac{h\tanh(\gamma(1-2j/N_y))}{\tanh(\gamma)} \tag{2.45}$$

where j is the wall normal grid index, N_y is the total number of points in the wall normal direction. The parameter γ = 2.85 controls the grid non-uniformity. The near wall region is fully resolved with first mesh point is within y^+ = 0.5 and 15 points within y^+ < 10 to satisfy the resolution requirement in viscous sub layer (Moser et al., 1999), where y^+ is nondimensional distance from wall given as $y^+ = {yu_\tau}/{\nu}$, u_τ is shear velocity given as $u_\tau = \sqrt{{\tau_w}/{\rho}}$ with τ_w is shear stress at wall, $\tau_w = \rho\nu \left.\frac{\partial\langle u\rangle}{\partial y}\right|_{y=0}$. Periodic boundary conditions are applied in both spanwise and streamwise direction. No slip and isothermal boundary condition at 750 K are imposed on top and bottom channel walls. The channel mean centreline velocity is ~80 m/s and the Reynolds number based on centreline velocity is ~3200. The wall shear velocity is ~4.4 m/s leading to a friction Reynolds number of ~180. The working fluid is hydrogen-Air mixture at equivalence ratio 1.5. The channel flow conditions are chosen similar to that of (Gruber et al., 2010), so that the fully developed turbulent channel flow can be later used as base case for simulating 'V'-flame in a channel for model validation study.

The initial velocity field is setup based on vortex-less low speed streaks profile with imposed sinuous perturbation based on the work of (Schoppa and Hussain, 2000) and integrated forward in time until flow reaches statistically steady state. Base flow profile is given as,

$$U^+(y^+,z^+)=U_0^+(y^+)+(\Delta u_0^+/2)\cos(\beta^+ z^+)(y^+/30)exp(-\sigma y^{+2}+0.5),\ V^+=0,\ W^+=0 \tag{2.46}$$

where, U_0^+ is the turbulent mean velocity profile Δu_0^+=11.2 is the streaks normal circulation per unit length, β^+ = 0.06 is spanwise wave number, σ = 0.00055 is transverse decay, The sinuous perturbation, streak waviness in the z direction (spanwise),

$$W^+(x^+,y^+)=\varepsilon\sin(\alpha^+ x^+)y^+\exp(-\sigma y^{+2}),\ U^+=0,\ V^+=0 \tag{2.47}$$

where, ε is the linear perturbation amplification, α^+=0.02 is wavenumber for streamwise direction flow. To avoid contamination of the solution by non physical acoustic oscillations due to rough initial flow perturbations, a low Mach number Solver (equations presented in section 2.4.2) is first applied and once the flow turbulence was established the solver was switched back to All Mach solver.

The flow is driven by mean favourable effective pressure gradient to maintain streamwise homogeneity, which is adjusted in each timestep such that the streamwise mass flux is conserved. The effective pressure gradient and body force (f_i) are essentially interchangeable in the momentum equation (Huang et al., 1995),

$$-\left(\frac{\partial P}{\partial x_i}\right)_{eff}=\rho f_i \tag{2.48}$$

The streamwise mass is conserved and the effective pressure or body force are computed for each time step as,

$$\int \rho u dy dz = \text{Constant} \tag{2.49}$$

$$-\left(\frac{\partial P}{\partial x_i}\right)_{eff} = \rho f_i = \frac{\int \rho u dy dz_{t_{new}} - \int \rho u dy dz_{t_{old}}}{\Delta t \int \rho dy dz} \tag{2.50}$$

The effective pressure gradient term used in the momentum equation is accommodated in energy equation as $-u\left(\frac{\partial P}{\partial x_i}\right)_{eff}$. Once the velocity field reaches statistically steady state, the simulations are further integrated in time to obtain time average statistic of flow variables.

2.10.2 Numerical results

The statistical steady state is identified by a linear total shear stress profile (Bradshaw, 1985), which is computed as,

$$Total\ shear\ stress = viscous\ stress + Reynolds\ stress$$

$$Total\ shear\ stress = \rho \upsilon \frac{\partial \langle U \rangle}{\partial y} - \rho \langle u'v' \rangle \tag{2.51}$$

where, <.> is ensemble averaging. The stress profiles normalized by the shear velocity along the half channel height are shown in Figure 2.4. The excellent linear profile of the total stress indicates that the channel flow is in state of fully developed turbulent flow and the ensemble averages of flow statistics have attended steady state. The viscous stresses are dominant in near the wall region and there after the Reynolds stress are dominant towards the channel centreline. Overall the total shear stress is maximum near the wall and diminishes to zero towards the channel centreline.

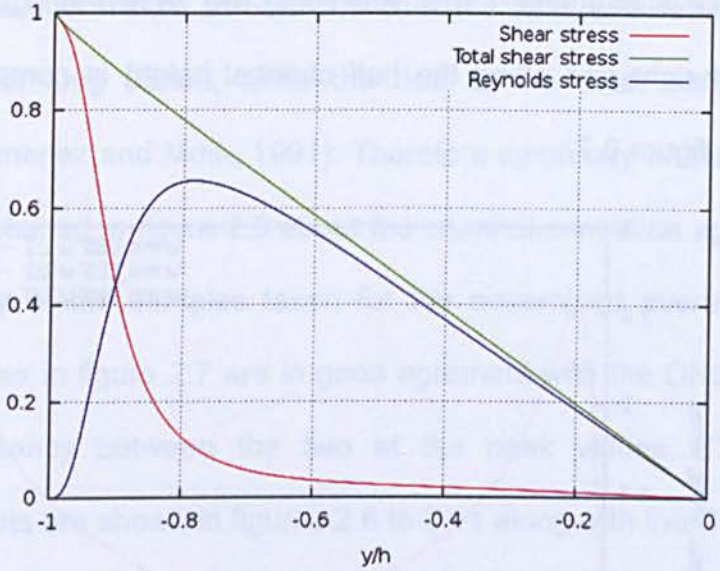

Figure 2.4. Reynolds stress and total stress plot normal to wall (up to half channel height)

The profile of the mean streamwise velocity non- dimensionalised by the wall shear velocity is shown in figure 2.5 on linear axis scale and the inset figure in log scale x-axis. Good match of the velocity profile with the DNS data is obtained and this corresponds to the adequacy of the sample taken for the ensemble averaging.

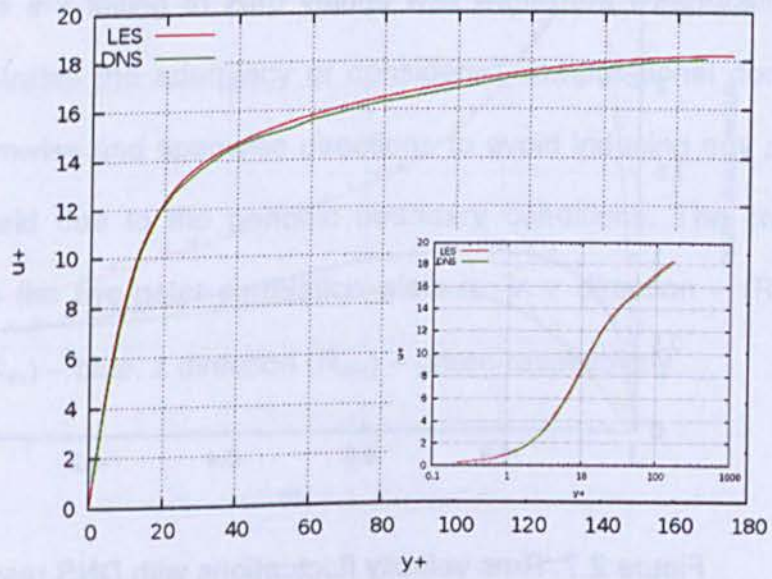

Figure 2.5. Streamwise mean velocity profile

Turbulence fluctuations (rms velocities) are shown in figure 2.6 along the channel height and along the half channel height in comparison with DNS results in figure 2.7.

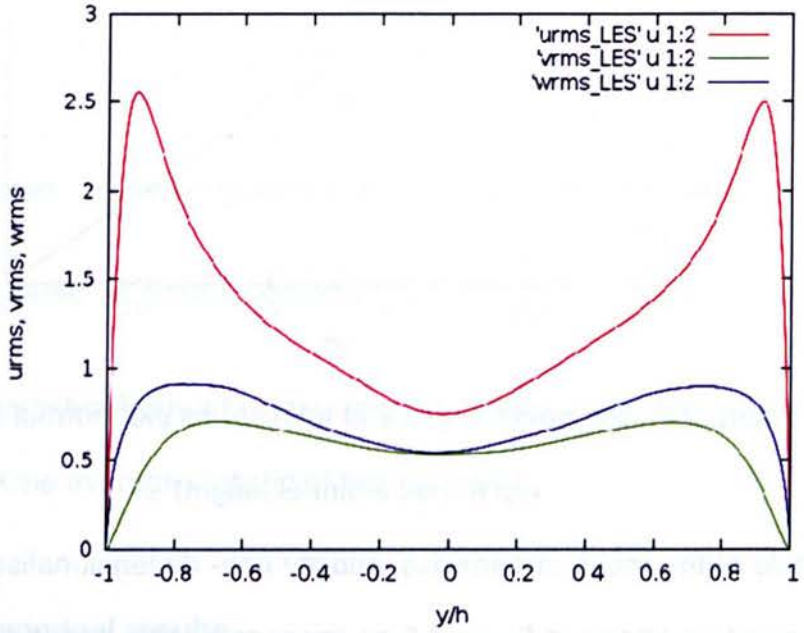

Figure 2.6. LES rms velocity fluctuations along the channel height

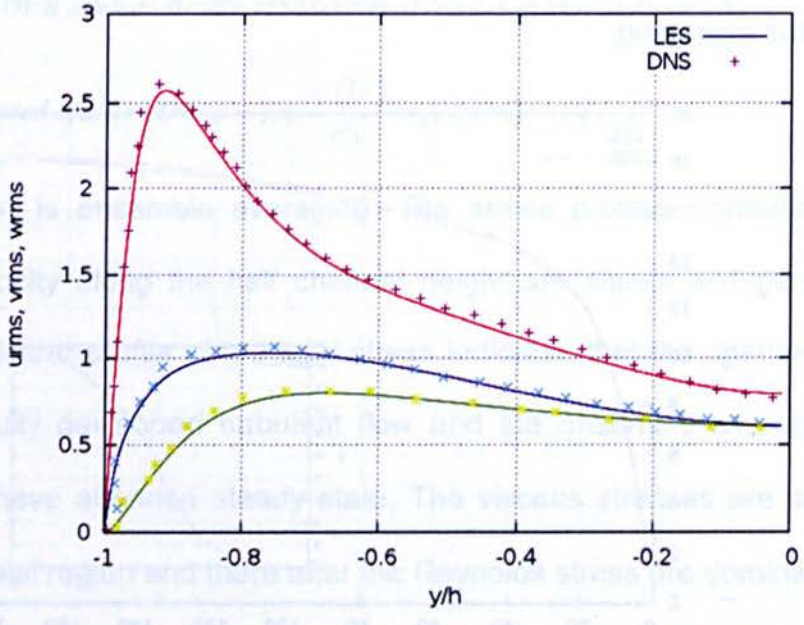

Figure 2.7. Rms velocity fluctuations with DNS results

Turbulence is intermittent at both the channel walls and resides only at a single wall for long period, while the flow at the other wall is relatively quiescent (Jimenez and Moin, 1991). Therefore symmetry of the rms velocity profiles as obtained in figure 2.6 about the channel centreline again indicates the adequacy of the samples taken for the ensembled average. The rms velocity profiles in figure 2.7 are in good agrement with the DNS results with slight discrepancy between the two at the peak values. The two-point correlation plots are shown in figures 2.8 to 2.11 along with the DNS results. It characterizes the distance over which the fluctuating velocity field is correlated. The two-point correlations are plotted at two y locations in streamwise and spanwise direction - one very close to the wall ($y^+ = 5$) and the other close to the centerline ($y^+ = 149$). As expected the velocities have correlations over longer distance in streamwise direction (figure 2.8 & figure 2.10) than in the spanwise direction (figure 2.9 & figure 2.11), since the net channel flow is driven in the streamwise direction. It is clear from the plots that curves are falling to zero values well within the computational domain limits, Illustrates the adequacy of considered computational domain size in both streamwise and spanwise directions to avoid inducing any periodicity in the flow field due to the periodic boundary conditions. The colour legend followed in the two-point correlation plots is: in x direction – (R_{uu}) – red, y direction (R_{vv}) – blue, z direction (R_{ww}) – green respectively.

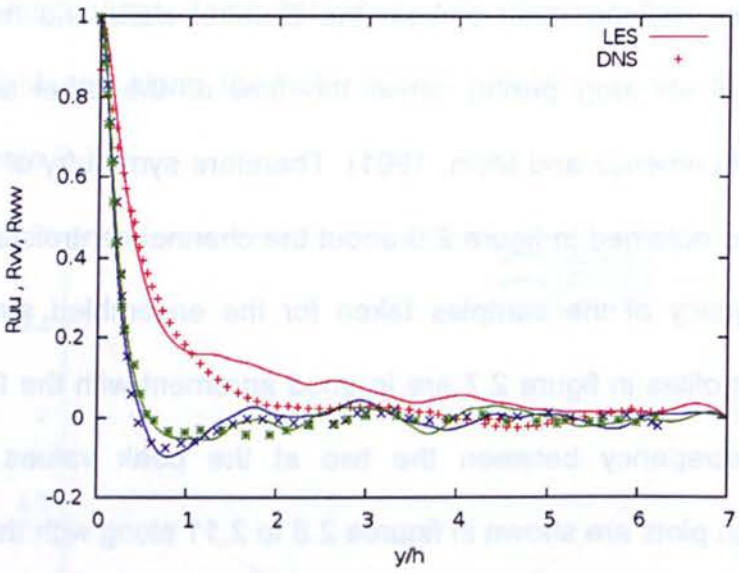

Figure 2.8. Two point correlation in streamwise direction at $y^+ \sim 5$ along streamwise direction

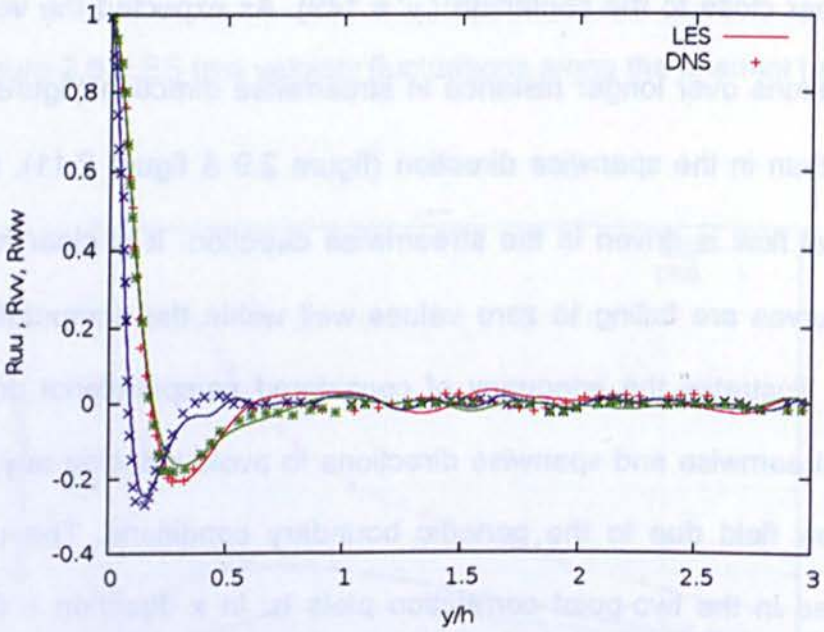

Figure 2.9. Two point correlation in spanwise direction at $y^+ \sim 5$ along spanwise direction

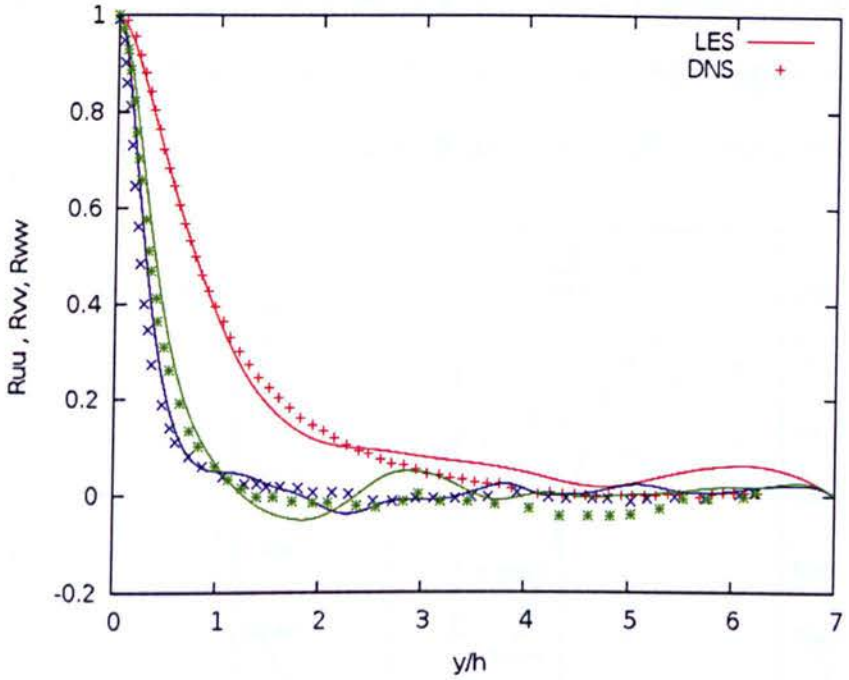

Figure 2.10. Two point correlation in streamwise direction at $y^+ \sim 149$ along streamwise direction

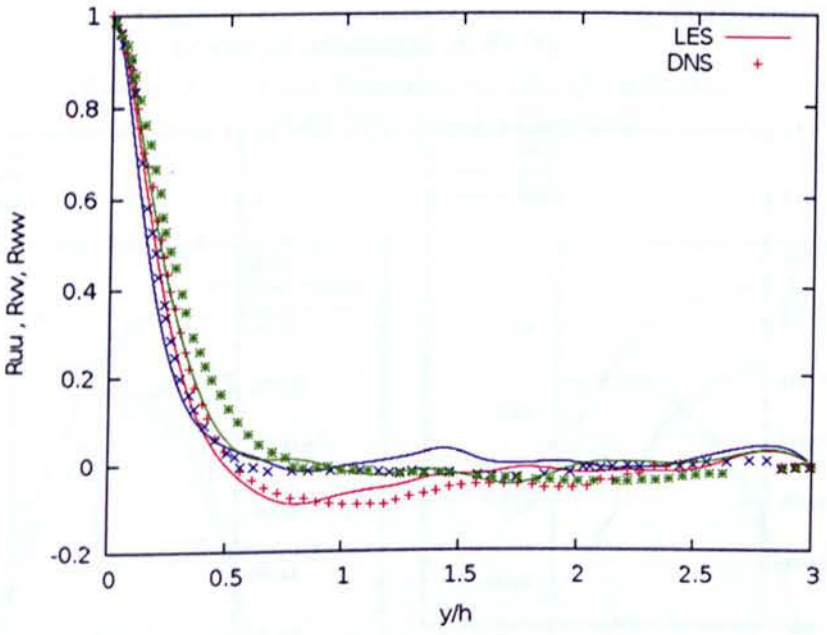

Figure 2.11. Two point correlation in spanwise direction at $y^+ \sim 149$ along spanwise direction

The energy spectra plots illustrate the flow kinetic energy distribution at various length scales (wave numbers). The one dimensional energy spectra plots are shown in figure 2.12 to figure 2.15.

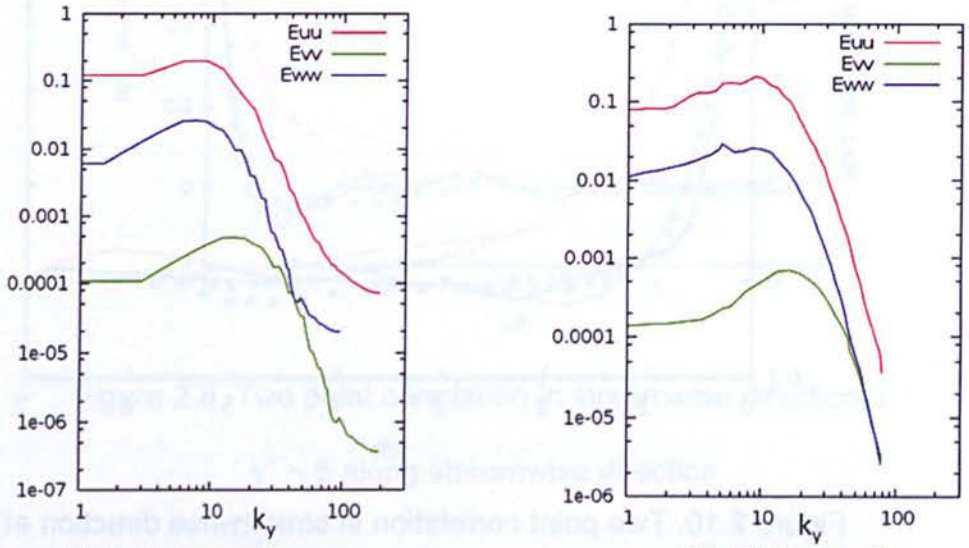

(a) LES results (b) DNS results

Figure 2.12. One dimensional energy spectrum at y+ ~5 in spanwise direction

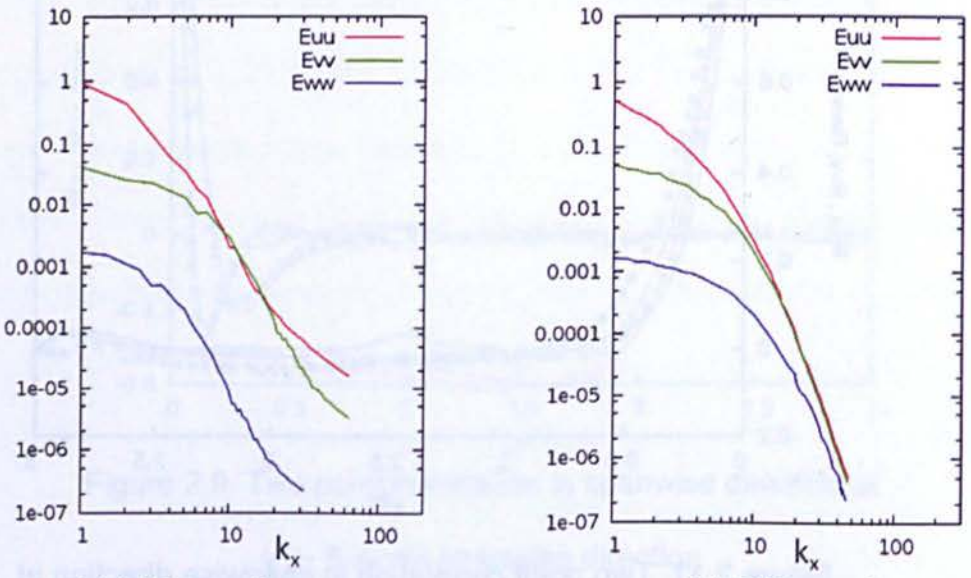

(a) LES results (b) DNS results

Figure 2.13. One dimensional energy spectrum at y+ ~5 in streamwise direction

The one dimensional energy spectra are plotted at two y locations in streamwise and spanwise direction - one very close to the wall (y^+ = 5) and the other close to the centerline (y^+ = 149).

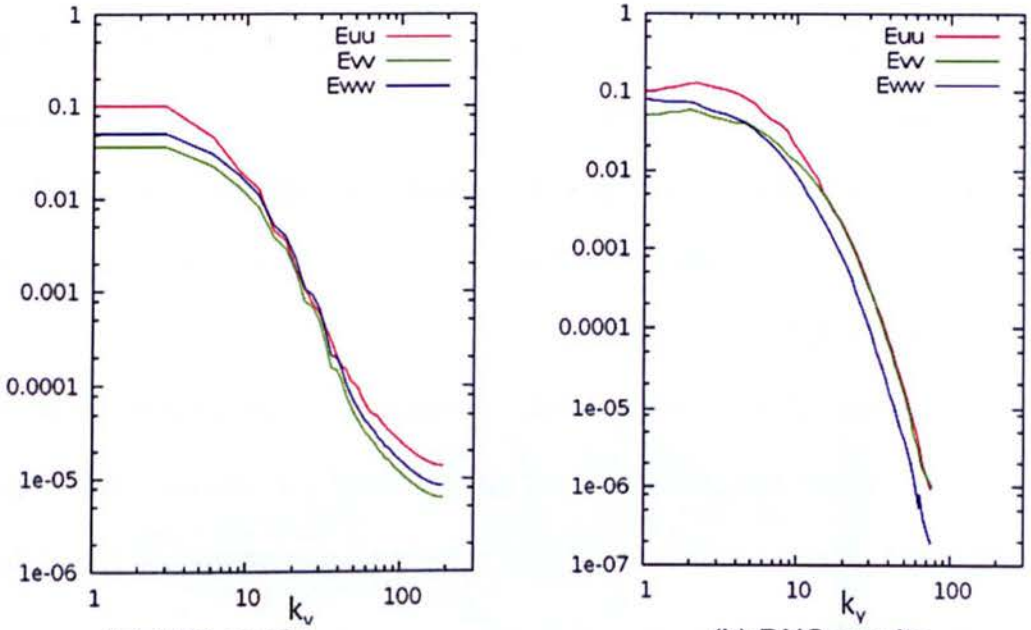

(a) LES results (b) DNS results

Figure 2.14. One dimensional energy spectrum at y+ ~149 in spanwise direction

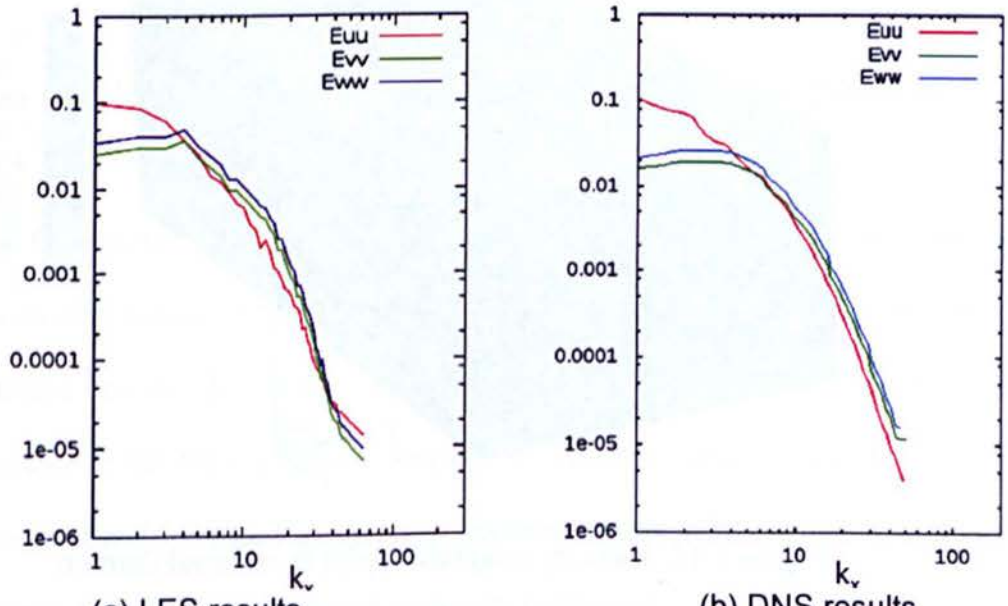

(a) LES results (b) DNS results

Figure 2.15. One dimensional energy spectrum at y+ ~149 in streamwise direction

The energy density associated with the high wavenumber is few order (decades) lower than to the energy density at lower wave numbers, elucidate that the grid resolution is adequate in capturing the energy transfer from larger to smaller scales (Kim et al., 1987). The DNS spectra plots and the LES spectra plots cannot be compared one to one as the grid resolution in both the simulation is different and hence the resolved length scales will be also be different. Moreover the LES results trends are satisfactory in comparison to the DNS results.

Figure 2.16 shows the velocity magnitude contour plot on the channel domain, it can be discerned that the centre of the channel has large scale flow eddies and near the wall small scale eddies ejecting low speed fluid into core of the flow.

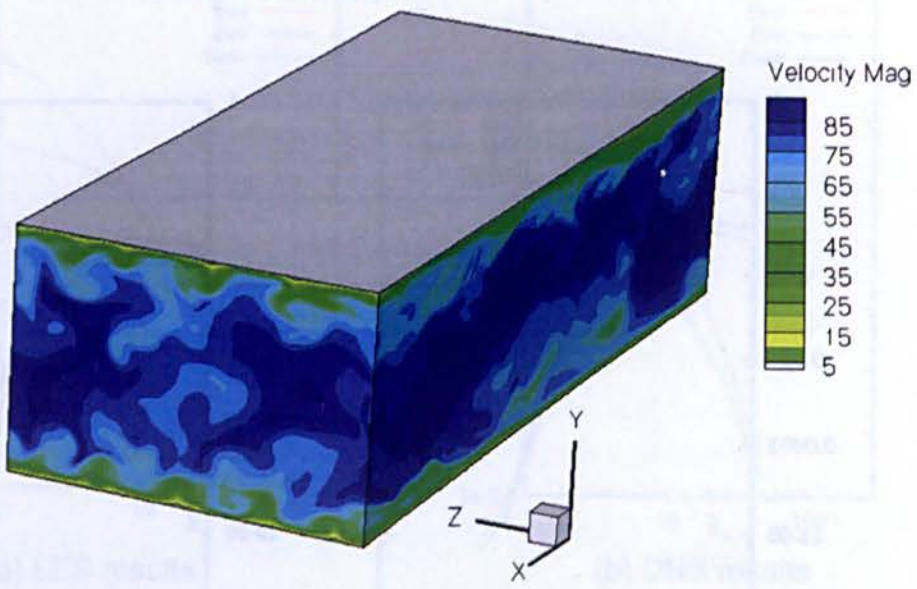

Figure 2.16. Velocity magnitude plot in channel domain

The most prominent structural features of near-wall turbulence are streaks of low momentum fluid which are been lifted into the buffer region as elongated longitudinal vortices. The velocity gradient tensor represents the balance between rotation and strain rate, flow visualization based on velocity gradient topologies provide some interesting evidence of direct linkage between the inner and outer turbulence flow. Vortex eduction techniques Q method and λ_2 method extensively used in turbulence research for identify the near wall flow structures are based on velocity gradient tensor analysis.

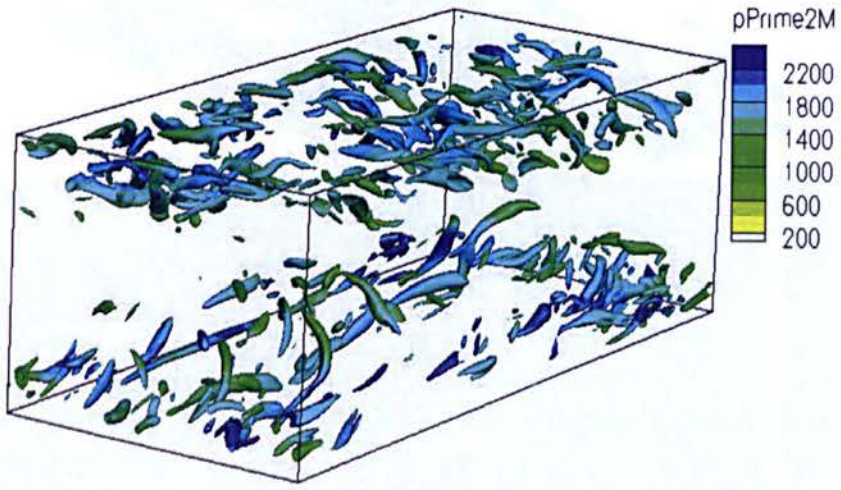

Figure 2.17. Flow structures near both channel walls (Q method)

The Q criterion devised by (Hunt et al., 1988), defining as an eddy zone region characterized by positive values of the second invariant of the velocity-gradient tensor. Moreover, Q can be interpreted as the source term of pressure in the Navier-Stokes equations . The flow structures close to the wall using second invariant of velocity gradient tensor - Q method are shown in figure 2.17 with superimposed pressure fluctuations.

The λ_2 method proposed by (Jeong and Hussain, 1995), based on the second largest eigenvalue of the tensor formed by summing the products of the symmetric and antisymmetric parts of the velocity-gradient tensor by considering the problem of the pressure minimum for definition for a vortex.

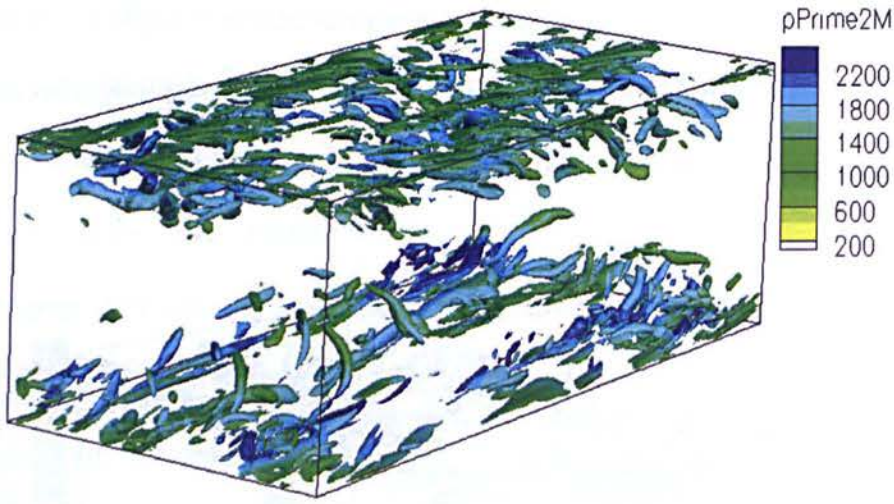

Figure 2.18. Flow structures near bottom channel wall (λ_2 method)

Figure 2.18 is showing the near wall flow structures plotted using λ2 method with superimposed pressure fluctuations. The vortex magnitude is contour plotted in a horizontal plane close to the bottom wall in figure 2.19. The high and low speed streaky structures in the streamwise direction are well captured in plot. The slow moving fluid in the colour blue is adjacent to red coloured faster moving fluid.

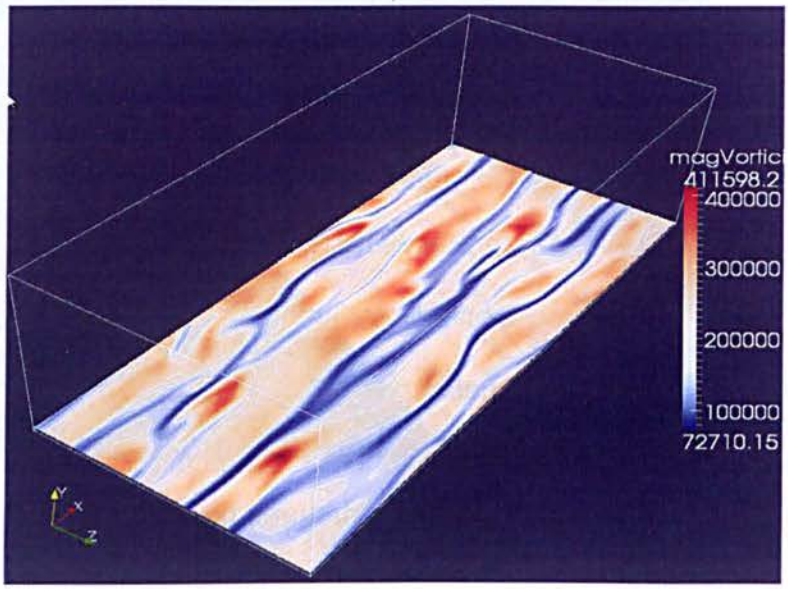

Figure 2.19. Flow streaks on the bottom wall

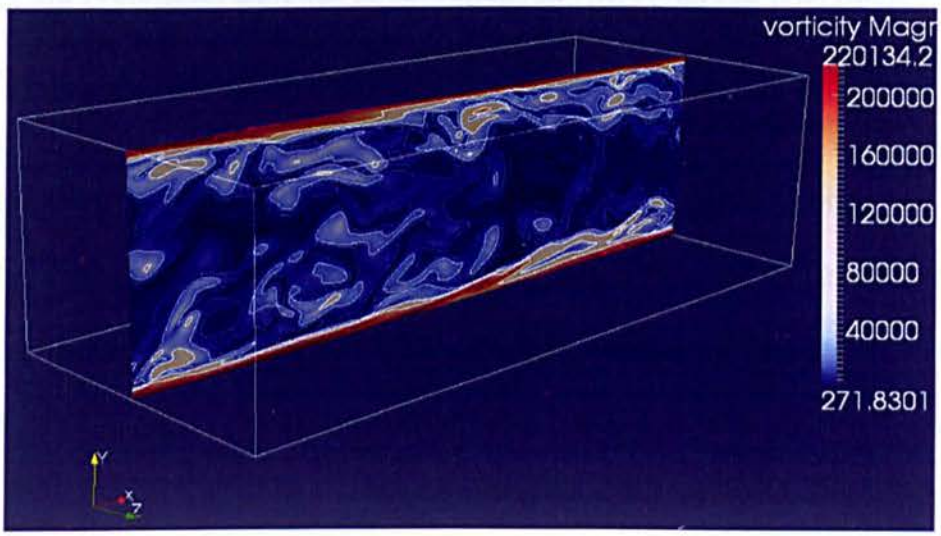

Figure 2.20. Vortex structures in vertical plane in streamwise direction

The vortices magnitude contour plot in vertical plane is shown in figure 2.20. It can be discerned that the magnitude of vortices is high near the wall and the coherent flow structures are lifting from the wall and elongating into the core of the flow.

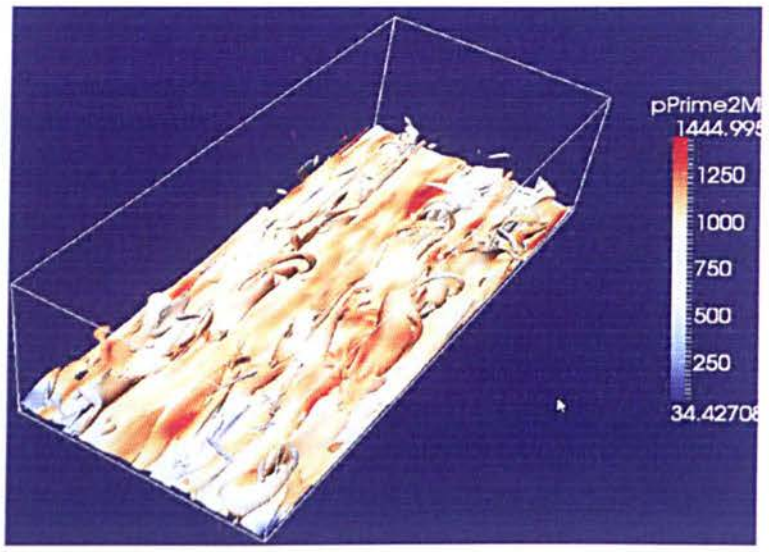

Figure 2.21. Vortex structures near bottom wall

The vortices magnitude iso-surface plot superimposed with pressure fluctuations is shown in figure 2.21. Clearly the fine flow structures near the wall are well captured by the vortex eduction methods derived from the velocity gradient tensors (figure 2.17 and 2.18).

The LES turbulent channel flow single-point and two-point statistics so far discussed are well predicted by the LES solver, essentially capturing the wall generated turbulence features. LES results also compare satisfactorily with the DNS results, hence validates the employed numerical solver and the schemes in simulating the turbulent flows.

2.11 Summary

Turbulent flows occur at high Reynolds number. Turbulence is characterized by fluctuations of all local properties, any property 'f' can be split into mean $\bar{f}$ and fluctuating f' contributions. The computational approach for solving Navier-stokes equations can be performed at three different levels namely,

RANS, LES and DNS. LES approach resolves large scale motions and models small scales which are more universal in nature, therefore is able to predict the occurrence of instabilities due to heat release, hydrodynamic flow fields and acoustic waves. The governing NSE equations are present in All Mach and low Mach number approximation. The boundary condition are discussed in LES context to completely define a given flow problem.

The turbulent flow governing equations, numerics and the boundary conditions together defining the CFD solver are validated by simulating a well known LES test case - channel flow case based on DNS work of (Kim et al., 1987). The LES turbulent channel flow at results $Re_t \sim 180$ are presented this chapter along with the DNS results. The LES compressible channel flow results are compared with the incompressible DNS channel flow results under Morkovin hypothesis. The density weighted LES results are in well match to the DNS results. The velocity gradient tensor methods Q and λ_2 are plotted to identify the typical features of wall generated turbulence.

Chapter 3

PREMIXED COMBUSTION MODELING

3.1 Introduction

Premixed turbulent combustion is a highly complex process but one which greatly affects everyday life. The quest to better understand this physical process is continual and one aspect of it is the search for computational models to describe the processes involved. The model may be of less detailed than the actual physical phenomenon in the nature, but should provide adequate treatment for the turbulence, the chemical reactions of the combustion and consequential heat release, as well as the mutual interaction of these areas, since the combustion alters the physical properties of the fluid and drives the flow, whilst the flow moves reactants and products around and thus influence the combustion (Tabor and Weller, 2004). Combustion modeling is essential for providing a better estimate of the physical mechanism which are key to improving the performance and reducing the environment impact of combustion systems

This chapter gives an overview of the combustion modeling, starting with description of premixed laminar flame structure in section 3.2. The premixed laminar flames properties - thickness and flame speed are defined in section 3.3 and 3.4 respectively. The combustion regimes in the premixed turbulent combustion are discussed in section 3.5. Brief overviews of different modeling approaches in premixed turbulent combustion are provided in

section 3.6. The Coherent flame Model (CFM) and modeling of individual terms in the flame surface density transport equation are describes in section 3.7. The Lewis number effects are discussed in section 3.8. Followed by limitations in the CFM-LES modeling in section 3.9. Finally this chapter is concluded in section 3.10 with brief summary of above discussions.

3.2 Premixed laminar flame structure

The laminar premixed flame fronts can be distinctly identified into three different layers (Williams, 1985, Peters, 2000) as shown in Figure 3.1, namely a) preheat zone – which is mostly chemically inert (excepting hydrogen flames), b) inner layer – the zone of chemical reaction wherein the fuel is consumed with significant heat release, and c) oxidation layer – in this zone the oxidation of radicals formed in the inner layer is completed.

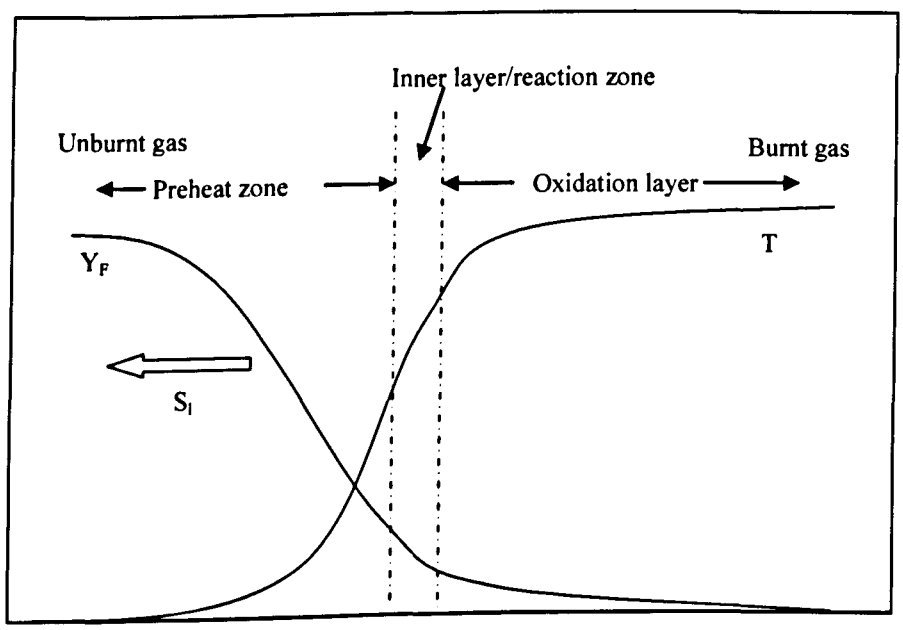

Figure 3.1 Premixed laminar flame front structure

The temperature of the gaseous mixture increases across the flame front while the mixture density decreases such that the pressure of the mixture remains nearly constant across the flame. This flame thickness separates the unburnt fresh gases (a mixture of fuel and oxidizer) from the burnt hot gases (a mixture of the hot products of the chemical reactions). The flame front has finite thickness and propagation flame speed. The speed of the one-dimensional planar unstretched freely propagating flame is termed as unstretched laminar flame speed (S_l) and is one of the primary important parameters in modeling premixed flames and other being the laminar flame thickness.

3.3 Laminar flame thickness

Premixed flame thickness is one of the important input parameters in numerical premixed combustion models. Flame thickness is also critical in determining the grid resolution in numerical simulations. Various definitions for the flame thickness are being used by researchers, notably the diffusive thickness, total flame thickness, thermal thickness and reaction thickness.

Diffusive thickness is defines as the ratio of the thermal diffusion coefficient to the laminar flame speed

$$\delta_d = \frac{D_{th}}{S_L} = \frac{\lambda}{\rho C_P S_L} \tag{3.1}$$

The quantities ρ, C_P and λ are evaluated in unburnt gases.

Thermal thickness is based on temperature profile of flame and defined as the ratio of the temperature difference to that of maximum temperature gradient across the flame

$$\delta_{th} = \frac{T_b - T_u}{\max \left| dT/dx \right|} \tag{3.2}$$

Total flame thickness is also based on the temperature profile and defined as the distance over which the reduced temperature T_{rd} changes from 0.01 to 0.99, where reduced temperature is given as $T_{rd} = \frac{T - T_u}{T_b - T_u}$.

In general the diffusion thickness gives smaller and the total thickness (δ_{tot}) gives larger predictions for the flame thickness as shown in Fig. 3.2. The thermal thickness is considered a reasonable representation of the premixed laminar flame thickness (Poinsot and Veynante, 2005).

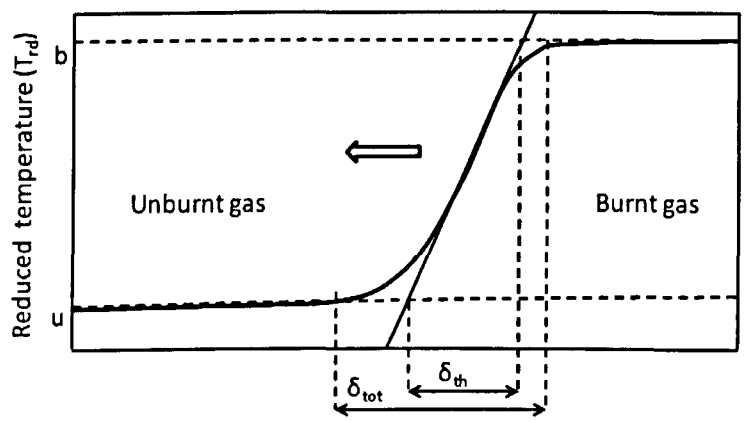

Figure 3.2. Flame thicknesses for premixed flames (Poinsot and Veynante, 2005)

Since the estimation of the flame thickness is required *a priori* in the combustion models for computation of premixed flames, the correlation proposed by (Blint, 1986) , gives fairly good estimation of the thermal flame thickness,

$$\delta_L^b = 2\frac{D_{th}}{S_L}\left(\frac{T_b}{T_u}\right)^{0.7} \tag{3.3}$$

Table 3.1 presenting the values of thermal flame thickness or simply the unstretched laminar flame thickness (δ_l) used in the present research work.

s. no	fuel	Equivalence ratio	Thermal flame thickness (mm)
1	Hydrogen	1.0	0.3
2	Methane	1.0	0.70
3	Propane	1.0	0.43

Table 3.1. Typical values for the flame thickness used in the present simulation work

3.4 Laminar flame speed

Unstretched Laminar flame speed (S_l), is the speed at which a free planar laminar flame will propagate. S_l is an input quantity in flamelet combustion models introducing the fuel chemistry. It depends on the reacting mixture composition, temperature and pressure. Experimental results are fitted into power law expression (Metghalchi and Keck, 1980, Gülder, 1984), to provide laminar flame speed as a function of equivalence ratio, fresh gas temperature and pressure.

$$S_l(\phi,T,P) = S_{l,0}(\phi)\left(\frac{T}{T_{ref}}\right)^{\alpha}\left(\frac{P}{P_{ref}}\right)^{\beta} \tag{3.4}$$

where, $S_{l,0}(\phi)$ is a polynomial fit for the unstretched laminar flame speed as a function of equivalence ratio within the flammable limits at reference

temperature (T_{ref}), pressure (P_{ref}), α and β are temperature and pressure exponents respectively. The reference temperature and pressure are 300 K and 1 bar respectively.

The following experimental correlation has been used in the present work for the respective fuel gases:

a) Methane (Gülder, 1984)

$$S_{l,0}(\phi)=W\,\phi^{\eta}\,e^{-\xi(\phi-\sigma)^2} \tag{3.5}$$

with W (cm/s) = 42.2, η = 0.15, ξ = 5.18 and σ = 1.075. The exponents of temperature and pressure ratio are 2.0 and -0.5 respectively.

b) Hydrogen (Dahoe, 2005)

$$S_{l,0}(\phi)=2.1087\phi^5-8.6278\phi^4+10.455\phi^3-2.8908\phi^2+1.3031\phi-0.1075 \quad for\ \phi<1.7$$

$$S_{l,0}(\phi)=0.0027\phi^5-0.067\phi^4+0.645\phi^3-2.8799\phi^2+5.1941\phi-0.1446 \quad for\ \phi\geq 1.7 \tag{3.6}$$

The exponents of temperature and pressure ratio are 1.4 and -0.1 respectively.

In general, the laminar flame speed is a strong function of temperature and a weak function of pressure, which means that the laminar flame speed increases rapidly when the temperature of the fresh gas increases but decreases slightly when pressure increases.

3.5 Combustion regimes

Turbulent combustion involves various lengths, velocity and time scales describing turbulent flow field and chemical reactions. Therefore the derivation of the combustion models depends on the physical analysis and comparison of these time and length scales. Diagrams defining combustion

regimes in terms of non-dimensional numbers based on length and velocity scale ratios have been proposed by (Bray, 1980, Borghi, 1985, Williams, 1985, Peters, 1988, Abdel-Gayed et al., 1989, Peters, 1999).

The characteristic length, time scales and the non-dimensional numbers are typically associated with the turbulence and combustion are briefly discussed below

- Chemical time scale (τ_c) : it is the ratio of the laminar flame thickness (δ_l) and the laminar flame propagation speed (S_l)

$$\tau_c = \frac{\delta_l}{S_l} \tag{3.7}$$

Turbulent time scale (τ_t) : it is estimated as the ratio of the integral length scale (l_t) and the (u') rms velocity (square root of turbulent kinetic energy).

$$\tau_t = \frac{l_t}{u'} \tag{3.8}$$

Damköhler number (Da) : defined for the largest eddies (l_t) as the ratio of turbulent time scale to chemical time scale.

$$Da = \frac{\tau_t}{\tau_c} = \frac{l_t S_l}{\delta_l u'} \tag{3.9}$$

Karlovitz number (Ka) : defined for smallest eddies (η_k) as the ratio of chemical time scale to the kolmogorov time scale (τ_k)

$$Ka = \frac{\tau_c}{\tau_k} = \frac{\sqrt{\varepsilon/\nu}}{S_l/\delta_l} \tag{3.10}$$

- Turbulent Reynolds number (Re_t) : compares turbulent transport to the viscous forces

$$\mathrm{Re}_t = \frac{u' l_t}{\nu} = \left(\frac{u'}{S_l}\right)\left(\frac{l_t}{\delta_l}\right) \quad \Rightarrow \mathrm{Re}_t = Da^2\, Ka^2 \tag{3.11}$$

Based on these non-dimensional numbers, the combustion regime may be identified in terms of length (l_t/δ_l) and the velocity (u'/s_l) ratios based on modified combustion diagram proposed by (Peters, 1999, Peters, 2000),

- Laminar flame regime: Re_t < 1. The line Re_t = 1 separates the laminar flame regime from the turbulent combustion regime Re_t >1.
- Corrugated and wrinkled flamelets regime : Ka < 1 and Da > 1, the chemical time scale is shorter than any turbulent time scale and the flame thickness is smaller than the smallest turbulent scales, the Kolmogorov scales. In this regime, the flame front is thin, has an inner structure close to a laminar flame and is only wrinkled by the turbulence motions. This thin flame regime or flamelet regime may be divided into two regions depending on the velocities ratio (u'/s_l).
  - ($u' < s_l$) - the speed of turbulent motion is too low to wrinkle the flame front up to flame interactions. This regime is identified as "wrinkled flamelet regime ".
  - ($u' > s_l$) - as the turbulent motions velocities become greater than the flame front speed, the turbulent motion wrinkles the flame front leading to the formation of pockets of fresh and burnt gases. This regime is identified as a thin flame with pockets or "corrugated flamelet regime".
- Thin reaction zone or thickened flame regime : 1< Ka < 100 and Da >1. In this zone, the turbulent integral time scale is still larger than the chemical time scale but the Kolmogorov scales are smaller than the flame thickness

and larger than the reaction zone. The turbulent motions are able to modify the preheat zone but not the reaction zone, which remains close to a wrinkled laminar reaction zone.

- Distributed burning or broken reaction zone : Ka > 100 and Da < 1 , turbulence motions have shorter characteristics times than the chemical reaction time τ_c , mixing is fast and the overall reaction rate is limited by chemistry. Both preheat and the reaction zones are affected by turbulent motions. The flame front is intensively disturbed by the small flow structure and the reaction take place in regions instead of layers.

These regimes are plotted on a combustion diagram as a function of length (l_t / δ) and velocity ($u' < s_l$) ratios shown in figure 3.3 using the log scale.

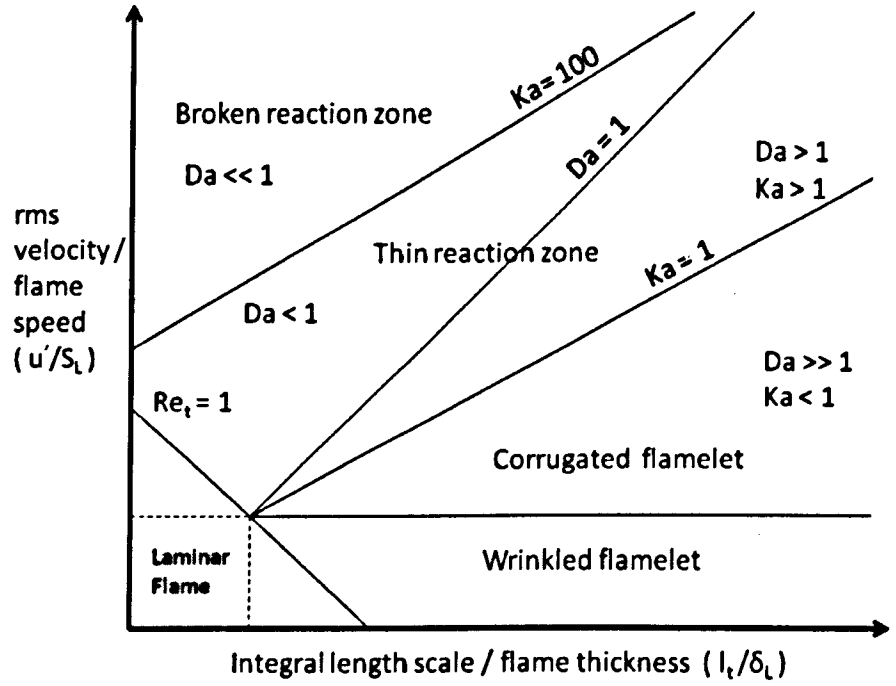

Figure 3.3. Modified combustion regimes diagram for turbulent premixed flames (Peters, 1999),(Peters, 2000).

The boundary line $u' = s_l$, separates the wrinkled flamelets regime from the corrugated flamelet regime. Similarly the Ka=1 line is boundary between corrugated flamelets and thin reaction zone, which is condition that flame thickness is equal to the Kolmogorov length scale is known as the Kilmov-Williams criterion.

3.5.1 Limiting case based on Damköhler number

For Da >> 1, chemical times are shorter than the integral turbulence time. Hence turbulence is not able to affect the inner flame structure which remains close to the laminar flame, wrinkled by the turbulence motions (Flamelet regime).

For Da << 1, the chemical time is larger than turbulence times. The overall reaction rate is therefore controlled by chemistry whereas the reactants and products are mixed by the turbulence motions. This regime is called the "perfectly stirred reactor".

DNS studies by (Poinsot et al., 1991) suggest that the flamelet regime can be extended to accommodate flames whose internal structure may be somewhat altered by small scale turbulence without leading to quenching of the flamelets. This indicates that the validity of flamelet assumption can be extended up to thin reaction regime.

The summary of the combustion regimes identified interms of Karlovitz number (Ka) and Damköhler number (Da) number is presented in Table 3.2.

Ka < 1 and Da > 1	Ka > 1 & Ka < 100 and Da > 1	Da << 1
Flamelets	Thickened flames	Well stirred reactor
Flame is thinner than all turbulence scales	Small turbulence scales may enter the flame front	All turbulence time scales are smaller than the chemical time scale

Table 3.2 Summary of the premixed turbulent combustion regimes

3.6 Modeling strategies

Turbulent combustion models may be devised in many different ways. The classical approach is based on statistical techniques and the determination of the mean reaction rate usually involves a presumed probability density function. Alternative description of turbulent combustion relies on the flamelet concept. The flamelet approach views a turbulent flame as an ensemble of discrete, steady laminar flames, called flamelets. The structure of these flamelets is identified and can be analysed separately. An important advantage of this concept is that it decouples complex chemistry and molecular transport problems from the modeling of the turbulent flow field.

The flamelet concept in premixed turbulent flames has been reviewed extensively by (Peters, 1988), (Libby and Williams, 1994) and by many others. In most of premixed turbulent combustion applications has longer turbulent time and spatial scales compared with the chemical time and spatial scales leads to chemical reaction generally being confined to a thin propagating surfaces with a thickness between 0.1 mm and 1 mm. The unburned reactants and burnt products are separated by this thin reacting

interface called flamelets that preserve their locally laminar structure. The local rate of reactant consumption can be approximated using the planar laminar flame. This effectively decouples the effects of chemistry and turbulence. Chemical effects work to modify the local laminar flame speed, which may be obtained from separate laminar flame calculations (Cant and Bray, 1989). The primary effect of the turbulence is to wrinkle and strain the embedded laminar flamelets.

Typically range of the turbulent premixed flame thickness is 0.1 to 1mm which is much smaller than the LES mesh size. Thus the flame front cannot be resolved in the computation. To overcome this difficulty, methods based on simulations of artificially thickened flame or flame tracking technique G-equation method or filtering with Gaussian filter larger than the mesh size are adopted. The latter approach requires development of sub grid scale models for filtered reaction rates and unresolved scalar transport that increases the flame thickness either through turbulent diffusion or through numerical diffusion (Poinsot and Veynante, 2005) .

(Butler and O'Rourke, 1977) proposed an attractive solution of propagating premixed flames on coarse grid in terms of artificially thickened flames. The thermal diffusivity and reaction rate are altered by a factor to maintain actual flame speed in the thickened flame front. The flame cusps are avoided due to addition of artificial diffusivity, thus altering the conjugation between displacement and consumption speed. Overall the thickened flame modifies the interaction between turbulence and flame, but this method seems to be promising at least when the flow scales are much larger than the laminar flame thickness as in combustion instabilities.

The G-equation technique is quite suitable for large eddy simulation of turbulent premixed flame in terms of resolving the flame front (Kerstein et al., 1988). In this approach the flame thickness is set to zero and the flame front is described as propagating surface using G-field. The resolved G-field does not need to follow the progress variable gradient and can be smoothed out to be resolved on the LES mesh. Subgrid turbulent flame speed closure is required in the model. The drawback of this approach is that the G-field is an arbitrary field and difficult to validate it with DNS and experiments. Moreover turbulent flame speed is not a well defined quantity and no universal model is available, experimental data exhibits a large scatter and depends on various parameters like chemistry characteristic, turbulence scales, pressure, flow geometry etc (Poinsot and Veynante, 2005).

Further attempts to model combustion LES were to extend the RANS closures to LES context. (Möller et al., 1996) investigated three different reaction rate formulations, the eddy dissipation kinetic model, a model based on the presumed PDF approach, and finally a monotonically integrated LES model that does not explicitly take subgrid scale effects into account. The predictive capabilities of these LES models were studied by numerical simulations of the flow past a triangular-shaped flame holder in a rectilinear channel at various operating conditions parameterized by the equivalence ratio, inlet velocity, and temperature. Comparison of simulated and measured experimental quantities indicates that these models are capable of predicting the flow accurately. The LES based Eddy Break Up model still has deficiencies, with the reaction rate being independent of chemical reaction and over estimation of the reaction rate in the zone of strong shears.

The filtering of the progress variable balance equation is another popular approach with different reaction rate closures. The filtered progress variable is resolved using physical space Gaussian filter with filter size larger than the computational mesh size. The closure for subgrid flame surface density (the flame surface area per unit volume at the subgrid scale level) or the subgrid scale flame wrinkling factor (the ratio between the subgrid flame surface and its projection in the propagation direction) is required for the model. (Knikker et al., 2002) conducted large eddy simulations of premixed combustion based on the reaction progress variable approach. The unresolved reaction rate is modelled using a flame surface density method, in which the filtered fuel consumption rate is written as a product of a local laminar flame speed times a factor that corresponds to the flame surface area per unit volume, the Flame Surface Density (FSD). This method requires a model for both resolved and unresolved FSD, and the authors selected an algebraic form developed by (Boger et al., 1998) in RANS to describe the resolved FSD and a similarity concept is employed for the unresolved portion, wherein the unresolved FSD is assumed to be similar, in location and order of magnitude to the contribution evaluated at the resolved scales. (Richard et al., 2007) formulated commonly used CFM-RANS in LES context for studying cyclic variation in spark ignition engines. Their work demonstrates the feasibility of LES of engine cycles simulation by using a flame surface density (FSD) approach. The results of phenomenological balanced transport equation for FSD were compared to those obtained with the algebraic model for the FSD proposed by (Boger et al., 1998) and the need for non-equilibrium combustion models was demonstrated.

3.7 Coherent Flame Model (CFM)

Originally, the concept of solving a modelled transport equation for flame surface density was applied to the non-premixed turbulent combustion by (Marble and Broadwell, 1977). Since then, there have been many studies of the approach in turbulent premixed combustion. (Marble and Broadwell, 1977), employed the coherent flame model to describe the physical processes that create and destroy flame surface area. Further analysis have led to an exact transport equation for the flame surface density based on theoretical considerations for a propagating surface as given by (Pope, 1988) and (Candel and Poinsot, 1990).

The CFM simplifies the turbulent combustion problem by separating the combustion modeling from the analysis of the turbulent flow field. The flamelet model implies that the reaction takes place in the relatively thin layers that separate regions of unburned and fully burned gases. Considering a single step chemistry, unity Lewis number and flamelet regime, the thermo chemistry of the reacting flow can be described by the transport equation of progress variable c of the reaction , c = 0 in fresh gases and c = 1 in fully burned gases

$$c = \frac{Y_f - Y_f^u}{Y_f^b - Y_f^u} \tag{3.12}$$

where, Y_f is fuel mass faction, superscripts u and b representing unburnt and burnt mixture.

Favre filtered progress variable transport equation is given as,

$$\frac{\partial \bar{\rho}\tilde{c}}{\partial t} + \nabla.(\bar{\rho}\tilde{u}\tilde{c}) + \nabla.\left[\bar{\rho}(uc - \tilde{u}\tilde{c})\right] = \overline{\nabla.(\rho D \nabla c)} + \overline{\dot{\omega}_c} \tag{3.13}$$

where, the over bar (–) denotes a filtered quantity and the tilde (~) a Favre-

filtered quantity. There are three unknown terms, the subgrid scale reaction progress variable flux (third term on the left-hand side), the filtered molecular diffusion (first term on the right-hand side) and the subgrid scale reaction rate (second term on the right-hand side). The unresolved scalar fluxes are generally described from a simple gradient assumption and written as turbulent diffusion

$$\left[(uc-\tilde{u}\tilde{c})\right]=-\frac{\nu_t}{Sc_t}\frac{\partial\tilde{c}}{\partial x_i} \tag{3.14}$$

The analysis of the DNS database by (Boger et al., 1998) has shown that gradient or counter-gradient unresolved fluxes may be observed in LES like in RANS depending on the turbulence level and heat release rate, But unresolved LES fluxes are lower than in RANS so that model uncertainties have less dramatic consequences in LES than in RANS.

Counter-gradient transport may be explained by differential buoyancy effects between cold heavy fresh and hot burnt gases at all characteristics lengths scales. Accordingly the unresolved scalar flux increases almost linearly with the filter size 'Δ', without the change in the type – gradient or counter gradient. Therefore a portion of the counter gradient phenomena is directly described in LES through resolved motions, even when a gradient type subgrid scale closure is used (Poinsot and Veynante, 2005).

The high gradients within the thin flame allow a balance to be established between molecular transport and chemistry. This implies that diffusive transport and chemical reactions cannot be modelled independently of each other.

$$\overline{\nabla.(\rho D\nabla c)}+\overline{\dot{\omega}_c}=\overline{\rho S_d|\nabla c|} \tag{3.15}$$

$$\overline{\rho S_d|\nabla c|}\approx\rho_u S_l\Sigma=\rho_u S_l\Xi_\Delta|\nabla\overline{c}| \tag{3.16}$$

Where, Σ is the subgrid scale flame surface density (flame surface per unit volume) and Ξ_Δ is the subgrid scale flame wrinkling factor - the ratio between the subgrid fame surface and its projection in the propagating direction. Models are required for Σ and Ξ_Δ. Various modelling approaches like algebraic (Boger et al., 1998, Charlette et al., 2002b), similarity model (Knikker et al., 2002) and balance transport equation (Boger et al., 1998), (Hawkes and Cant, 2000, Richard et al., 2007) have been used for subgrid flame surface density or for flame wrinkling factor (Weller et al., 1998a). The particular models relating to flame surface density quantity are more popular as FSD is physically well defined quantity and may be extracted from DNS or experimental measures for validation studies.

In the present work, the algebraic model proposed by (Charlette et al., 2002b) and the balanced transport model proposed by (Richard et al., 2007) are considered for closure of FSD. In the following section both the models for FSD are discussed in detail

3.7.1 Algebraic model

The coupling of flame propagation and unresolved turbulence is modelled according to the subgrid scale combustion model.

$$\Xi_\Delta=\left(1+\frac{\Delta}{\eta_c}\right)^\beta=\left(1+\min\left[\frac{\Delta}{\delta_l},\Gamma\left(\frac{\Delta}{\delta_l},\frac{u'_\Delta}{S_L},\mathrm{Re}_\Delta\right)\right]\frac{u'_\Delta}{S_L}\right)^\beta \tag{3.17}$$

In equation 3.16, the subgrid flame wrinkling factor (Ξ_Δ) is written in terms of

a power-law expression involving an inner cut-off scale η_c, an outer cut-off scale (the filter scale) Δ, and the parameter β as an exponent. The inner cut- off length scale is defined as the inverse mean curvature of the flame, limits wrinkling at the smallest length scales of the flame. η_c is modelled by introducing an efficiency function Γ, which takes into account the net straining effect of all relevant turbulent scales smaller than the filter size Δ. A spectral analysis of the DNS results of elementary flame–vortex interactions by (Colin et al., 2000) was performed to construct Γ as a function of the filter scale to laminar flame thickness ratio Δ/δ_l, the subgrid scale turbulent velocity to laminar burning velocity ratio u'/S_L and the subgrid scale turbulent Reynolds number Re_Δ. Later (Charlette et al., 2002a) proposed efficiency function as a function of flame thickness ratio and velocity ratio only. The details of the (Charlette et al., 2002a) efficiency function are discussed in details in the next following section. Furthermore, efficiency function was corrected such that the eddies whose characteristic speed falls below $S_l/2$ do not wrinkle the flame. The presence of the 'min' operator in equation 3.17, is due to the fact that the model could predict inner cut-off scales smaller than the laminar flame thickness δ_l. To avoid this problem the expression was clipped at the laminar flame thickness. The equation 3.17 is essentially a flame wrinkling model that however, works well also beyond the wrinkled regime of combustion (Charlette et al., 2002a, Charlette et al., 2002b).

3.7.2 Balanced transport equation

In the present work, the modeling for the FSD transport equation is based on the work of (Richard et al., 2007). The Σ-transport equation provides a proper description of the flame surface dynamics and closure models are required for individual terms.

$$\frac{\partial \overline{\Sigma}_{\tilde{c}+}}{\partial t} + T_{res} + T_{sgs} = S_{res} + S_{sgs} + C_{res} + C_{sgs} + P \tag{3.18}$$

where, T_{res}, S_{res}, C_{res} and P are respectively the transport , strain , curvature and propagation terms due to resolved flow motions and T_{sgs}, S_{sgs} and C_{sgs} are respectively the unresolved transport , strain and curvature terms.

3.7.2.1 Modeling of the flame propagation and curvature

The propagation term P and resolved curvature term C_{res} are physically linked and ensure the laminar flame propagation, when the subgrid scale turbulence is low. The proposed formulation is based on the normal $N = {-\nabla \overline{c}}/{|\nabla \overline{c}|}$ to the iso-surface of the filtered progress variables and given as

$$P = -\nabla.(S_d N \overline{\Sigma}_{\tilde{c}}) \tag{3.19}$$

$$C_{res} = S_d (\nabla.N) \overline{\Sigma}_{\tilde{c}} \tag{3.20}$$

where, S_d is the flame displacement speed, which is the difference between the flame front velocity and the flow velocity evaluated as $S_d = (1 + \tau \tilde{c}) S_l$ with $\tau = \frac{\rho_u}{\rho_b} - 1$ is the thermal expansion rates across the flame front also known as heat release factor. Typically the value of heat release factor lies between

5 - 7 for most of the premixed flames. The FSD destruction associated with the effect of propagation and curvature vanishes when the flame is planar.

The subgrid scale curvature term C_{sgs} represents the influence of the unresolved curvature on the flame front wrinkling. DNS simulations by (Trouve et al., 1994), have shown that the subgrid curvature acts as a sink term towards burned gases and as source term towards fresh gases. The subgrid scale curvature is formulated by (Rymer, 2001) and corrected for the $\overline{\Sigma}_{\tilde{c}}$ as

$$C_{sgs} = \beta S_l \frac{(c^* - \overline{c})}{(\overline{c}(1-\overline{c}))} (\overline{\Sigma}_{\tilde{c}} - \overline{\Sigma}_{\tilde{c}}^{lam}) \overline{\Sigma}_{\tilde{c}} \tag{3.21}$$

where, $\overline{c}$ is unweighted filtered progress variable estimated as $\overline{c} = \frac{(1+\tau)\tilde{c}}{(1+\tau\tilde{c})}$ and laminar part of Favre filtered flame surface density is given as $\overline{\Sigma}_{\tilde{c}}^{lam} = |\nabla \tilde{c}| + (\overline{c} + \tilde{c}) \nabla . N$, with $\beta = 4/3$ and $c^* = 0.5$ are modeling constants.

3.7.2.2 Modeling of flame strain rate

The resolved strain S_{res} corresponds to the flame strain rate due to resolved flow eddies. The flame strain rate due to the resolved flow field is modelled as

$$S_{res} = (\nabla . \tilde{u} - NN : \nabla \tilde{u}) \overline{\Sigma}_{\tilde{c}} \tag{3.22}$$

The operator $(NN : \nabla \tilde{u})$ represents the gradient operator normal to the flame surface and is written in index form as

$$NN : \nabla \tilde{u} = \left[n_i n_j \frac{\partial \tilde{u}_i}{\partial x_j} \right] \tag{3.23}$$

The S_{res} term mainly acts as a production term throughout the flame front.

The subgrid scale strain (S_{sgs}) accounts for the influence of unresolved structures on the flame front. This term is usually modelled as proportional to the inverse of turbulent timescale. Differently sized vortices have different effect in terms of straining the flame, depending on their relative size of the vortices compared with the laminar flame thickness and the propagation speed (Hawkes and Cant, 2000). The intermittent turbulent net flame stretch (ITNFS) model proposed by (Meneveau and Poinsot, 1991) tend to reproduce the straining effects depending on the local characteristics of the flame. The straining term is multiplied by an efficiency function Γ, which takes into account the ability of all vortices to wrinkle the flame and depends on the relative velocity u'/S_l and the relative length scale Δ/δ_l. (Colin et al., 2000) have showed that resolved eddies smaller than the flame thickness defined by $\hat{\Delta}=n_{res}\Delta_x$ are not able to wrinkle the flame front, typical value of n_{res}~ 5-10 for finite volume solvers (n_{res} can also be treated as flame resolution factor) Therefore the combustion filter size is $\hat{\Delta}$ and not the momentum filter Δ_x. The subgrid scale strain is accordingly defines as

$$S_{sgs}=a_t\overline{\overline{\Sigma}}_{\tilde{c}}=\Gamma\left(\frac{\hat{u}'}{S_l},\frac{\hat{\Delta}}{\delta_l}\right)\frac{\hat{u}'}{\hat{\Delta}}\overline{\overline{\Sigma}}_{\tilde{c}} \tag{3.24}$$

where, a_t is turbulent strain rate , $\hat{u}'$ is turbulent velocity fluctuation at filter scale $\hat{\Delta}$. It is estimated from the subgrid scale turbulence velocity fluctuation assuming kolmogorov cascade as $\hat{u}'=u'(\hat{\Delta}/\Delta_x)^{1/3}$, subgrid turbulence velocity fluctuation (u') is estimated for subgrid kinetic energy. The efficiency function Γ is proposed by (Charlette et al., 2002b) based on DNS studies of elementary flame-vortex at single length and velocity scales is been adopted

in the present work (corrected for the subgrid scale quantities $\hat{\Delta}$ and $\hat{u}'$). Following is the adopted efficiency function,

$$\Gamma\left(\frac{\hat{u}'}{S_l},\frac{\hat{\Delta}}{\delta_l}\right)=[((f_{\hat{u}'}^{-a}+f_{\hat{\Delta}}^{-a})^{-b}+f_{\mathrm{Re}}^{-b})^{-1/b} \tag{3.25}$$

where,

$$f_{\hat{u}'}=4\left(\frac{27C_k}{110}\right)^{1/2}\left(\frac{18C_k}{55}\right)\left(\frac{\hat{u}'}{S_l}\right)^2 \tag{3.26}$$

$$f_{\hat{\Delta}}=\left[\frac{27C_k\pi^{4/3}}{110}\left(\left(\frac{\hat{\Delta}}{\delta_l}\right)^{4/3}-1\right)\right]^{1/2} \tag{3.27}$$

$$f_{\mathrm{Re}}=\mathrm{Re}_{\hat{\Delta}}^{1/2}\left[\frac{9}{55}\exp\left(-\frac{3}{2}C_k\pi^{4/3}\mathrm{Re}_{\hat{\Delta}}^{-1}\right)\right]^{1/2} \tag{3.28}$$

$$\mathrm{Re}_{\hat{\Delta}}=4\left(\frac{\hat{\Delta}}{\delta_l}\right)\left(\frac{\hat{u}'}{S_l}\right) \tag{3.29}$$

$C_k\approx1.5$ is the Kolmogorov constant. The exponents *a* and *b* control the sharpness of the transition between the asymptotic behaviours and good results were obtained with

$$a=0.60+0.20\exp\left[-0.1\left(\frac{\hat{u}'}{S_l}\right)\right]-0.20\exp\left[-0.01\left(\frac{\hat{\Delta}}{\delta_l}\right)\right],\ b=1.4 \tag{3.30}$$

The graphical representation of the efficiency function (equation 3.25) is been shown figure 3.4 for various values of relative velocity and relative length scales. The arrow mark on the plot indicates the direction of increase in relative length scale values.

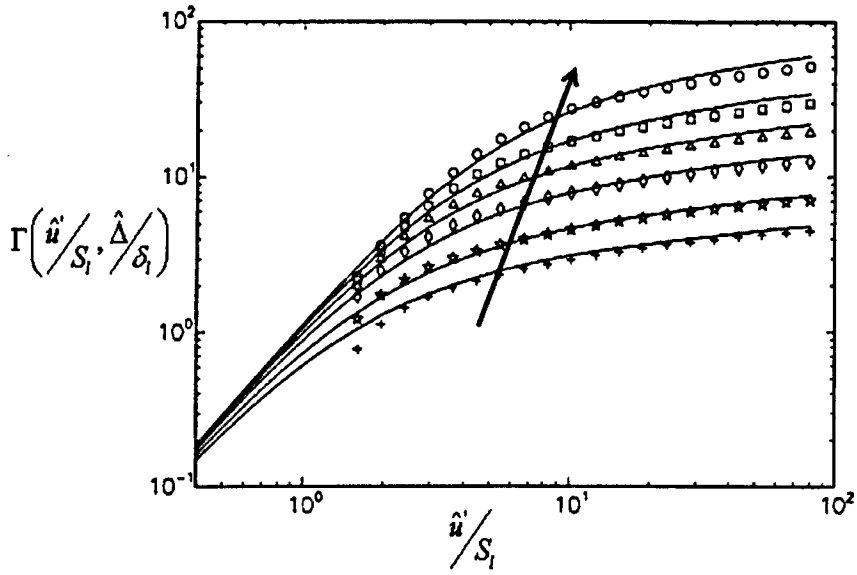

Figure 3.4. Efficiency function for different values of $\hat{\Delta}/\delta_l = 10, 20, 50, 100, 200 \& 500$ (Charlette et al., 2002a).

3.7.2.3 Modeling flame surface density transport term

The resolved transport term T_{res} takes into account the effect of mean flow convection on the flame front, which is modelled as

$$T_{res} = \nabla.(\tilde{u}\bar{\Sigma}_{\tilde{c}}) \tag{3.31}$$

The unresolved transport is closed under a gradient assumption and given as standard turbulent diffusion term based on combustion filter scale $\hat{\Delta}$.

$$T_{sgs} = -\nabla\left(\frac{\hat{\nu}_t}{Sc_t}\nabla\bar{\Sigma}_{\tilde{c}}\right) \tag{3.32}$$

where, $\hat{\nu}_t$ is turbulent viscosity at filter scale $\hat{\Delta}$. It is evaluated from the subgrid scale terms as $\hat{\nu}_t = C\hat{u}'\hat{\Delta}$ with C = 0.12 as model constant.

3.7.2.4 Flame thickness control factor (σ_c)

In complex geometries the mesh can hardly be maintained as uniform. (Richard et al., 2007) proposed flame thickness factor (σ_c) similar to thickened flame approach TF-LES (Colin et al., 2000) to adapt FDS propagation to non-regular mesh. The flame brush thickness is controlled by a balance between the turbulence transport and source terms of the FSD equation 3.16. Integrating the FSD equation for 1D steady flame, the natural flame brush thickness δ_{bt} is

$$\delta_{bt}=\frac{4S_l(\Xi_{eq}-1)\dfrac{\beta}{1+\tau}\left(1+\tau\left(\dfrac{1}{2}+\dfrac{\tau}{3}\right)-c^*\left(1+\tau+\dfrac{\tau^2}{3}\right)\right)}{a_t} \tag{3.33}$$

where, Ξ_{eq} is the equilibrium wrinkling factor given by the KPP analysis (Duclos et al., 1993)

$$\Xi_{eq}=\frac{S_{T_{KPP}}}{S_l}=1+\frac{2}{S_l}\sqrt{\frac{\hat{\nu}_t a_t}{1-\beta c^*/(1+\tau)}} \tag{3.34}$$

The δ_{bt} evolves from the subgrid scale turbulence and vary in typical numerical simulations from $5\Delta_x$ to $50\Delta_x$, which corresponds to respectively to over-resolved and under-resolved of the flame front. In order to ensure a constant resolution of flame front on certain number of mesh points (n_{res}), a correction factor (σ_c) is introduced in the expression of diffusivity and subgrid scale strain by replacing $\hat{\nu}_t$ with $\sigma_c\hat{\nu}_t$ and a_t with a_t/σ_c , where σ_c is defined as $\sigma_c=n_{res}\Delta_x/\delta_{bt}$. To avoid modifying the mixing processes involved in the species and energy transport equation outside the flame front, a dynamic procedure is adopted: the diffusivity $\sigma_c\hat{\nu}_t$ is only used inside the resolved

flame front and out of the reaction zone ν_t corresponding to standard diffusivity model is retained. The final CFM-LES combustion model equation proposed by (Richard et al., 2007) is

$$\frac{\partial}{\partial t}(\bar{\rho}\tilde{c})+\nabla.(\bar{\rho}\tilde{u}\tilde{c}) =\nabla.(\sigma_c\mu_{eff}\nabla\tilde{c})+\rho_u S_l\overline{\Sigma}_{\tilde{c}} \tag{3.35}$$

$$\frac{\partial\overline{\Sigma}_{\tilde{c}}}{\partial t}+\nabla.(\tilde{u}\overline{\Sigma}_{\tilde{c}})-\nabla.(\sigma_c\mu_{eff}\nabla\overline{\Sigma}_{\tilde{c}})=(\nabla.\tilde{u}-NN:\nabla\tilde{u})\overline{\Sigma}_{\tilde{c}}+\Gamma\left(\frac{\hat{u}'}{S_l},\frac{\hat{\Delta}}{\delta_l}\right)\frac{\hat{u}'}{\hat{\Delta}}\overline{\Sigma}_{\tilde{c}}/\sigma_c$$

$$+S_d(\nabla.N)\overline{\Sigma}_{\tilde{c}}+\beta S_l\frac{c^*-\bar{c}}{\bar{c}(1-\bar{c})}(\overline{\Sigma}_{\tilde{c}}-\overline{\Sigma}_{\tilde{c}}^{lam})\overline{\Sigma}_{\tilde{c}}-\nabla.(S_d N\overline{\Sigma}_{\tilde{c}}) \tag{3.36}$$

3.8 Lewis number effect

Lewis number (Le) is the ratio of thermal diffusivity to mass diffusivity of a deficient reactant.

$$Le=\frac{\alpha}{\rho C_p D_k}=\frac{D_{th}}{D_k} \tag{3.37}$$

It's difficult to define a single unique Lewis number for a premixed combustion due to presence of different species with different thermo-physical properties. To simplify the analysis of multispecies mixture is characterized by Lewis number of deficient reactant. The flame temperature depends on relative rate of heat and mass diffusion at the flame front. If the diffusivities are equal i.e., Le = 1 then the total energy is conserved and the flame temperature is adiabatic temperature, however if Le > 1, heat loss exceeds the gain in the concentration of the deficient species and flame temperature is less than adiabatic temperature. For Le < 1, heat loss is less than the gain in mass of

deficient species and hence the flame temperature is higher than adiabatic flame temperature.

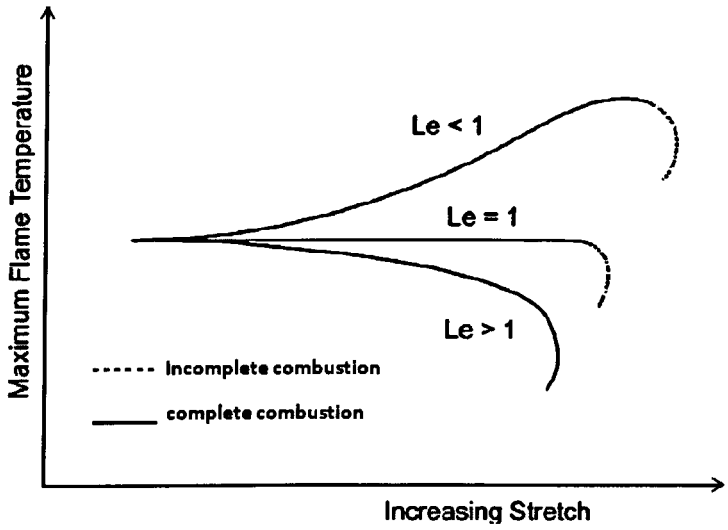

Figure 3.5. Effect of stretch, non-equidiffusion and completeness of reaction on the maximum flame temperature (reproduced from (Law, 2006))

Flame stretch has minimal effect on an adiabatic, unrestrained, diffusionally-neutral flame with complete reaction (Flame stretch is defines as the sum of the tangential strain rate and curvature on the flame front). The temperature, propagation rate, and thickness of the flame are invariant to stretch, and that stretch alone cannot extinguish such a flame. In such cases the extinction of flame is possible due to incomplete combustion process. In the presence of preferential diffusion and/or when the flame movement is restrained, the response of the flame to stretch becomes more sensitive and extinction is possible (Law et al., 1988, Law, 1989).

The effect of non-equidiffusion, stretch rate and completeness of reaction on flame temperature is summarized in figure 3.5. The interaction of

non-unity Lewis number (due to preferential diffusion and/or unequal rates of heat and mass transfer) with the coupled effect of radiation, chemistry and unsteadiness alters several characteristics of a flame. (Chakraborty and Cant, 2006, Chakraborty and Cant, 2009) used three-dimensional compressible DNS of statistically planar flames to study the effects of tangential strain rate on the displacement speed of turbulent premixed flames in the thin reaction zones. For non-unity Lewis numbers it was found that the variations of temperature and scalar gradient in response to tangential strain rate on a given reaction progress variable isosurfaces have a profound influence on displacement speed behaviour. In the case of $Le = 0.8$, temperature and tangential strain rate are found to be positively correlated at locations of zero curvature whereas the opposite behaviour is apparent for the case of $Le = 1.2$. It was demonstrated that the effects of the temperature-curvature and tangential strain rate-curvature correlations are implicitly present in the response of the temperature to local strain rate. Under the same initial conditions of turbulence, flames with low Lewis numbers are found to exhibit counter-gradient transport, whereas flames with higher Lewis numbers tend to exhibit gradient transport. The strength of dilatation rate is found to increase with decreasing Lewis number and this effect becomes particularly strong for the flames with $Le < 1$ because of thermo-diffusive instability. The dilatation rate is responsible for the preferential alignment of the reactive scalar gradient with the most extensive principal strain rate in the reaction zone for flames with Le close to unity, contrary to the alignment of scalar gradient with the most compressive principal strain rate in turbulent passive scalar transport. The scalar gradient alignment with local strain rate plays an

important role in the transport of scalar dissipation rate and the flame surface density. The influence of non-unity Lewis numbers of oxidant and fuel vapours was investigated experimentally by (Greenberg and Ronney, 1993). In this study the Lewis number of the oxidant affects the spread rate only through its effect on the flame temperature and the fuel Lewis number plays no role at all. Good agreement between a zeroth order formula for the flame spread velocity and experimental results indicated that unity Lewis number assumptions can lead to rather inaccurate spread rate and flame temperature predictions. For most gases Lewis no is close to unity, hydrogen is an exception with strong bias towards mass diffusivity with Le ~ 0.3.

3.9 Limitations of CFM-LES

- Coherent Flame Model formulation is based on unity Lewis no. as discussed in section 3.8, flame stretch do not influence the flame temperature and hence of flame quenching is only possible by heat loss and incomplete combustion.
- The source terms in the Flame Surface Density balance equation are proportional to either Σ or Σ^2, implicitly assumes the flame surface density is established, therefore the equation cannot generate the flame surface density where there is no initial flame surface in CFM.
- Requires ignition models outside CFM modeling to generate initial flame surface density to establish the flame front. CFM balance equation is only valid, when flame front is pre existing. Hence CFM-LES cannot simulate spark ignition process.

3.10 Summary

Turbulent combustion process involves various lengths, velocities and time scales describing turbulent flow field and chemical reactions. Therefore the derivation of the combustion models depends on the physical analysis and comparison of these time and length scales. Flamelet approach of turbulent combustion assume that reaction takes place in relatively thin layers that separate regions of unburned and fully burned gases thereby simplify the turbulent combustion problem by separating the combustion modeling from the analysis of the turbulent flow field.

Coherent flame model have been widely used in RANS and recently been extended to LES is particularly attractive as the modeling parameters - Flame Surface Density and laminar flame speed are physically well defined quantity and may be extracted from DNS or experimental measures for validation studies. The Σ-transport equation provides a proper description of the flame surface dynamics. Closure models are required for individual terms, involving the transport, strain, curvature and propagation due to resolved and unresolved flow motions in the Σ transport equation. CFM transport equation can only propagate the existing flame surface density and cannot generate the flame surface density where there is no initial flame surface. Finally, the effect of non-equidiffusion, stretch rate and completeness of reaction on maximum flame temperature are discussed briefly.

Chapter 4

FLOW-WALL INTERACTIONS

4.1 Introduction

The presence of solid surface in fluid flows introduces 'wall' physical boundary condition. The fluid viscosity enforces the no-slip condition and acts as a sink for momentum leading to a characteristic length scale near the wall that is viscosity dominated. Ludwig Prandtl (1900) was the first to propose two region solution for fluid layer near the surface, where viscous forces dominate to the region far away from the surface where the inertial forces dominate, the latter region is known as boundary layer.

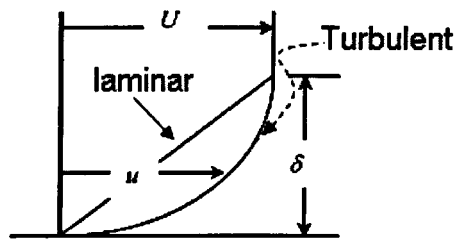

Figure 4.1 Velocity profile on a flat plate (laminar & turbulent)

The linear relationship in laminar flows between the wall shear stress and velocity enables a simplified method of capturing the wall effects

$$\tau_w = \rho \nu \left. \frac{\partial \langle U_p \rangle}{\partial y} \right|_w \tag{4.1}$$

where τ_w is the wall shear stress, ν is the kinematic viscosity, y is the normal distance of the first grid point from the wall, and $\langle U_p \rangle$ is the mean velocity at

that point (p) relative to the wall. However, in a turbulent flow, this relationship is no longer linear as shown in figure 4.1. The kinematic viscosity (v) and the wall shear stress (τ_w) are the two important parameters in the near wall region. From these quantities appropriate viscous scales i.e. length and velocity scales in the near-wall region are defined. They are the friction velocity,

$$u_\tau = \sqrt{\frac{\tau_w}{\rho}} \tag{4.2}$$

and the viscous length scale,

$$\delta_v = v\sqrt{\frac{\rho}{\tau_w}} = \frac{v}{u_\tau} \tag{4.3}$$

The distance from the wall is non dimensionalised using viscous length scale and termed as wall units denoted by

$$y^+ = \frac{y}{\delta_v} = \frac{u_\tau y}{v} \tag{4.4}$$

The friction Reynolds number is an important parameter in turbulent flow, which is defined as

$$\mathrm{Re}_\tau = \frac{u_\tau l_c}{v} = \frac{l_c}{\delta_v} \tag{4.5}$$

Where, l_c is flow characteristic length. The wall shear velocity is chosen as the flow characteristic velocity as most of turbulence in the flow is due to the interaction of the flow with the solid boundary and the flow velocity away from the solid boundaries can be misleading. Moreover two flows can be fundamentally different with same centreline velocity as shown in figure 4.1, thus u_τ will distinguish between these two flows (Berselli et al., 2006).

The wall modeling problem in LES is nothing but a particular subgrid modeling problem, which arises when the first computational cell at the wall is too coarse to allow for a direct capture of the large turbulent scales that are present in the inner part of the turbulent boundary layer. Since the first grid cell at the wall is too coarse, the usual no-slip boundary condition must be replaced by another condition (wall models) which accounts for the details of the sub-grid motion. To avoid the placement of a large number of grid points near a wall, a wall model is generally used to capture near-wall effects. These models are empirical boundary conditions that bridge the gap in the wall region. since most wall models are developed by simplifying assumptions and tested in simple flows. These models are not easily applicable to cases involving streamwise and spanwise surface curvatures, pressure gradients, and separation as in complex geometry.

In the remaining part of the chapter, the structure of the flat turbulent boundary layer is discussed in brief, followed by comments on compressible turbulent boundary layer – Morkovin hypothesis. Modeling strategies to address the flow-wall interactions in LES are presented. Followed by the details of the adopted flow-wall model in the present study. Finally this chapter is concluded after discussion about the validation case study.

4.1.1 Structure of the turbulent boundary layer

Different regions in the near wall flow can be identified on the basis of y^+ values (Pope, 2000). In figure 4.2, a typical turbulent boundary layer profile on flat plate is been shown. Following are the regions identified as, Viscous sublayer ($y^+ < 5$) - the Reynolds shear stress is negligible compared with the

viscous stress. At the surface all the stress is viscous stress. Log-law region ($y^+ > 30$) - in this region the log-law holds for the mean velocity profile. The inertial forces are dominant than viscous forces. Buffer layer ($5 < y^+ < 30$) - the region between the viscous sublayer and the log-wall region.

Another way of identifying the near wall region is in terms of 1) inner layer (y+ < 50), there is a direct effect of molecular viscosity on the shear stress, this region is also known as Viscous wall region and 2) Outer layer ($y^+ > 50$), in this region the effect of viscosity is negligible. It's also known as velocity defect law region.

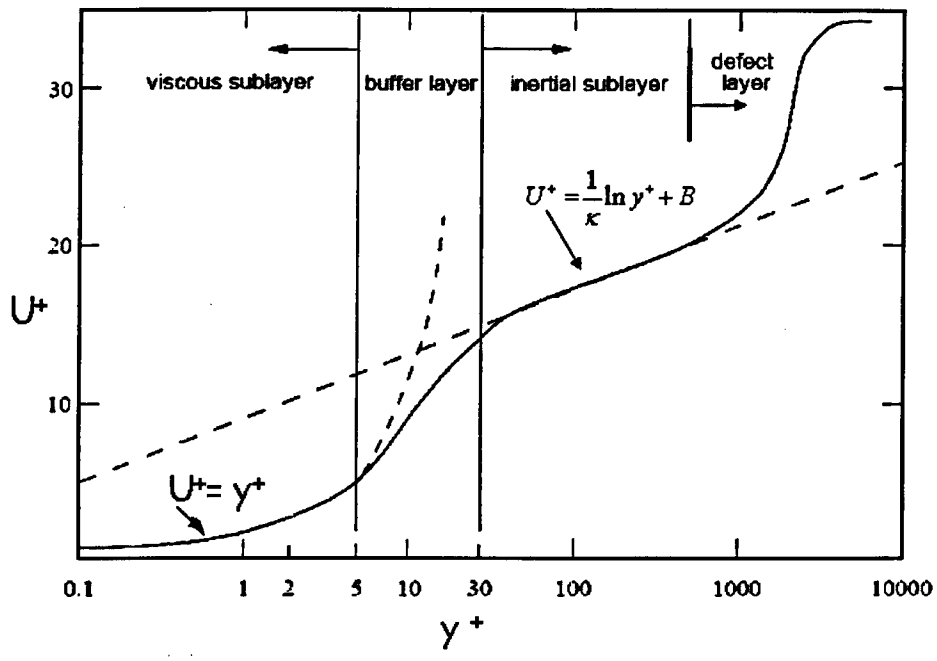

Figure 4.2. Typical flat plate turbulent boundary layer profile

4.1.2 Compressible turbulent boundary layer

The compressibility effects are negligible in low Mach number flows. Density behaves as a passive scalar or as a fluid property, and the vorticity production

due to baroclinic torque remains small. One of the more widely used hypotheses for the analysis and computation of compressible turbulent boundary layer is Morkovin hypothesis. This hypothesis was developed in 1962 by Morkovin from an analysis of supersonic boundary layer data. He concluded that for moderate Mach number ($Ma \leq 5$) the essential dynamics of the shear flows will follow the incompressible pattern. The hypothesis was used and reframed by (Bradshaw, 1974) to indicate that high-speed boundary layers can be computed using the same model as at low speeds by assuming that the density fluctuations are weak. The application of Morkovin's hypothesis is essentially limited to boundary layer. However the characterization of compressible turbulence depends on the level of fluctuating divergence $\nabla.u'$ that is proportional to the material derivatives of density $D(\rho'/\rho)Dt$ rather than to the density fluctuation ρ'/ρ itself. Both experiments and numerical simulations confirmed that at moderate Mach numbers, the essential dynamics of the investigated supersonic turbulent boundary layers closely resemble the incompressible pattern under analogous conditions (Coleman et al., 1995, Huang et al., 1995, Lenormand et al., 2000, Brun et al., 2008).

4.2 Modelling strategies

Near a solid surface, all turbulent structures are small and the grid resolution has to very fine to resolve even the energy-carrying structures. Large numbers of grid points are required to adequately resolve the steep velocity gradients and to compute the wall stress accurately makes LES also an expensive method. The cost of wall-resolved LES based on a flat plate was

estimated by (Chapman, 1979, Choi and Moin, 2012) to be proportional to $Re^{13/7}$. It is well known that the scaling of the near-wall structures is strongly dependent on the Reynolds number, thus limiting wall-resolved LES computations to fairly low Reynolds number. For flows of engineering interest Reynolds numbers are in the range of 10^6 - 10^9, resolving the near wall region is not computationally feasible, hence appropriate wall modeling is required to capture wall effects. One such modeling is to use approximate boundary conditions similar to the wall functions applied in RANS simulations with turbulence models. These boundary conditions are known as equilibrium-stress models and assume the existence of an equilibrium layer in which the stress is constant. This results in the existence of a logarithmic layer that can be used to relate the velocity in the outer layer to the wall stress.(Deardorff, 1970, Schumann, 1975, Werner and Wengle, 1993) This method allows one to place the first grid point in the logarithmic region and thus avoid simulating the wall layer altogether. Since the wall layer structures don't have to be resolved, the grid can be quite coarse in spanwise and streamwise directions.

Another approach consists of keeping a fine grid at the wall but solving simplified set of equations weakly coupled to the outer flow. This approach was first employed by (Balaras et al., 1996) who used simplified set of equations, using thin-boundary-layer assumption, in the inner layer.

The Detached Eddy Simulation (DES) is another method introduced by (Spalart, 2000) which switches from LES in the core of the flow to RANS in the wall vicinity. A lot of works has more recently been devoted to the development of the so-called hybrid methods, using RANS equations in the inner layer, while LES equations are solved away from the wall. A recent

review of wall model used in LES can be found in various references (Cabot and Moin, 2000, Piomelli and Balaras, 2002, Piomelli, 2008) .

In flows with complex geometries, the assumption of an equilibrium boundary-layer is not valid, in particular flows with boundary-layer separation. The favourable or adverse pressure gradient acts as a non-equilibrium term for the boundary-layer. To take this effect into account, (Manhart et al., 2008) proposed a model including the streamwise pressure gradient considering thin boundary layer equations. However, the Reynolds stresses were neglected in their formulation limiting the validity range of the model to the viscous sublayer, i.e. the first grid point from the wall should be placed in the $y^+ < 5$ region. (Duprat et al., 2011) extended the work of (Manhart et al., 2008) taking into account both the streamwise pressure gradient and the Reynolds stresses effects. This new model provides an analytical formulation for the streamwise velocity variation as a function of the distance to the wall. The model proposed by (Duprat et al., 2011) is adopted in the present study to model the flow-wall interactions. In the following section the formulation of this model is discussed in detail.

4.3 Wall layer model with/out pressure gradient

For the boundary layer, a simplified averaged set of partial equations can be derived from the Navier-Stokes equation neglecting the horizontal viscous diffusion terms and fixing the pressure gradient to the outer flow value. as shown in equation 4.6. The set of equations are known as the unsteady thin-boundary-layer equations (TBLE). In case of LES, it is assumed that the filtered velocity is equivalent to the averaged velocity close to the wall. This

assumption is valid, if cells are coarse enough close to the wall to contain a large number of eddies and if the time step is much larger than the time scale characteristic of the near wall eddies.

$$\frac{\partial U_i}{\partial t}+\frac{\partial U_i U_j}{\partial x_j}+\frac{1}{\rho}\frac{\partial P}{\partial x_i}=\frac{\partial}{\partial y}\left[(\upsilon+\upsilon_t)\frac{\partial U_i}{\partial y}\right] \tag{4.6}$$

where, v is kinematic viscosity, U_i is the mean velocity in the direction x_i and y is the direction normal to the wall. The Reynolds stresses are modelled through a turbulent eddy viscosity assumption (v_t). The streamwise pressure gradient is assumed to be constant in the wall normal direction. Further simplification of equation 4.6 is done by neglecting the first two terms on the left hand side leading to,

$$\frac{1}{\rho}\frac{\partial P}{\partial x_i}=\frac{\partial}{\partial y}\left[(\upsilon+\upsilon_t)\frac{\partial U_i}{\partial y}\right] \tag{4.7}$$

Integrating the equation 4.7 in the wall normal direction leads to,

$$0=(\upsilon+\upsilon_t)\frac{\partial U}{\partial y}-\frac{1}{\rho}\frac{\partial P}{\partial x}y-\frac{\tau_w}{\rho} \tag{4.8}$$

where, $\tau_w=\rho\upsilon\left.\frac{\partial U}{\partial y}\right|_{y=0}$ is wall shear stress. Rearranging the equation 4.8 to

$$\frac{\partial U}{\partial y}=\frac{\frac{\partial P}{\partial x}y+\tau_w}{\rho(\upsilon+\upsilon_t)} \tag{4.9}$$

Momentum equation 4.9 is then scaled with the extended inner scaling proposed by (Manhart et al., 2008) for the wall layer. This scaling is denoted by a superscript *. The scaling takes into account wall shear stress and the streamwise pressure gradient in terms of nondimensional velocity U* and nondimensional length y* defined as

$$U^* = \frac{U}{u_{\tau p}} \quad , \quad y^* = \frac{y u_{\tau p}}{\nu} \tag{4.10}$$

where, $u_{\tau p} = \sqrt{u_\tau^2 + u_p^2}$ is a combination velocity using the classical friction velocity at the wall, $u_\tau = \sqrt{|\tau_w|/\rho}$ and an additional velocity based on the streamwise pressure gradient, $u_p = \left|(\mu/\rho^2)(\partial P/\partial x)\right|^{1/3}$ proposed by (Simpson, 1983) . one of the advantage of this scaling is that it stays valid even for separation or reattachment region as opposed to the classical wall coordinates (u_τ) .a dimensional parameter $\alpha = u_\tau^2 / u_{tp}^2 \in [0,1]$ can be used to quantify the predominant effect between shear stress and streamwise pressure gradient. $\alpha = 0$ corresponds to a zero shear stress flow, a separation point, and $\alpha = 1$ corresponding to a zero pressure gradient flow. The nondimensional formula can be deduced to following equation using the extended scaling,

$$\frac{\partial U^*}{\partial y^*} = \frac{sign\left(\frac{\partial P}{\partial x}\right)(1-\alpha)^{3/2} y^* + sign(\tau_w)\alpha}{\left(1 + \frac{\nu_t}{\nu}\right)} \tag{4.11}$$

The comparison between the pressure gradient sign and the wall shear sign allows knowing if the pressure gradient is adverse or favourable. The eddy viscosity in equation 4.11 is unknown quantity and required to be modelled, which is been dealt in the next section.

4.3.1 Turbulent eddy viscosity model

The usual approach of modeling the turbulent eddy viscosity is by the ad hoc damped mixing length to approximate both the linear and inertial region. The

original Van Driest formula predicted very well the velocity profile for boundary layers with zero pressure gradients. It has given unsatisfactory results for flows with non zero pressure gradient. This has prompted many investigators to propose modifications for this turbulent viscosity to take the pressure gradient into account. Based on the works of (Balaras et al., 1996) the eddy viscosity is here defined as

$$\frac{\nu_t}{\nu}=\kappa y^*[\alpha+y^*(1-\alpha)^{3/2}]^{\beta}(1-e^{-y^*/(1+A\alpha^3)})^2 \tag{4.12}$$

where, $\kappa=0.42$ is the von Karman constant. The constant A and β are determined by (Duprat et al., 2011) through a priori tests based on DNS calculations of three different boundary layer scenarios to be β= 0.78 and A=17 . The two equations 4.11 & 4.12 together allows to relate the streamwise velocity with the wall-normal coordinate, taking into account both streamwise pressure gradient and velocity gradient at the wall. They constitute the improved wall model proposed by (Duprat et al., 2011) in allowing to determine the wall shear stress, which is the required unknown quantity in practical LES. Henceforth, equation 4.11 and 4.12 will be referred in the text as new wall layer model (NWM) for the sake of convenience.

4.4 Validation study

To validate the implementation of the new wall layer model in the OpenFOAM framework, the channel flow with periodic hill is chosen as a test case. This configuration has been specifically defined as a test case for investigating issues of subgrid scale and wall modeling in the presence of massive separation from a smooth curved surface (Mellen et al., 2000). The shape of

the constrictions has been retained from (Almeida et al., 1993) and is available in the ERCOFTAC database (ERCOFTAC and database).

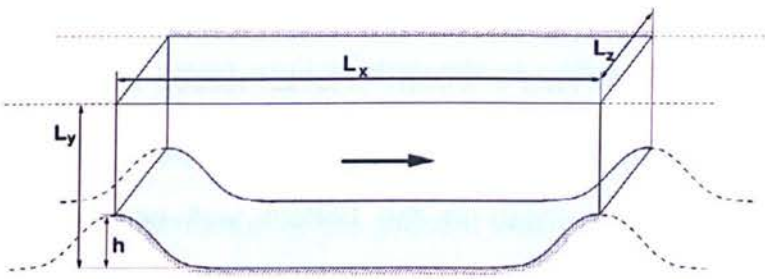

Figure 4.3. Channel with periodic hill geometry

The geometry of the periodic hill segment and its orientation is shown in Figure 4.3 and 4.4. The height of the hill h = 2.8 cm is considered for the simulation.

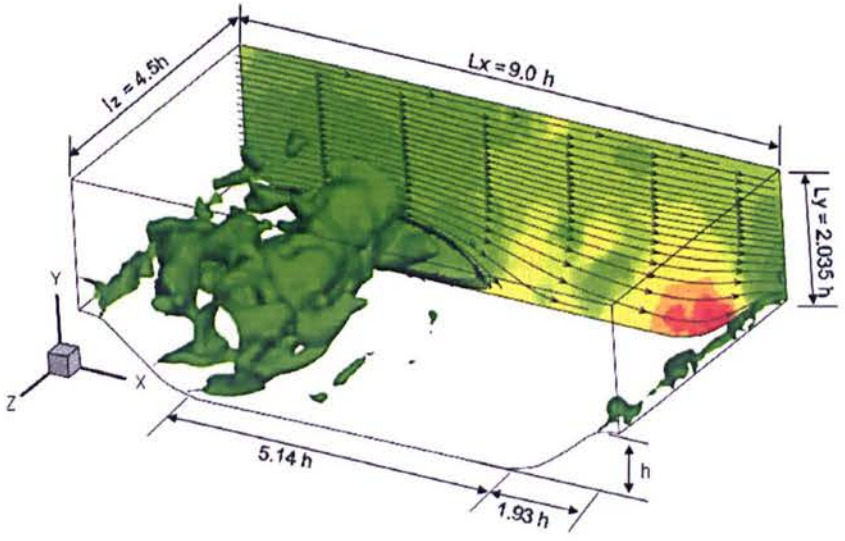

Figure 4.4. Periodic hill geometry with the instantaneous iso-pressure and time averaged streamline contours

The channel height is L_y = 3.035h and the streamwise period length is L_x = 9h. The computation domain is discretized into 0.38 million cells with N_x=120, N_y=33, N_z=96, where, $N_{(i=x,y,z)}$ is number of finite volume cells in coordinate

direction. For the same geometry, wall-resolved LES simulations were undertaken by (Temmerman et al., 2003, Frohlich et al., 2005, Breuer et al., 2007) with a mesh size of about 5 million nodes, Therefore the mesh used in the present simulation is almost less by a factor of 12 to the fully resolved case. The mesh distribution is kept uniform in streamwise and spanwise direction, however mesh in the bottom wall normal direction is slightly expanding away from the wall to have $y^+ \sim 30$. The mesh distribution in the vertical plane is shown in figure 4.5,

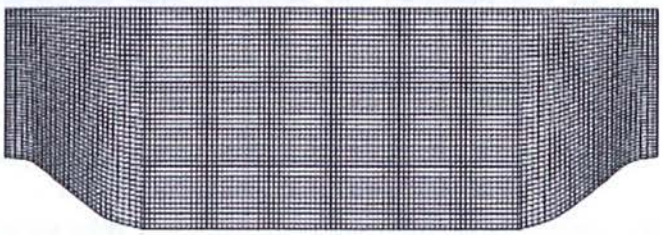

Figure 4.5. Mesh distribution in the vertical plane.

The Reynolds number based on the bulk velocity above the hill crest and the hill height is $Re_b \sim 10595$ corresponding to $Re_{Ly} = 21560$, based on the channel height and the bulk velocity $U_b = 1.724$ m/s. Bulk velocity is defined as ,

$$U_b = \frac{1}{2.035} \int_{h}^{3.035h} U(y)dy \tag{4.13}$$

Streamwise and spanwise periodicity boundary condition is chosen to removes the need for a specification of inflow conditions thus eliminating a number of potential sources for errors. The new improved layer wall model is applied at wall boundary. The required flow rate was imposed through a pressure forcing term which was kept constant in space and adjusted in time

so as to yield at each instant the desired flow rate. The pressure forcing term is added as a addition source term to the momentum and energy conservation equation. The computations of the time varying forcing term are previous discussed in section 2.10.1. Thus the bulk Reynolds number was held invariant while the pressure gradient varied depending upon the wall shear stress. The performance of the present wall layer model is compared with Spalding continuous law (SCL) simulation results (Spalding, 1961). The SCL model assumes zero streamwise pressure gradients and uses a Taylor series expansion to describe with a unique function, the entire turbulent boundary-layer i.e., viscous region, buffer layer and the logarithmic region. Spalding continuous law is given as,

$$y^+ = U^+ + \frac{1}{E}\left\{e^{-\kappa U^+} - \left[1 + (\kappa U^+) + \frac{(\kappa U^+)^2}{2} + \frac{(\kappa U^+)^3}{6}\right]\right\} \tag{4.14}$$

where, $\kappa = 0.42$ is the von Karman constant and $E = 9.1$ is constant characterizing the wall roughness for a smooth wall.

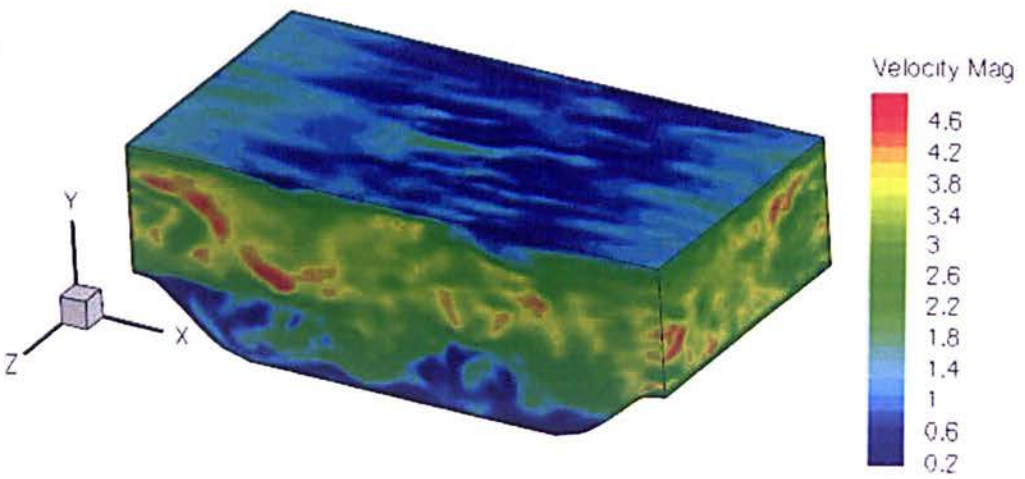

Figure 4.6 Instantaneous velocity contour plot

The magnitude of instantaneous velocity is contour plotted over computational boundaries as shown in figure 4.6, depicting regions of slow and fast moving fluid regions in the periodic hill channel domain. The mean velocity profiles represent quantities performance of the wall functions. The mean velocity profiles at different streamwise locations (x/h = 0.5, 1.0, 2.0, 3.0, 6.0 8.0) obtained after time averaging the flow quantities for nearly 250 flow through or flush time ($\sim L_x/U_x$) are shown in figure 4.7 (a)-(f). The simulation results using the NWL and SCL are compared with the fully resolved LES results of (Temmerman et al., 2003).

At x/h = 0.5

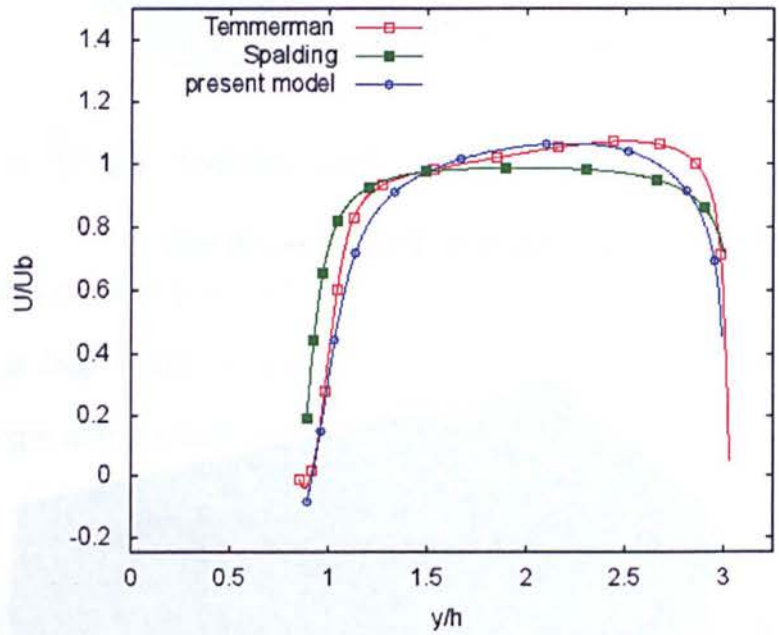

(a) At x/h = 1.0

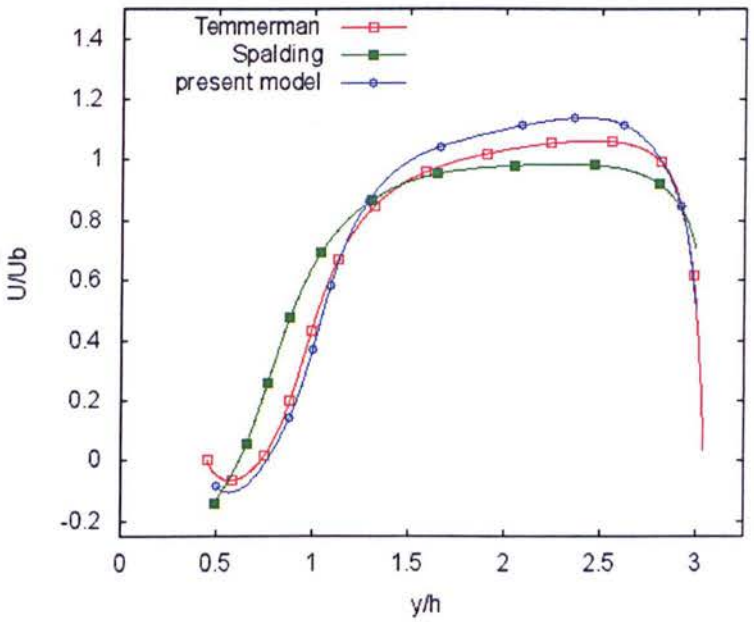

(b) At x/h = 2.0

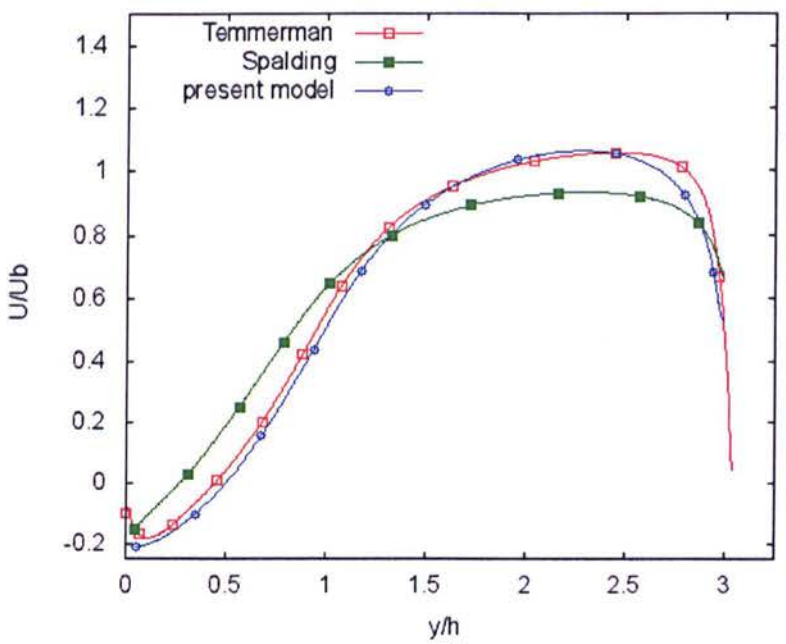

(c) At x/h = 3.0

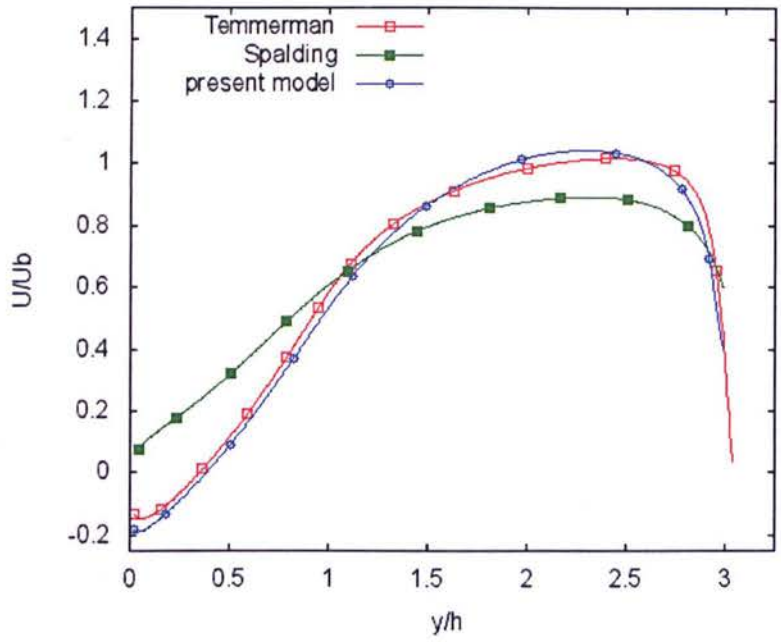

(d) At x/h = 6.0

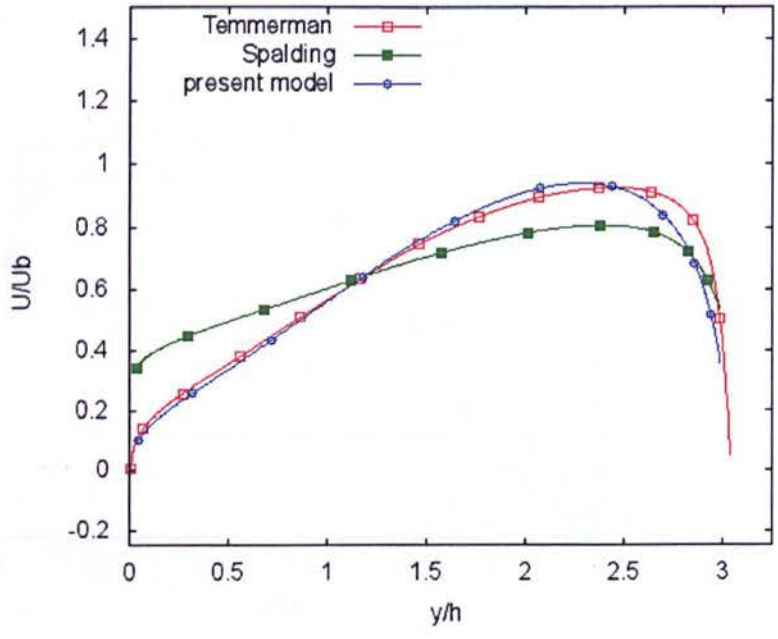

(e) At x/h = 8.0

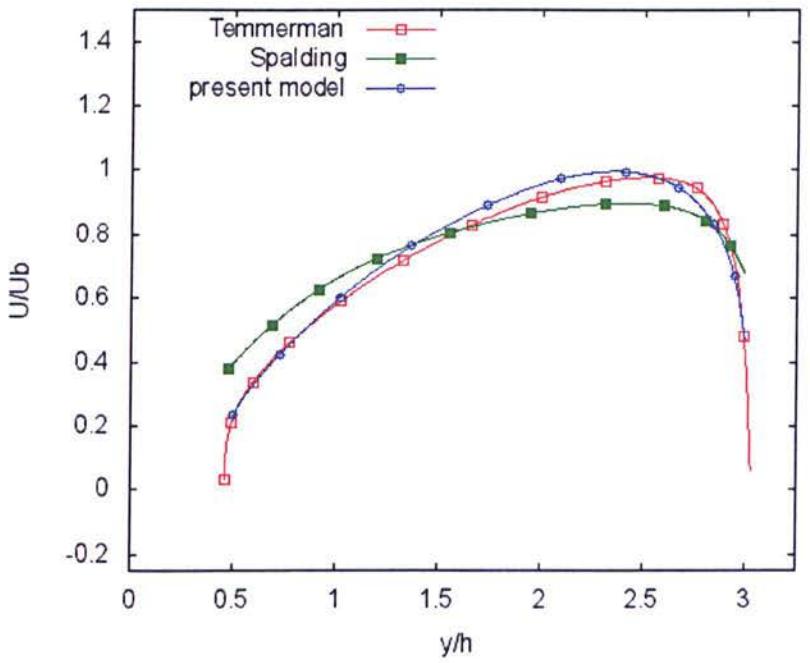

Figure 4.7. The mean velocity profiles at different (x/h) streamwise locations

In general, the SCL is giving poor predictions for both near the wall and in bulk of the flow. The new wall layer is showing good prediction in the near wall region and there are also some deficiencies in core of the flow. In general, the mean velocity predictions by NWL model are superior to SCL model at all the plotted streamwise location. The mean flow velocity streamline for three cases are shown below in figure 4.8. The predicted size of the recirculation zone is in the simulated cases are compared with the fully resolved results of (Breuer et al., 2007). The size of the separation zone is underestimated in figure 4.8 (b) using the SCL, whereas figure 4.8 (c), NWL is able to capture the recirculation zone size close to that obtained in fully resolved simulation by (Breuer et al., 2007).

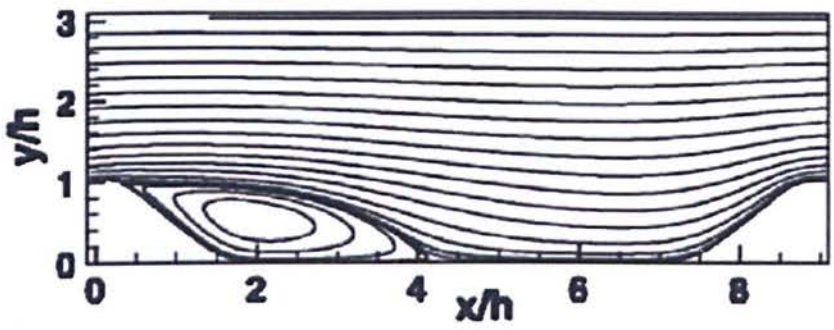

(a) Fully resolved case by (Breuer et al., 2007)

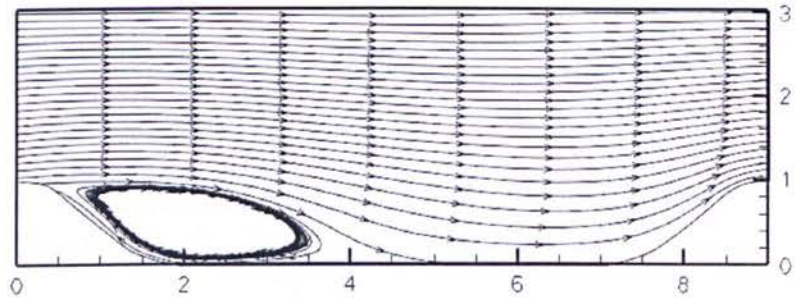

(b) Using Spalding continuous law.

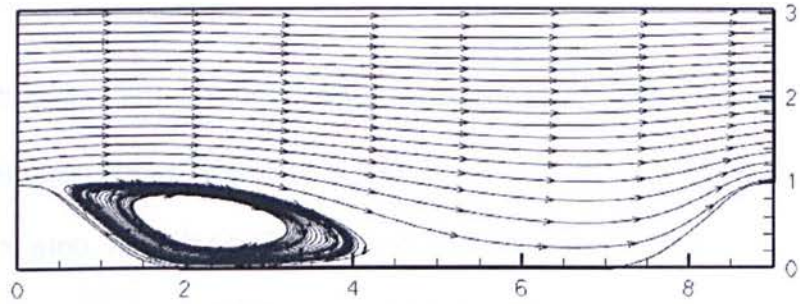

(c) Using the new wall layer model (NML)

Figure 4.8. Mean streamlines plots for chosen three different wall models.

The above discussed results of NWL clearly show that the streamwise pressure gradient inclusion in the wall model has improved the model predictions. The periodic hill channel flow case, which is considered a challenging case for wall functions functioning is well predicted and hence establish the model implementation.

4.5 Summary

The turbulent boundary layers have distinctive flow regions near the wall. Morkovin hypothesis suggest that the compressible turbulent boundary layer essentially follow incompressible turbulent boundary layer when the free stream Mach number is less than equal to 5. Therefore the flow statistic of compressible boundary can be readily compared to incompressible counterpart for the analysis and validation. In flows with adverse pressure, wall model based on the shear velocity scaling fail at the point of separation. Hence to make the wall model applicable to flows with/without pressure gradient, model should use combination velocity for scaling.

A new wall layer model proposed by (Duprat et al., 2011) using extended inner scaling, which takes into account both wall shear stress and streamwise pressure gradient. The new model is based on the simplified thin-boundary-layer equations and on a turbulent viscosity coefficient whose formulation is an extension of the ones originally proposed by (Balaras et al., 1996). The turbulent viscosity involves a damping function which is a function of the intensity of the streamwise pressure gradient. The results of flow in a periodic hill channel, clearly demonstrate the importance of taking into accounts both streamwise pressure gradient effects and shear stresses in the wall modeling. For flows with adverse pressure gradient, the present model is able to reproduce flow separation even when very coarse grids are considered. The model implementation in OpenFOAM is verified by simulating the flow in a periodic hill obstructed channel. The coarse grid LES results are able to predict the flow features obtained in a fully resolved LES results, hence establish the model implementation in OpenFOAM.

Chapter 5

FLAME-WALL INTERACTIONS

5.1 Introduction

Combustion is strongly influenced by the presence of walls which may cause flame fronts to quench and limits flame wrinkling. Also, the flame significantly affects the flow in the vicinity of the wall as well as on the heat flux to the wall. The flame approaching the cold wall (temperature of the wall is same as the ambient conditions, which is typical scenario for combustion processes in enclosures), losses heat through diffusion and within some distance to the wall it retreats and vanishes as its consumption rate of the burned fuel diminish slowly to zero. The flame that retreats is a weak premixed flame, though it propagates away from the region of highest fuel concentration. The reaction zone appears always to be relocated to the regions that maximize reaction rate. The activation energy plays a profound role on premixed flame quenching. Higher the activation energy, smaller is the required enthalpy loss from the flame zone for its extinction (Wichman and Bruneaux, 1995).

Most of the early experiments in flame-wall studies were in laminar flows performing quenching studies, involving tubes, spherical bomb and narrow channels with primary interest of determining flame quenching distance i.e., the distance from the wall at which the flame stops propagation and eventually gets quenched. In laminar flame wall interaction, it has been

experimentally verified that apart from the heat loss to the wall, the diffusion of H, O and OH radicals in the flame front plays a vital role in determining whether or not the flame will be quenched by a given wall geometry.

The turbulent flame-wall interaction becomes much more complex due to increase of diffusion and mixing at various length scales. Turbulence is also influenced by the presence of both flame and the wall. Viscosity is greatly increased in the burned gases, which tends to inhibit turbulence. Excessive turbulence can itself quench the flame. A laminar flames entering a region of intense turbulence without mean flow was studied by (Chomiak and Jarosiński, 1982) measuring instantaneous temperature, global and local chemiluminescence using fast schlieren photography. It was observed that the premixed flame is quenched by turbulence for a critical value of Karlovitz-Kovasznay criterion $K=(\Delta u'/l_t)(\delta_l/S_l)$ lying between 7 and 20. The coincidence of laminar and turbulent flame quenching data indicates that the extinction of flame by the flow has a universal character and is caused by excessive stretch of the local combustion region.

Flame-wall interactions are simplified to the following configurations namely, Head on quenching, Side wall quenching and Tube quenching (Poinsot and Veynante, 2005). In head on quenching the flame propagates in perpendicular direction to the impinging surface as shown in Figure 5.1.a. The entire flame front is affected by the confining wall. The wall heat transfer is maximum in case of head-on quenching. In side wall quenching, flame propagates in parallel direction to the bounding wall as shown in figure 5.1.b. Only edge of the flame close to the wall is affected by the confining wall. The

heat transfer to the wall is less in magnitude when compared to the head on quenching case.

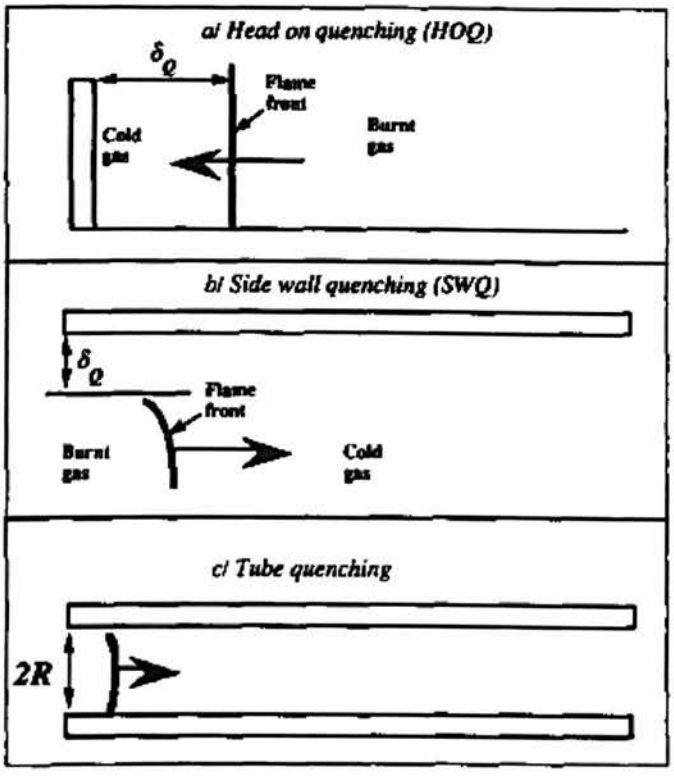

Figure 5.1. Configuration for flame-wall interactions (Poinsot and Veynante, 2005)

Tube quenching is an extended scenario of side wall quenching, the flame edge close to the tube wall is affected hence wall heat transfer to the wall is along the circumference of the flame. Based on the thermal theory of flame quenching, the critical Peclet numbers for flame quenching in each of the above scenarios are different and are in same order of magnitude as found by many researchers for simple geometries. Typical Peclet number (Pe) values are as follows, a) Head on quench, Pe ~ 3, b) Side wall quench, Pe ~ 7, c) Tube quench, Pe ~ 50. Peclet number (Pe), is a nondimensional number defined as the ratio of rate of advection of a flow quantity to the rate of diffusion of the same quantity.

In remain parts of this chapter, first presents the literature review of some of the recent published work in section 5.1.1 and 5.1.2 to bring out the major factor influencing flame-wall interactions in laminar flows and in turbulent flow respectively. In section 5.2 and section 5.3, the modeling required for the CFM and the modification proposed for the standard governing equation are shown. The proposed flame-wall interactions have two model constants. These two model constants are evaluated in a posterior test - simulating turbulent 'V'-flame anchored in a channel in section 5.4. The final section 5.5 summarizes the discussions carried out in this chapter.

5.1.1 Laminar Flame-Wall interaction

Laminar flame-wall studied is often characterized by two parameters, i.e. the quenching distance and the wall heat flux. The wall distance 'y' is normalize by a characteristic flame thickness, $d = k/\rho C_p S_l$, where k is thermal conductivity of the gas and expressed as the local Peclet number,

$$Pe = \frac{y}{d} \tag{5.1}$$

The instantaneous wall heat flux ϕ is normalized by the laminar 'flame power' (Flame power is amount of heat released by flame per unit time per unit surface area).

$$\phi = \frac{\varphi}{(\rho Y_0^F S_l \Delta H)} \quad \text{and} \quad \varphi = -k \left.\frac{\partial T}{\partial y}\right|_w \text{ is wall heat flux.} \tag{5.2}$$

The wall temperature is an important factor in flame-wall interaction. The effects of wall temperature and surface property on flame quenching are investigated experimentally by (Kim et al., 2006) in an apparatus that has a

high surface-to-volume ratio as in a micro scale combustor. In most micro combustors, the effects of flow are absent during quenching because the flow is laminar and no severe stretch is present. In such a circumstance, quenching is mainly caused either by heat loss or by removal of active radicals at the combustor wall. A two-dimensional slit burner discharging a combustible mixture between two parallel plates was used for the quenching experiments. The distance between the two walls at which quenching occurs was measured under different surface conditions. The results were analyzed to estimate the relative significance of heat loss to the wall and the removal of radicals at the surface. The measured quenching distance indicated that there exist three distinct regimes in the quenching behaviour. For low surface temperature of the plates ranging between 373 K and 623 K, the quenching is mainly determined by the heat loss to the plate and is independent of surface properties. When surface temperature of the plate increases beyond 673 K, the flame quenching becomes dependent on the heterogeneous reaction of radicals at the surface and quenching distance increases with surface temperature. In this regime, the surface property affects the quenching distance. As the temperature of plates increases beyond 873 K, the homogeneous chemical reactions overcome the effect of radical removal by the surface and the flame becomes resistant to quenching. Therefore, it was conclude that the surface reaction must be considered for accurate prediction of quenching and stabilization of flame, particularly when the combustor has a high surface-to-volume ratio. Similarly wall temperature effect was studied by (Boust et al., 2009) in laminar head-on quenching between temperatures 300-500 K and inferred that the wall heat flux increases and quenching distance

decreases with increase in the wall temperature, establishing that wall temperature is one of key factor influencing near wall flame quenching.

The unsteady heat transfer during premixed laminar flame quenching was measured by (Ezekoye et al., 1992) in a constant volume chamber over a range of wall temperature from 298 K and 423 K and a range of equivalence ratio 0.8 -1.2 for both methane and propane. The fraction of the heat release rate attributed to heat transfer was found to be independent of the equivalence ratio but dependent on the wall temperature.

The influence of flow pressure, velocity and turbulence on quenching distance was examined experimentally by (Ballal and Lefebvre, 1977) using combustible mixtures of methane and propane. In some of the trials the nitrogen in the air was partially or totally replaced with either by oxygen or argon to study the relative importance of thermal and diffusional mechanism in the quenching of hydrocarbon flames. The results in general confirmed that importance of thermal diffusion processes, even at high flow velocities.

The coupling of thermal and chemical processes is found to be significant in flame quenching .The relative influence of heat loss and radical recombination reactions in flame quenching was carried out by (Sloane and Ratcliffe, 1982) using molecular beam mass spectrometer sampling. The chemistry effect of a flat lean CH_4-O_2-Ar flame at 4.0 KPa which is cooled by gold and a platinum surface whose temperature is held at 373 K was examined. The gold surface is chemically inert and its effects on the flame was limited to cooling of the flame, whereas the platinum surface promotes recombination of H, O and OH radicals which collide with the surface. It was concluded from the results that cooling of the flame gases has a far greater

effect than catalytic recombination activity of the surface on flame quenching. The cooling effect extends out to nearly 1.0 cm from the surface in the experiments, whereas the effects of recombination on the surface are restricted to 0.1 cm from the surface.

Experimental measurements of quenching distance in laminar head-on and side-wall quenching of premixed methane-air were carried out by (Bellenoue et al., 2003). The quenching Peclet number was found to be in similar magnitude as numerically predicted. The influence of the wall material was also studied in terms of the wall heat flux estimated from the theoretical formula based on measured quenching distances. The peak heat flux to the polished steel surface is found to be 0.46 & 0.26 MW/m^2 for head-on and side wall quenching respectively and for ceramic surface values were 0.8 & 0.39 MW/m^2 for head-on and side wall quenching.

In terms of modeling quenching distance, a thermal formulation of single wall flame quenching was proposed by (Boust et al., 2007) for simple laminar model with stretch effects neglected. This model describes the relation between quenching distance and mixture composition. It allows evaluating quenching distance using the wall heat flux and mixture properties, a significant advantage of this formula is the absence of any empirical coefficient. Experiments have been done for both head-on and sidewall configurations in quiescent methane-air mixture in a constant volume chamber (70 x 75 x 120 mm^3) to examine the model predictions. Quenching distance is determined through direct visualization, whereas wall heat flux is processed from the time evolution of wall surface temperature. Flame stretch tends to be zero in head-on configuration, whereas it takes finite values in

sidewall configuration due to flame curvature. The quenching distance computed using the model equation is found to be within 25% variation of the experimental data for the laminar flame-wall interaction.

A two-dimensional stationary model has been used to study the sidewall quenching of laminar propane/air flames in a boundary-layer flow (Andrae et al., 2002). The flame is parallel to the wall sweeping the laminar boundary-layer while propagating and interacting with the wall. The main purpose has been to examine the extent to which the flame can propagate toward the cooled wall for lean flames compared to stoichiometric flames. A detailed kinetic model is used to examine the oxidation of both the fuel and the intermediate hydrocarbons (IHCs). For stoichiometric and near stoichiometric mixtures, the thermal coupling between the flame and the wall is small but significant. However, for very lean flames, the thermal coupling between the flame and the wall is found to be very significant. Stoichiometric and near-stoichiometric flames are very strong, and the thermal boundary layer is relatively thin. Therefore, the flame can consume the unburned fuel at the wall in a short residence time. The study has examined only steady laminar flames in a boundary-layer flow.

From the above brief discussion it can be summarised that the major factors affecting the Flame-Wall interaction can be listed as,

1) Heat transfer to wall/ heat loss
2) Chemical reaction / radical absorption
3) Thermal/Mass diffusion (Le)
4) Flame stretch
5) Turbulence

6) Wall temperature

7) Fuel properties / concentration

8) pressure

Ideally the flame-wall interaction modeling should include the effect of these factors at least in a minimal way.

5.1.2 Turbulent Flame-Wall interactions

In turbulent combustion, the transient boundary layer has a different structure, and the effect of the scale of the turbulence across the turbulent boundary layer on the wall effects is still unclear. Very few experiments have been conducted to study Flame-Wall interactions in turbulent flows due to the difficulties associated with the small length and time scales involved. The temperature decrease from burnt gas to the wall temperature occurs in the near-wall layer which is less than 1 mm thick, leading to very large temperature gradients. The only measurable quantity is the transient wall heat fluxes. Flames are dominated by highly transient effects when approaching walls. They do not touch the walls. Instead, they are quenched a few micrometers from the wall as the low temperature of most walls inhibits chemical reactions (Poinsot and Veynante, 2005).

DNS studies to understand the interactions of turbulent flame with wall are very promising in bring out the inter-dependence of flame and turbulence near wall. Due to associated high computational efforts in detailed modeling, so far the DNS studies were indeed performed considering very restrictive assumptions, like constant density, low heat release, two dimensional, single step chemistry, single mode of turbulence (Re_t ~ 180). Hence information

available for modeling in RANS and LES are also limited. DNS results have shown that flame essentially gets quenched in the laminar viscous region near the wall. The quenching distance is smaller and the maximum heat flux to the wall is higher in turbulent flames compared to that of laminar flames. The coherent flow structure in near wall region play a dynamic role in pushing the flame elements closer to the wall and hence causing higher wall heat fluxes. (Poinsot et al., 1993, Bruneaux et al., 1997).

The interaction between laminar and turbulent premixed flame and wall is studied by (Poinsot et al., 1993) using a two dimensional DNS with simple chemistry. The effect of wall distance on the local and global flame structure were investigated. Based on the simulation results 'law of the wall' model is derived to describe the interaction between a turbulent flame and a wall. In turbulent case, the configuration studied corresponds to the shear free boundary layer in which the turbulence with no mean shear interactions with the wall. The initial turbulence field was chosen to produce small scale turbulence near the wall and to impose zero velocity fluctuations at the wall. Based on laminar flame wall interaction, two zones are identified in near-wall region, namely quenching and influence zone.

The quenching zone stretch from the wall (y = 0) to a distance corresponding to a local Peclet number of about 3.4. In this zone no reaction takes place. The influence zone goes from the wall y = 0 to a distance δ_t corresponding to a Peclet number of about 8 and flame entering the influence region will start sensing the wall and will eventually get quenched. The heat flux to the wall appears to be controlled mainly by heat diffusion. The overall turbulent flame behaviour near the wall was summed by authors as, when the

flame first reaches the wall, it has a normal incidence and behaves like a head on quenching and flamelets stops at a distance from the wall given by P ~ 3.4. Then the flame flattens and the part of the flame close to the wall quenches. This creates a quench zone, where heat diffusion takes place without combustion leading to development of cold zone. On both sides of the quench zone, pieces of the flame which have not been quenched during the first interaction then move away from the cold zone, parallel to the wall. These flamelets stabilize when they are located at a distance roughly equal to the one given by Peclet number of 7, similar to side wall quenching (Poinsot et al., 1993). The quenching zone thickness and the influence zone thickness have similar values for turbulent and laminar premixed flames. The quenching zone is located inside the viscous layer. One of the important conclusions drawn for this study was that the Flamelets travelling from the free stream towards the wall first encounter laminar flow in the viscous region and only later are quenched. The results are used in the modeling of flame wall interaction – 'FIST' model (Flame Interaction with Surface and Turbulence).

Turbulence is inherently three dimensional (3-D) in nature and hence 3-D simulations are required to capture the true dynamics effects of turbulence on flame. (Bruneaux et al., 1996) performed 3-D DNS of premixed flame interacting with channel walls with constant density (low heat release) and variable viscosity modeling(Bruneaux et al., 1996). The computation is first initialized with random fluctuations imposed on a mean Poiseuille profile. The turbulence develops from these fluctuations and reaches a statistically stationary state, at this instant the reaction solver is started and a slab of burned gases is introduced near the centre of the channel, so that two back to

back 1D laminar flame propagate towards the walls. Combustion is represented by a simple irreversible reaction with a large activation temperature. It was found that the quenching distance decreases and the maximum heat fluxes increase relative to laminar flame values, scaling with the turbulent strain rate. The normal strain is generated by horseshoe vortices which push flame elements towards the wall and convects fresh gases away from the wall, forming finger like structure. These DNS results were further analyzed in terms of flame surface density parameters and modeling changes to CFM-RANS were proposed (Bruneaux et al., 1997) . The major outcome of this work was that during the flame wall interaction, high flame surface density gradients near the wall are responsible for the predominance of the transport terms in the conservation equation of FSD. Enthalpy loss though the wall affects flamelets speed, flamelet annihilation and flame propagation. Decrease of turbulence scales near the wall also affects turbulence diffusion and flame strain.

The changes induced in the mean turbulent boundary layer by the presence of flame was studied by (Alshaalan and Rutland, 1998) in a Couette channel flow using 3-D DNS with single step chemistry. A 'V'-flame held in place by a flame holder was simulated such that one end of section of the flame was interacting with the wall (nonadiabatic) and the other section was unaltered by the wall (adiabatic). It was found that the heat release in the flame alters both the local flow and imposes a mean streamwise pressure gradient, the mean velocity is accelerated. The increase in the wall shear stress was more rapid than the increase in the velocity. The reduction in turbulent length scales induced by flame is more in adiabatic flame compare

to nonadiabatic flame since in nonadiabatic case, the flame loses energy near wall and the movement of the flame brush is restricted by the wall. A similar configuration was experimentally studied by (Tayebi et al., 2007). The interaction between a turbulent premixed flame and a laminar boundary layer were examined by using a stationary 'V'-shaped flame, stabilized on a rod, expanding in a lean premixed methane-air flow and interacting with an adiabatic wall laterally. The Laser Doppler Anemometry (LDA) was used to quantify the velocity field. Results showed that the flame is globally deflected by the wall with a drastic reduction in the flame brush thickness, smoothing the turbulent shape of the flame front in the interacting zone. The flame front length decreases as consequence of damping of the flame wrinkles and extinction of the flame front near the wall. Results also suggest that the turbulent flame doesn't disturb the velocity gradient in the laminar boundary layer region.

The presence of turbulence in a flammable gas mixture wrinkles the flame front increasing the flame surface area and enhancing the burning rate. Experimental data was analyzed for the turbulent velocity field generated during flame-obstacle interaction in explosion by (Hargrave, G. H et al, 2002). The interaction between the gas movement and the obstacle creates turbulence by vortex shedding and local wake recirculation whereby the flame can be wrapped in on itself, increasing the surface area available for combustion. Particle Image Velocity (PIV) was used to characterize the turbulent flow in the wake of the obstacles placed in the path of propagating flame. The experimental setup was 150mm x 150mm and 500 mm long with one end closed. Experiments were carried out with rectangle, cylinder and

square obstacle shapes with 50% blockage ratio. Results showed that the flame acceleration and overpressure were higher for the rectangular obstacle due to the high wrinkling caused by the generation of many small-scale vortices shedding from the sharp edges of the obstacle.

(Gruber et al., 2010) studied turbulent flame–wall interaction in a 3-D channel configuration using DNS and detailed chemical kinetics for hydrogen-air mixture. Simulations results are used to investigate the effects of the wall turbulent boundary layer (i) on the structure of a hydrogen–air premixed flame, (ii) on its near-wall propagation characteristics and (iii) on the spatial and temporal patterns of the convective wall heat flux. Results show that the local flame thickness and propagation speed vary between the core flow and the boundary layer, resulting in a regime change from flamelet near the channel centreline to a thickened flame at the wall. This finding has strong implications for the modeling of turbulent combustion using RANS or LES techniques. Moreover, the DNS results suggest that the near-wall coherent turbulent structures play an important role on the convective wall heat transfer by pushing the hot reactive zone towards the cold solid surface. At the isothermal wall temperature 750K, zero activation energy exothermic radical recombination reactions become important, and are responsible for approximately 70% of the overall heat release rate at the wall. Spectral analysis of the convective wall heat flux provides an unambiguous picture of its spatial and temporal patterns, previously unobserved, that is directly related to the spatial and temporal characteristic scaling of the coherent near-wall turbulent structures.

5.2 Modeling strategies

Within the purview of the CFM/FSD combustion models, the model parameters requiring flame-wall interaction modifications are laminar flame speed (S_l) and the flame surface density (Σ). (Poinsot et al., 1993) proposed a law-of-the-wall model named 'Flame Interaction with Surface and Turbulence' (FIST) in the context of the RANS. Based on two dimensional DNS study, the near wall region is categorized into two: close to the wall as 'inhibition layer' and remaining as fully turbulent region. The 'inhibition layer' is further categorized as 'quench zone' and 'influence zone'. A new source term accounting for flame quenching is proposed in the conservation equation for flame surface density apart from the flame source and consumption terms. These source terms are either set to 'zero' or modelled based on the location of the computation cells in the respective zones in the near wall region. The complete details about the FIST model can be found in the (Poinsot et al., 1993). The above model lacks in taking account of the factor influencing the flame quenching for instance the wall temperature and also the limits proposed for the respective zones categorization based on Peclet no. (Pe) are known to be not universal. A similar zonal modeling named as '0D flame-wall interaction' was used by (Rivas et al., 2011) for simulating internal combustion engine process. Again this model was in context of CFM-RANS and proposes two zones near the wall. The near wall region is quench zone and in this region extinction function is applied to flame surface density to quench the flame completely towards the wall. The extent of wall quench zone is determined based on half of near wall integral length scale. Setting the FDS to zero in the cells close to a wall, there is no physical ground upon

which such ad-hoc modeling can be justified. A proper approach to incorporate wall model in turbulent combustion models is to modify models near walls using physical arguments.

A more practical approach was used by (Bruneaux et al., 1997) in CFM-RANS to identify the near wall region for flames. The wall region was identified as the region in which the enthalpy is lost by the flame, due to wall heat transfer. Three dimensional constant density DNS of back-to-back flame in a channel flow was carried out to extract modeling implications for flame surface density balance equation. Back-to-back flame is referred to the two flame fronts generated by introduction of slab of burnt gas at the centreline of the turbulent channel flow to initiate reaction. Since the flow is constant density and is not influenced by flame, no momentum equation was solved. The wall has constant temperature and lead to flamelet quenching for sufficiently small wall flame distances. Single step chemical reaction was used to represent the combustion process. It was identified that, during the flame wall interaction, high flame surface density gradients near the wall are responsible for the predominance of the transport terms. Enthalpy loss though the wall affects flamelets speed, flamelet annihilation and flame propagation. Decrease of turbulence scales near the wall affects turbulence diffusion and flame strain. Based on the DNS results, modeling changes to CFM-RANS were proposed. In the present study the model proposed by (Bruneaux et al., 1997) are been adopted in LES context and explained in detail in the following section.

5.3 Modeling of CFM-LES

The flame-wall interactions are accounted by extending the closures proposed by (Bruneaux et al., 1997) for the CFM–RANS model in the LES context. The enthalpy loss factor proposed in the constant density flow field is revised to make it applicable for reactive compressible flows.

5.3.1 Enthalpy loss factor

There is no unified approach in capturing the enthalpy loss from the flame zone to the wall. Some previous studies are based on excess enthalpy factor and flame temperature polynomial fitting. The original parameter proposed by (Bruneaux et al., 1997) is applicable to systems at isobaric conditions with no appreciable pressure rise.

$$L_H = \frac{H_F^o - H}{H_F^o - H_P^o} \tag{5.3}$$

Where, H is gas enthalpy, H_F^o is the fuel enthalpy at the temperature of the fresh gases, H_P^o is the enthalpy of the product in the same state. The equation 5.3 can be simplified for simple chemistry under lean combustion, i.e. fuel is the limiting factor to (Williams, 1985, Wichman and Bruneaux, 1995),

$$L_H = 1-(Y+\theta) \tag{5.4}$$

where $\theta = \frac{T - T^o}{T_{ad} - T^o}$ is reduced temperature and $Y = \frac{Y_F}{Y_F^o}$ is reduced fuel mass fraction. In an adiabatic premixed flame with unity Lewis number, $L_H = 0$ everywhere and when the flame is non-adiabatic near wall, $L_H < 1$.

(Angelberger et al., 1997) extended the enthalpy loss factor used by (Bruneaux et al., 1997) to non-isobaric conditions and applied it to internal combustion engine computation.

$$L_H = \frac{H_u^{t_0} + \int_{t_0}^{t} (dp/\rho) - H^t}{\Delta H} \tag{5.5}$$

Where, Hu is the unburnt gas enthalpy, H^t the gas enthalpy at a given instance, dp is change in pressure, ρ is density of gas and ΔH is the heat of reaction per unit mass of fuel. In the present study, we used the enthalpy loss factor definition (equation. 5.5) proposed by (Angelberger et al., 1997), with transport equation for the unburned reactant enthalpy. The additional transport equation 2.21 is solved primarily for the unburnt reactants temperature in order to evaluate unstrained laminar flame speed using the correlation in equation 3.4. Thus, the influence of pressure variation on enthalpy loss factor near wall region is accounted.

5.3.2 Modeling of Flame-Wall interaction in FSD

Enthalpy loss through the wall affects the flamelet speed, flamelet annihilation and flame propagation. The rate at which the laminar flamelet speed is reduced due to enthalpy loss is modelled in terms of a quenching factor Q_m

$$\frac{S_{lm}}{S_l} = Q_m = e^{-\gamma_q \beta L_H} \tag{5.6}$$

where, γ_q is model constant $\beta = \alpha \frac{T_{av}}{T_{ad}}$ is reduced activation energy, $\alpha = \frac{T_{ad} - T_o}{T_{ad}}$ is heat release factor. The suffix 'm' refers to the modelled quantities. Near the wall both laminar flame speed and flame displacement

speed decrease. The rate of decrease is more predominant in the latter speed and becomes negative when flame retreats from the wall, dynamically approaching the region of lower enthalpy loss, while laminar flame speed always stays positive (Bruneaux et al., 1997). The displacement speed is modelled as

$$S_{dm} = S_l\,(1-(1-Q_m)/\gamma_d) \tag{5.7}$$

where, γ_d is a model constant. The model constants γ_q and γ_d are fine tuned in the present simulation. The turbulent diffusion accounts for the transport of flame surface density by turbulent convection and is modelled using turbulent viscosity. The decrease in the turbulent scales near the wall affects turbulent diffusion and flame strain rate. The van Driest mixing length is used for reduction in turbulent length scales towards wall and in the LES context, this can be regarded as modifications to the filter size.

$$\hat{\Delta}_m = \min(\hat{\Delta}, (\kappa/C_\Delta))y(1-e^{-y^+/A^+}) \tag{5.8}$$

where, κ is the von Karman constant, C_Δ= 0.158, A^+=26.0 are model constants, y^+ is nondimensional wall distance.

After modification for wall effects in CFM-LES, the progress variable equation 3.35 and filtered flame surface density transport equation 3.36 are given as (with suffix 'm' added to the modified quantities),

$$\frac{\partial}{\partial t}(\bar{\rho}\tilde{c})+\nabla.(\bar{\rho}\tilde{u}\tilde{c}) = \nabla.(\sigma_c\mu_{effm}\nabla\tilde{c})+\rho_u S_l Q_m \overline{\Sigma}_{\tilde{c}} \tag{5.9}$$

$$\frac{\partial \overline{\Sigma}_{\tilde{c}}}{\partial t}+\nabla.(\tilde{u}\overline{\Sigma}_{\tilde{c}})-\nabla.(\sigma_c\mu_{effm}\nabla\overline{\Sigma}_{\tilde{c}}) = (\nabla.\tilde{u}-NN:\nabla\tilde{u})\overline{\Sigma}_{\tilde{c}}+\Gamma\left(\frac{\hat{u}'}{S_l},\frac{\hat{\Delta}_m}{\delta_l}\right)\frac{\hat{u}'}{\hat{\Delta}_m}\overline{\Sigma}_{\tilde{c}}/\sigma_c$$

$$+S_{dm}(\nabla.N)\overline{\Sigma}_{\tilde{c}}+\beta S_l Q_m\frac{c^*-\overline{c}}{\overline{c}(1-\overline{c})}(\overline{\Sigma}_{\tilde{c}}-\overline{\Sigma}_{\tilde{c}}^{lam})\overline{\Sigma}_{\tilde{c}}-\nabla.(S_{dm}N\overline{\Sigma}_{\tilde{c}}) \tag{5.10}$$

The two model constants γ_q and γ_d in equation 5.6 and 5.7 respectively were proposed by (Bruneaux et al., 1997) as 2 and 0.3 based on constant density DNS in a non-stationery back-to-back flame in channel configuration. These values were found to be deferring in actual compressible flow (Angelberger et al., 1997) also based on the present authors previous study (MadhavRao et al., 2011, Vendra et al., 2013). Hence a detailed posteriori test has been carried out to ascertain the model constants which will be discussed in the following section.

5.4 Posteriori test

Three dimensional fully compressible DNS studies of the turbulent flame-wall interactions are very few. Two such studies were reported by (Alshaalan and Rutland, 1998) and (Gruber et al., 2010). Both author groups have simulated the 'V'-flame anchored in a turbulent couette and channel flow respectively. The flame displacement speed and wall heat flux plots in the DNS results of (Gruber et al., 2010) are primary modeling parameters in CFM. Hence the results of (Gruber et al., 2010) are more appropriate for model validation study of CFM-LES. The flame-wall interaction model constants required in the present study were hence fine-tuned by comparing the LES predictions with this DNS data.

The DNS case in (Gruber et al., 2010) was a 'V' flame anchored in a three dimensional turbulent channel flow (7H x 2H x 3H ; H=0.0029 m) at Re_t = 180 (centreline Reynolds number ~ 3200) with hydrogen-Air at equivalence ratio 1.5 and no-slip, isothermal channel walls were at 750 K temperature.

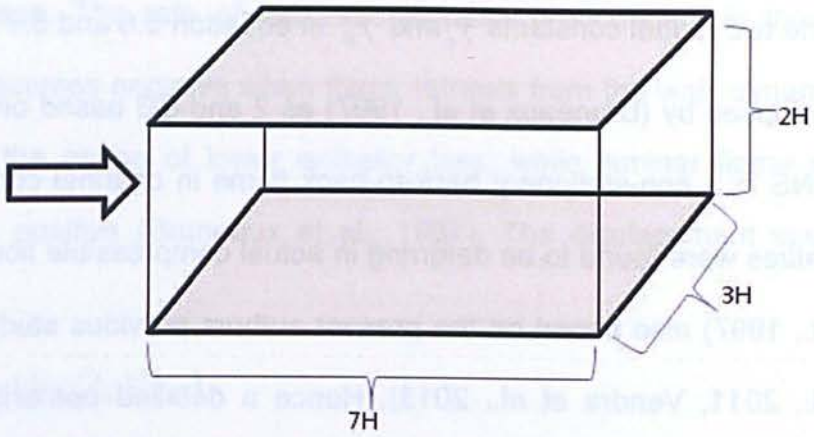

Figure 5.2. Channel layout (x- streamwise, y- wall normal, z –spanwise, H = 0.0029 m)

The reacting case was setup by superimposing the laminar 'V' flame on to the turbulent flow with boundary condition changed to non-reflecting inflow/outflow in streamwise direction. The complete 9 species, 19 reactions hydrogen–air chemical kinetics mechanism by (Li et al., 2004), was used to simulated the 'V'-flame.

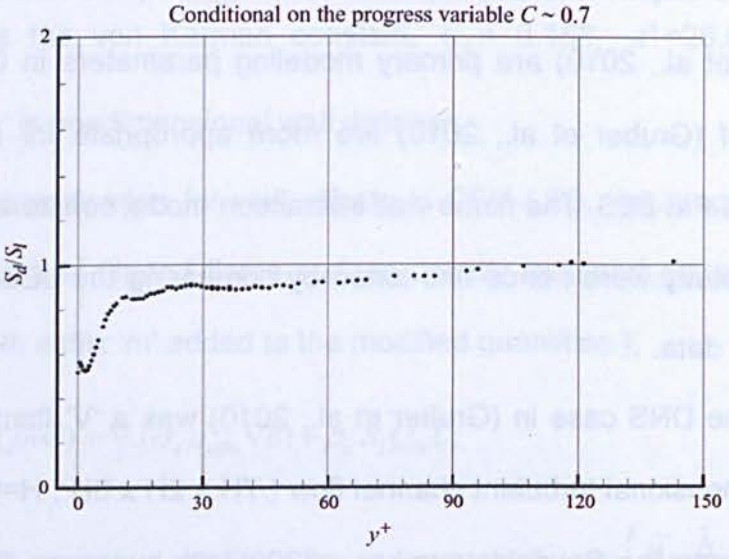

Figure 5.3. Flame displacement speed normalized by laminar flame speed DNS results (Gruber et al., 2010)

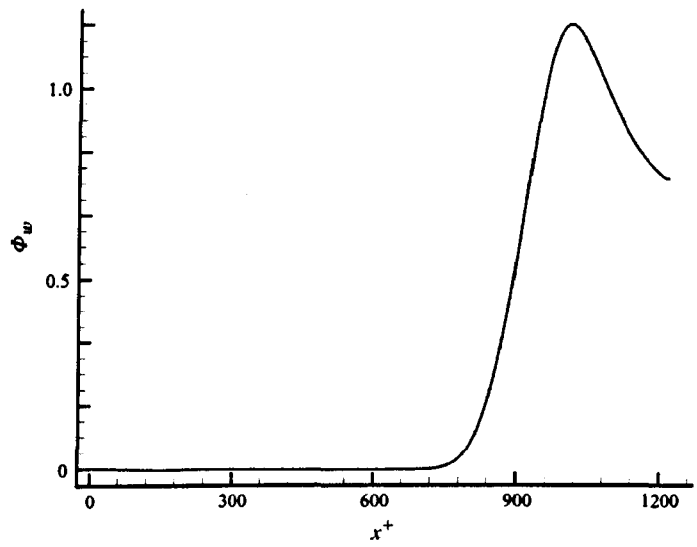

Figure 5.4. Wall heat flux normalized by laminar wall heat flux, DNS results (Gruber et al., 2010)

The flame displacement speed and wall heat flux plots in the DNS results of (Gruber et al., 2010) are shown in figure 5.3 and 5.4 respectively. The data in these plots are digitized to later compare them, to fine tune the LES results in posteriori test.

5.4.1 Numerical setup

The non-reacting turbulent channel flow field was obtained by using periodic boundary condition for both streamwise and spanwise directions shown in figure 5.5. The results were compared with the DNS results of (Kim et al., 1987) as detailed in section 2.10. The channel domain is discretised into 260 x 200 x 160 ~ 8 million computational cells and flow near the wall is resolved using very non-uniform mesh distribution in the wall normal direction. The computational grid is stretched in the y-direction by a hyperbolic tangent function given in equation 2.45. The parameter $\gamma = 2.85$ controls the grid non-

uniformity. The near wall region is fully resolved with first mesh point is within y^+ = 0.5 and 15 points within y^+ < 10. The discretisation scheme for the time derivatives is second order accurate, implicit backward scheme. The convective terms are discretized using second order accurate Gaussian-Gamma bounded scheme. The diffusion terms are discretized using Gaussian linear corrected scheme which is central differencing, with explicit non-orthogonal correction. Finally the gradient terms are solved using Gaussian linear scheme which is also central differencing.

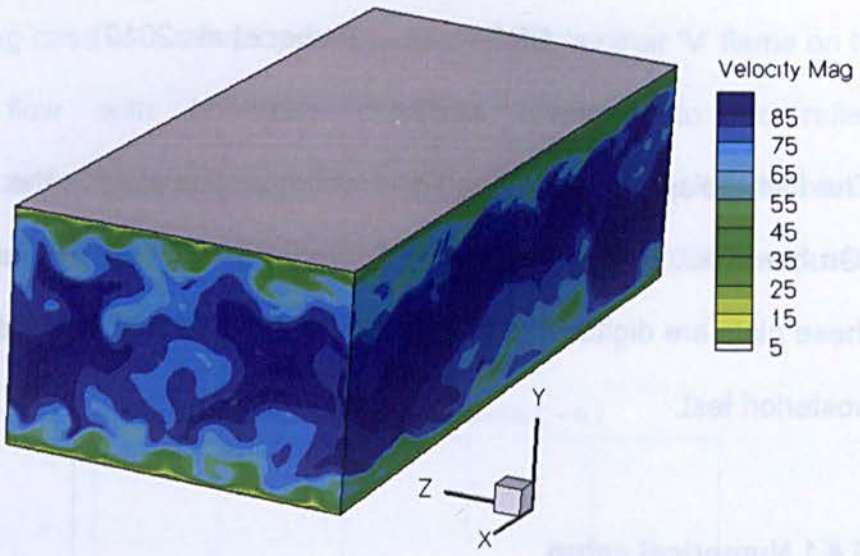

Figure 5.5. Fully developed turbulent channel flow field

The LES results are generated by considering exactly the same flow conditions as that of the DNS by (Gruber et al., 2010) mention in section 5.4, using CFM-LES combustion model with wall interactions . The reacting case was setup by superimposing the laminar 'V' flame on to the turbulent flow with boundary condition changed to inflow/outflow in streamwise direction. The simulations were further continued till sufficient number of flow

statistics were collected for analysis. The timevaryingmapped inlet boundary is applied at the inflow for velocity and temperature field. The zero-gradient condition is applied for the velocity and temperature fields at the outlet. The pressure boundary condition at the inflow is zero-gradient and non-reflecting waveTransmissive condition at outlet. Details about the above mentioned boundary conditions are given in section 2.8.

The 'V'-flame is anchored using numerical flame holder method, wherein burnt gas properties are imposed at each timestep at the flame holder location, with respect to CFM-LES, the burnt gas properties are imposed interms of flame surface density and progress variable using Gaussian function.

5.4.2 Combustion-LES results

Figure 5.6 shows, ensemble averages of progress variable and flame surface density in time and in the spanwise direction of the channel.

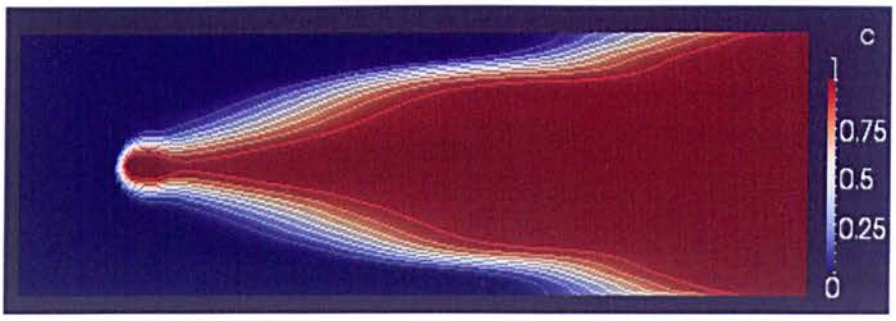

(a) Instantaneous progress variable contour plot

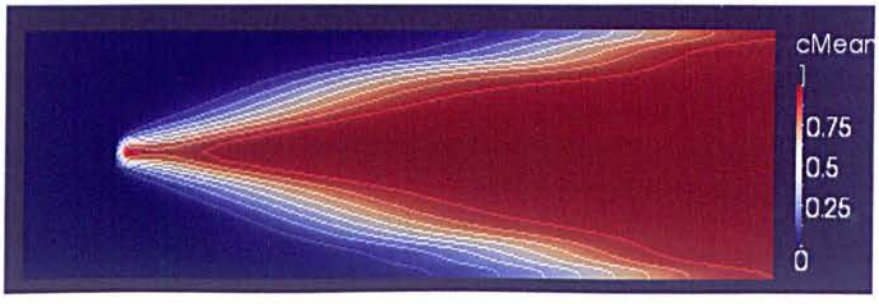

(b) Mean progress variable contour plot in vertical plane

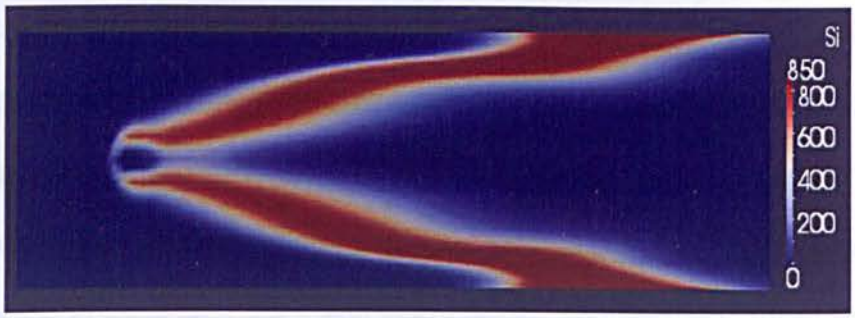

(c) Mean flame surface density contour plot in vertical plane

Figure 5.6. Turbulent 'V'-flame plots in the along the channel height

The instantaneous snapshot of the turbulent 'V'-flame is been shown in figure 5.7, The coherent flow structures are plotted in terms of second invariant of velocity gradient tensor (Q - Method) ,superimpose with vortices magnitude. The red and blue coloured iso-surfaces represent opposite signs of vortices rotation respectively. The flame front is plotted as iso-surface of progress variable c = 0.5 is black colour.

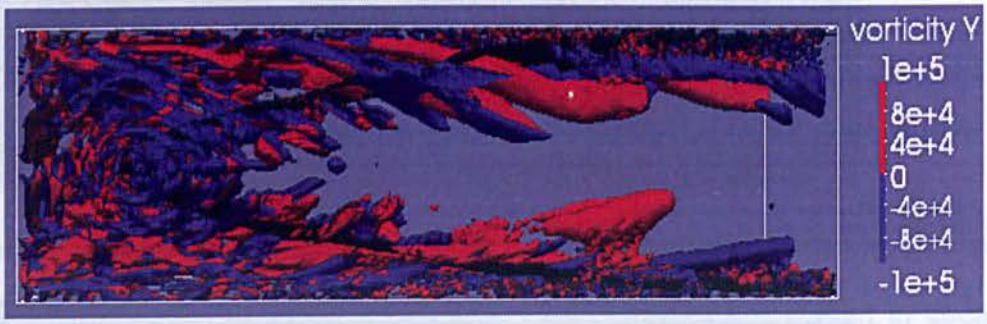

Figure 5.7. Instantaneous snapshot of turbulent 'V'-flame in a channel Interacting with flow structures.

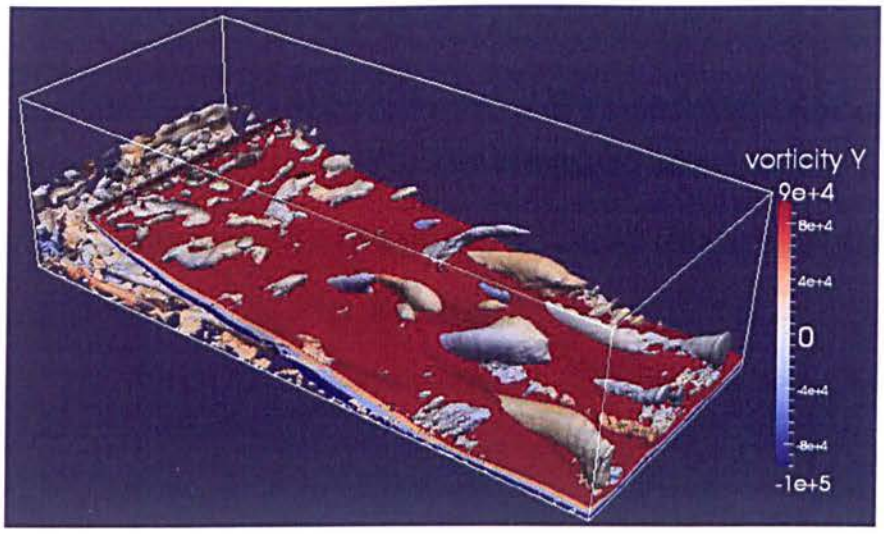

Figure 5.8. Instantaneous snapshot of the lower half of turbulent 'V'-flame interacting with boundary layer

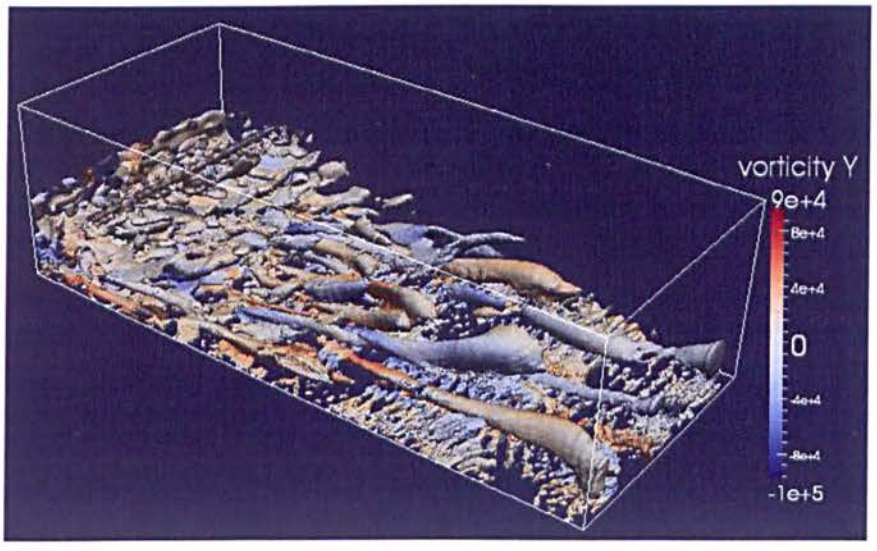

Figure 5.9. Instantaneous snapshot of the lower wall coherent flow structures (without flame front)

The interaction of the flame-front with the turbulent boundary layer is shown in figure 5.8 and 5.9. The heat release at flame front is altering the flow structures and elongating them due to increase in strain rate cause by expanding gases and flame is getting wrinkled due to the flow structures.

This strain rate creates additional flame acceleration, but this can also lead to complete flame quenching if the strain rate are above their critical limits.

The quantitative comparison is done for flame displacement speed (S_d) and the wall heat flux in figure 5.10 and 5.11 respectively. In the DNS case, the results are normalized using the laminar flame quantities. In order to compare with the LES predictions, the DNS results are rescaled using laminar flame quantities (Laminar flame quantities are presented in Appendix-A).

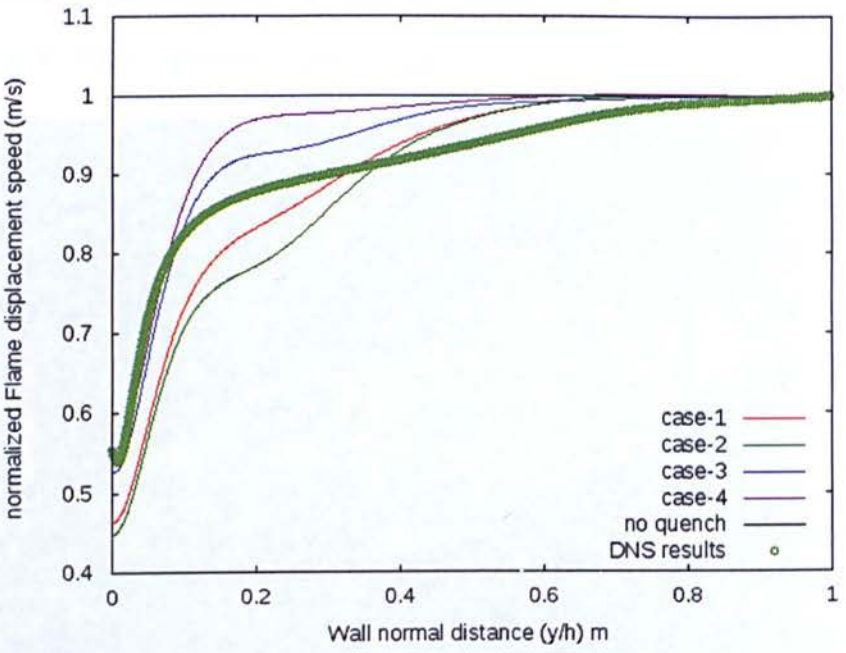

Figure 5.10. Normalized Flame displacement speed long channel height.

Case 1 – (γ_q = 5 , γ_d= 0.3), Case 2 – (γ_q = 5 , γ_d= 0.5),

Case 3 – (γ_q = 15 , γ_d= 0.3), Case 4 – (γ_q = 15 , γ_d= 0.5)

The flame displacement speed for the Isosurface of progress variable c = 0.7 is extracted from the flow field by first averaging the flow quantities in the spanwise direction and then using a visualizing tool (paraFOAM) to plot the

iso-contours for progress variable c = 0.7. Without the flame-wall interaction modeling the 'V' flame in the channel was not stable and within a few iterations the flame in the boundary layer quickly reached (flash back) the inlet plane. Also some of the combination of γ_q and γ_d resulted in unstable flame.

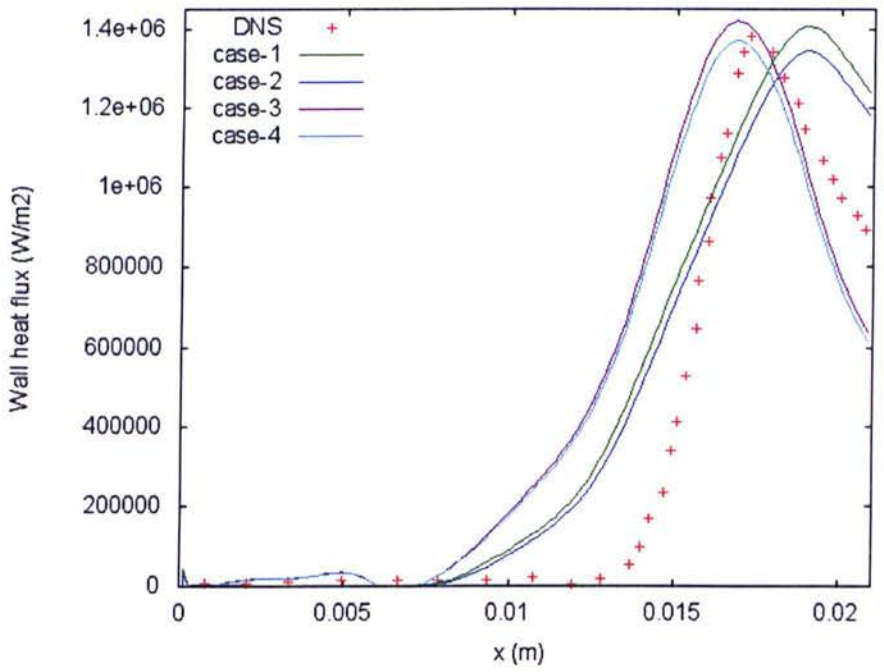

Figure 5.11. Comparing LES wall heat flux with DNS

The peak wall heat fluxes values are slightly different from those of the DNS results, but they are very much in the magnitude of laminar wall heat flux variations. Secondly the gradient of the wall heat flux also differs from that of the DNS. One of the reasons could be the difference in flame thickness obtained in LES and DNS. It has been reported by (Alshaalan and Rutland, 2002, Gruber et al., 2010), that the peak turbulent wall heat fluxes are in the order of ~ 1.4 MW/m^2, which is very well captured in the present LES simulations. Therefore the quantitative comparison of results leads to flame-

wall model constants to be γ_q = 15, and γ_d = 0.3 (case-3). Out of the two constants, γ_q is more dominant parameter.

Hydrogen fuel is well known to be more diffusive and highly reactive. The flame-wall interaction model constants have been obtained in posteriori test using hydrogen as fuel, therefore it is expected that there will be some order of magnitude errors in predicting wall heat fluxes, when simulating flame deflagrations of other fuels using the model constants deduced in the present study.

5.5 Summary

The flame-wall interactions are studied in three configurations namely: head-on, side-wall and tube quenching, they are further categorized as laminar and turbulent flame interaction. The laminar flame-wall interactions are well studied by many researchers, but owing to the experimental difficulties and high computation cost of DNS of turbulent flows, very few numerical and experimental works are present to fully understand and model the turbulent flame wall interactions.

Flame-wall interaction improvements are incorporated in CFM-LES based on few recent research studies on turbulent flame-wall interaction. The CFM-LES governing equations are modified in the near-wall region to capture the turbulent flame-wall interactions. The modifications have incorporated changes for laminar flame speed, annihilation and propagation through a flame quenching factor which is a function of enthalpy loss, heat release factor & reduced activation energy, and changes in turbulent length scales using van-Driest damping coefficient for viscosity.

A non-isobaric enthalpy loss factor similar to the definition used by (Angelberger et al., 1997) is adopted in present study to identify the near wall flame influenced zone. Finally posteriori test of 'V'-flame stabilized in a channel base on DNS results of (Gruber et al., 2010) is analysed to fix the two flame-wall interaction model constants. The flame displacement speed and wall heat flux plots in the DNS results of (Gruber et al., 2010) are primary modeling parameters in CFM. Hence the results of (Gruber et al., 2010) are more appropriate for model validation study of CFM-LES. The model constants in the flame-wall interactions were assigned the values of γ_q = 15, and γ_d = 0.3 respectively based on posteriori test.

Chapter 6

CASE STUDIES

6.1 Introduction

The model prediction of the developed CFM-LES solver and wall interactions in OpenFOAM are assessed by simulating the flame deflagrations in, a) quenching of flame in a quench mesh, b) turbulent flame propagation in a repeated obstructed channel and c) large scale deflagration in hydrogen cylinder storage facility.

All three considered test cases are simulated using one equation eddy viscosity model for computing sub-grid turbulence kinetic energy (equation 2.23). The discretisation scheme for the time derivatives is implicit backward scheme, which is second order accurate. The convective terms are discretized using second order accurate Gaussian-Gamma bounded scheme. The diffusion terms are discretized using Gaussian linear corrected scheme which is central differencing, with explicit non-orthogonal correction. Finally the gradient terms are solved using Gaussian linear scheme which is also central differencing. Further details and implementation of the numerical schemes in OpenFOAM can be accessed in (Weller et al., 1998b, H. Jasak et al., 1999, OpenFOAM, 2014). Therefore, the combinations of above discretisation scheme make the present numerical solver second order accurate in both time and space. In the following sections the individual test case are discussed in detail.

6.2 Quenching Mesh

6.2.1 Introduction

Flame quenching by fine mesh is one of the oldest known methods for mitigating flame propagation. Sir Humphry Davy pioneered the study of flame wall quenching while developing the mining safety lamp. There are no well established test cases to validate the modelled turbulent flame quenching processes. Therefore a known application of the flame quenching – quench mesh, is chosen to carry out calculations for turbulent flame deflagration in a stoichiometric methane-air mixture through single gap of the mesh. The application of quench mesh is often as a safety measure around the fuel handling installation to prevent any uncontrolled flame deflagration by quenching the flame.

6.2.2 Numerical setup

The ignition was initiated with a spark in the still mixture. Once the flame front is established, the reacting methane-air at stoichiometric is allowed to expand through the quenching mesh. The dimension of the quenching mesh wire is 0.3 mm diameter and the gap between the wires is also 0.3 mm. such fine gaps in quenching mesh or in flame arrestor are known Minimum experimental safe gap (MESG). MESG value depends on operating pressure, temperature and fuel type.

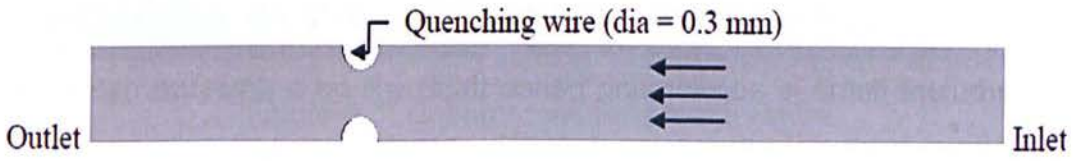

Figure 6.1. Quenching mesh domain

The flow direction of the reacting mixture is from Inlet to Outlet boundary as shown in Figure 6.1. To be more conservative, mesh gap size is chosen to be of 0.3 mm, this value is applicable to commonly used fuels : methane, hydrogen and propane. The multi block structure is used with cell size around 10 μm considering the mesh resolution requirement studied by (Kim et al., 2006), The top and bottom surfaces are specified as cyclic boundary conditions while the front and back surfaces are specified as symmetric. The isothermal boundary condition is imposed on the wall (mesh surfaces). The wall-flow interaction is accounted for by the log law wall function. The initial conditions are set as 300 K and 1 atmosphere pressure. The other conditions are u' = 0.1 mm/s, methane-air at equivalence ratio = 1.0. Due to symmetry of the geometry only half of the section shown in Figure 6.1 is numerically computed.

6.2.3 Simulation results

(Angelberger et al., 1997) applied the enthalpy loss factor only for the boundary wall cells in their internal combustion engine computation, but the effect of the enthalpy loss extends up to some distance from the wall. Hence, in the present study, the enthalpy loss factor was computed in front of the flame and in the near wall region based on nonisobaric enthalpy loss factor.

The flame is characterized by the progress variable between 0.01 to 0.99, $c < 0.01$ is unburnt reactants and $c > 0.99$ are burnt products. The turbulent flame is accelerating hence there will be a pressure rise in front of the flame due to adiabatic compression of the reactants.

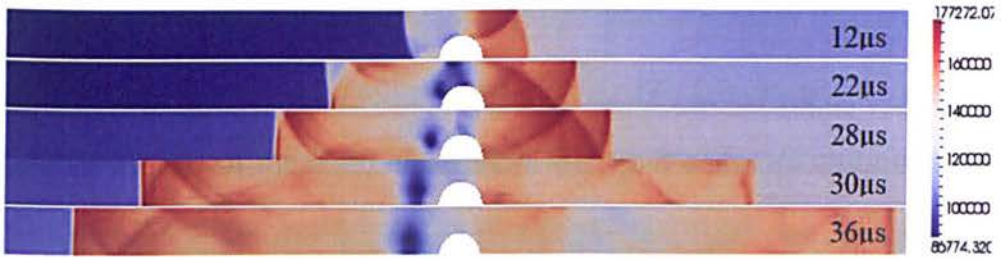

Figure 6.2. Pressure wave propagation in front of the flame

As shown in Fig. 6.2, the instantaneous pressure (Pa) rise due to flame acceleration is further magnified because of the semi confinement. This rise in pressure in the wire gap reduces the mass flow rate and increases the flame residence time. This in effect enhances heat transfer from the flame front to the wall. After the flame passes through the narrow gap, its temperature drops considerably due to expansion.

The peak laminar flame speed obtained in the simulation was 0.427 m/s from the base value of 0.40 m/s based on the power law correlation for unstretched laminar flame speed (discussed in section 3.4). For methane-air mixture, its laminar flame speed decreases with pressure and increases with temperature.

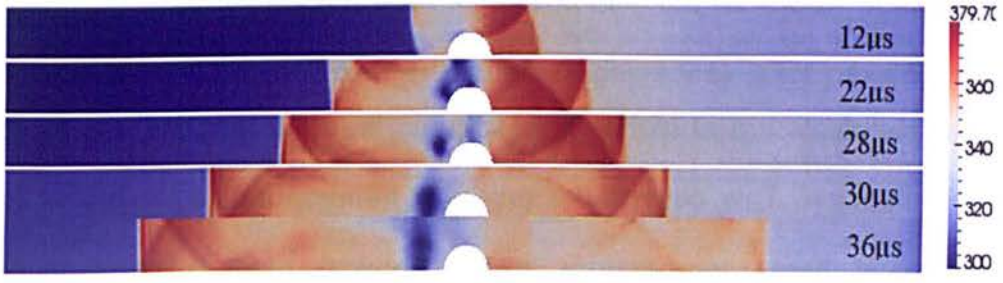

Figure 6.3. Unburnt reactants temperature

The unburnt reactants temperature increases due to adiabatic compression is shown in figure 6.3. Since the laminar flame speed is more sensitive to temperature increase than any increase in pressure as shown by the relative values of the temperature and pressure exponents in section 3.4, the reactants temperature rise result in the acceleration of the flame.

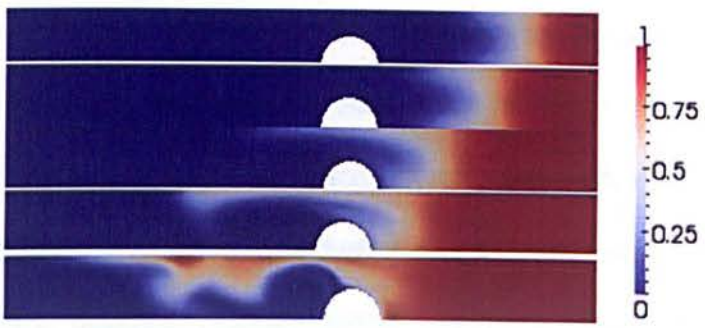

Figure 6.4. Progress variable plot without flame-wall interaction

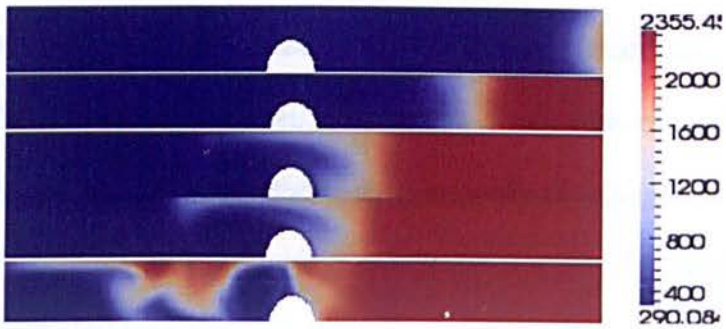

Figure 6.5. Temperature plot without flame-wall interaction.

The reactants are at higher temperatures than the ambient due to adiabatic compression. This causes the products temperature to be higher than the adiabatic flame temperature once chemical heat is released. Without implementing the flame wall interaction, the computed flame is not quenched at the quenching mesh and the flame passes though the mesh gap as shown

in Figure. 6.4 and 6.5. There is even rise in temperature of the mixture after the quenching mesh. Even though there is heat loss at the wall.

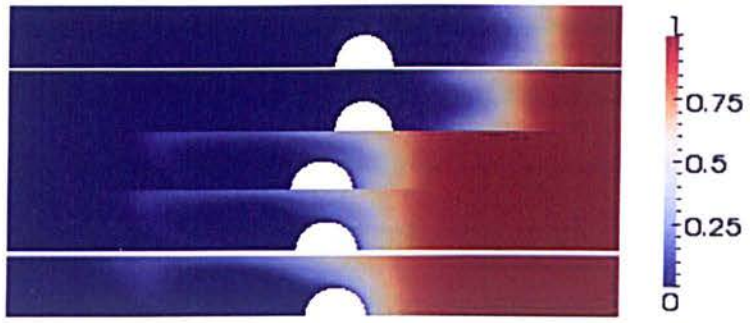

Figure 6.6. Progress variable plot with flame-wall interaction

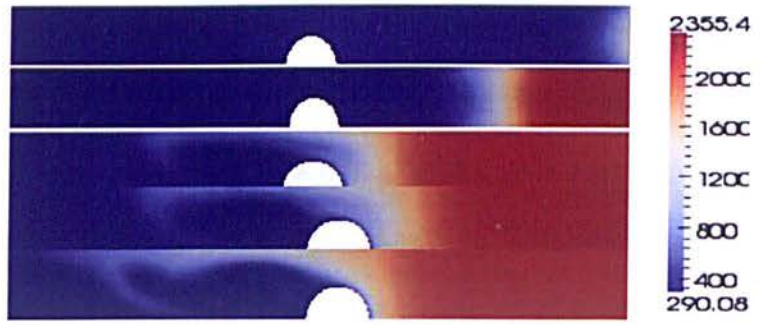

Figure 6.7. Temperature plot with flame-wall interaction.

With the modified model which accounts for flame-wall interaction, the progress variable values are convected and diffused as shown in figure. 6.6. The flame temperature shown in figure 6.7 decreases after passing though the quenching mesh. Eventually the flame will completely extinguish as the fuel is consumed in the reaction zone. Numerical simulation of flame extinction requires large simulation time as the process is slow and driven by molecular diffusion effect only.

6.2.4 Conclusion

The quenching of turbulent flame at the mesh gap of a single quench mesh is been simulated using the CFM-LES solver. Numerically simulated flame quenching at the wall, was modelled using both flow-wall and flame-wall interactions. To accurately predict the flame affect region, a non-isobaric enthalpy loss formulation is been used. The quenching process was numerically simulated only due to heat loss to wall but factually, it's a coupled thermo physical process involving heat transfer, flame stretch, radical absorption and preferential diffusion. The present numerical results have demonstrated the CFM-LES along with wall interactions capabilities in predicting the flame quenching process numerically. The model is able to simulate the heat loss, changing characteristics of the turbulent premixed flame and turbulence length scales in the near-wall region.

6.3 Flame propagation in obstructed channel

6.3.1 Introduction

Flame propagation in obstructed channels has been studied for many years primarily in connection with explosion safety. The interaction of the flame and the unburned gas flow field generated ahead of the flame provides an efficient feed-back loop that can lead to flame acceleration up to a velocity relative to a fixed observer on the order of the speed of sound of the combustion products, i.e., roughly 1000 m/s. Initially the geometric increase in flame area caused by the large-scale flow structures produced by the obstacles is responsible for flame acceleration. As flame acceleration proceeds and the unburned gas flow becomes turbulent, the transport of mass and momentum

into the flame is augmented and the resulting increase in the burning rate further enhances flame acceleration. As a result of these two effects, strong flame acceleration can lead to the production of a precursor shock wave with overpressures on the order of the adiabatic constant volume explosion pressure (Johansen and Ciccarelli, 2009). The flame acceleration process is governed by several parameters, including mixture reactivity and the ratio of the obstacle blockage area and the channel cross-section area, i.e., BR = (1 – h/H).

6.3.2 Experiment details

The apparatus used for this experiment was a closed ended 3.66 m long, 7.6 cm by 7.6 cm square channel consisting of six equal length interchangeable modules (Ciccarelli et al., 2010). One of the six modules was equipped with side mounted glass windows for optical access. Each non-optical module was equipped with two instrumentation ports spaced 30.5 cm apart and 15.2 cm from the end flanges on both the top and bottom surfaces. The optical module was placed at different positions downstream of the ignition point (module position 1) in order to capture the entire flame acceleration process.

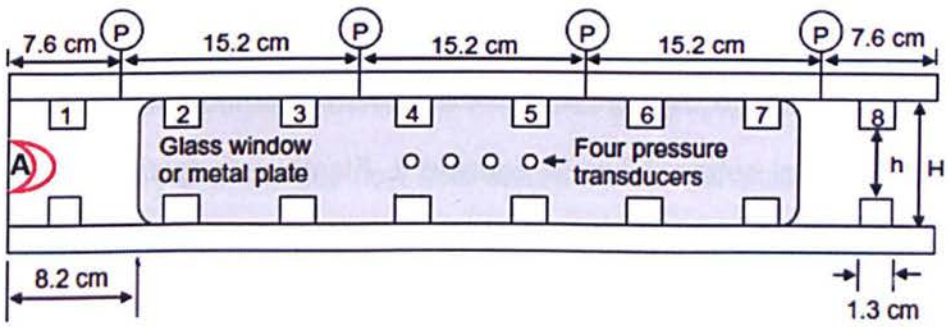

Figure 6.8. Schematic showing the optical module

Details of the window and instrument port locations for the optical module are provided in Figure 6.8, there are four instrumentation ports on the top and bottom surfaces. Instrumentation included PCB piezoelectric pressure transducers and ionization probes that protruded 1.5 cm into the channel to obtain flame time-of-arrival information. The 1.27 cm thick fence type obstacles were equally spaced at the channel height (i.e. 7.6 cm). Three different obstacle heights, corresponding to flow area blockages (BR = 1 - h/H) of 0.33, 0.5 and 0.67, were tested.

The experiments were carried out using stoichiometric methane–air, which was prepared in a separate mixing chamber via the method of partial pressures. The mixing chamber was equipped with an impeller that was driven externally by a pneumatic motor. After 15 min of mixing and 30 min of evacuation of the channel down to a pressure of 0.2 kPa absolute, the methane–air mixture was loaded into the apparatus to a final pressure of 47 kPa absolute. Ignition of the mixture is facilitated through the capacitive discharge of approximately 250 mJ of energy through an automotive spark plug mounted on the centre of one of the end flanges, which is designated as position 'A' in Figure 6.8.

6.3.3 Numerical setup

The computation domain is modelled with same dimensions as that of the experimental setup shown in figure 6.8. Flame propagation was initiated by providing an initial progress variable and flame surface density distribution at the site of spark ignition in experiments. The computation domain was discretised with fine mesh of ~ 5 mm in the optical module section and coarse

mesh of ~ 1 cm in the opaque module sections. The enclosing wall is treated as isothermal at 298 K. and the initial pressure in the channel was set at 47 kPa. The channel is filled with methane-air at equivalence ratio = 1.0. The initial turbulent flow files was set as a random field with u'=1 cm/s. Simulations are carried out for three different obstacle heights, corresponding to flow area blockages (BR = 1 - h/H) of 0.33, 0.5 and 0.67.

6.3.4 Numerical simulation results

i) Case 1, BR = 0.67

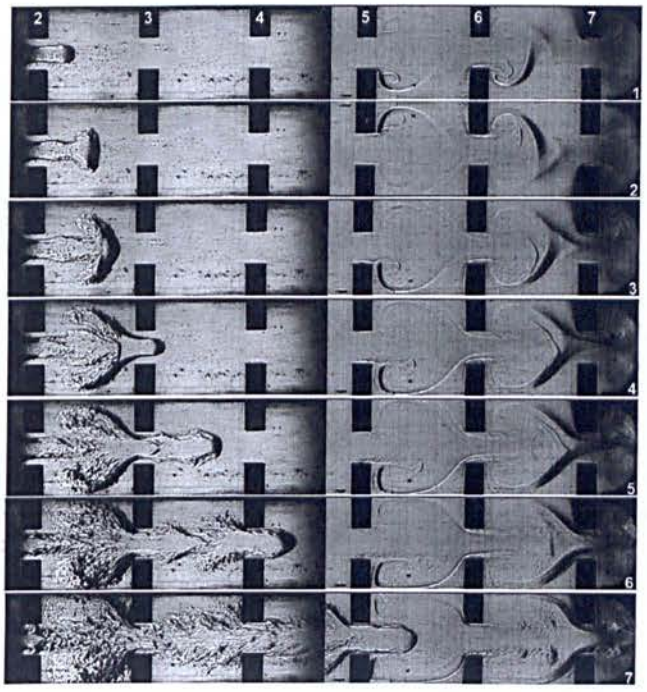

Figure 6.9. Experimental schlieren images of development of the flame surface and the unburned gas flow field ahead for 0.67 BR, Inter-frame time is 0.67 ms

The numerical simulation time were adjusted to have similar flame location as that of the experiments after obstacle numbered 2 in figure 6.9, thereafter simulation results written at output were collected for regular time intervals of 0.67 ms. The part (a) of figure 6.10, is showing flame propagation modelled with wall interaction and part (b) is showing the same results without flame-wall interaction. The flame front seems to be laminar in the initial time frames and later changed to turbulent.

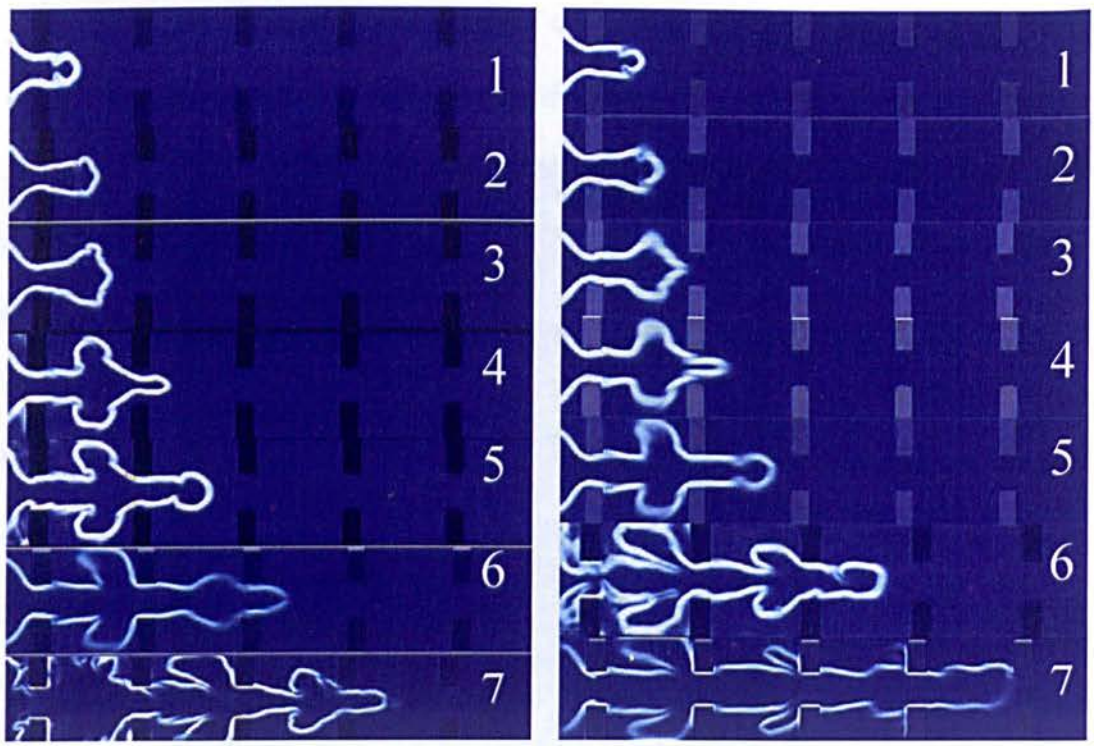

(a) with flame-wall model (b) without flame wall model

Figure 6.10. Schlieren (magnitude of density gradient) plot of flame propagation with inter-frame time is 0.67 ms

The predictions of the flame front propagation with flame-wall interactions match qualitatively well with experiments and simulations results without flame-wall interactions seems to over predict in the later time frames (6, 7, 8).

The expansion of the hot gases in the initial obstacle sections contribute for the flame acceleration. Apart for the expanding gases, the shear layer established at the tip of the obstacles is also contributing for the flame acceleration as observed in experimental results.

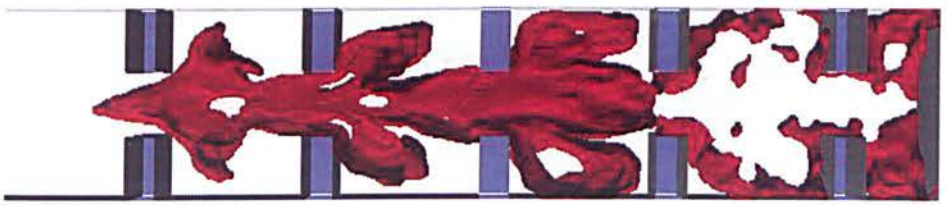

Figure 6.11. Iso surface for progress variable(c = 0.1) – location of flame front

The figure 6.11 is showing the flame front location with respect to the wall surface. The flame spread first happens in the recirculation zone adjacent to the obstacle and then the remains unburnt fuel engulfs in rapid phase creating hot expanding gas.

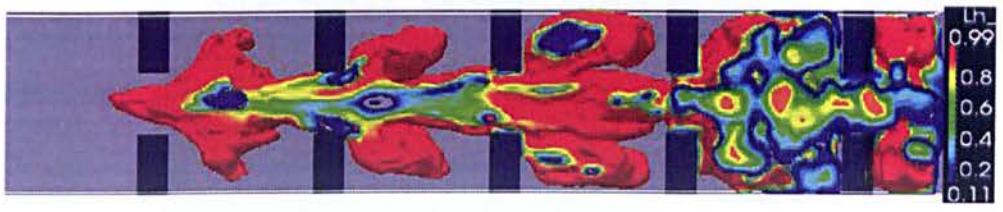

Figure 6.12. Isosurface for progress variable (c = 0.1) – superimposed by enthalpy loss factor

The figure 6.12 is showing the flame front superimposed by the enthalpy loss factor, giving indication about the flame-wall interaction region. When reduction in laminar flame speed is accounted based on heat loss, the

expansion of the hot gases is reduced leading to proper flame acceleration at the flame front due to shear layer mixing at the edge of the obstacles rather than the excess expansion of combustion products.

2) Case 2 : with BR = 0.33

The experimental schlieren images of flame surface development and the unburned gas flow field ahead for 0.33 BR, Inter-frame time 1 ms are presented in figure 6.13. The numerical results in comparison to experiments are shown in figure 6.14, using progress variable and in figure 6.15, using numerical schlieren variable for 0.33 BR, Inter-frame time 1 ms.

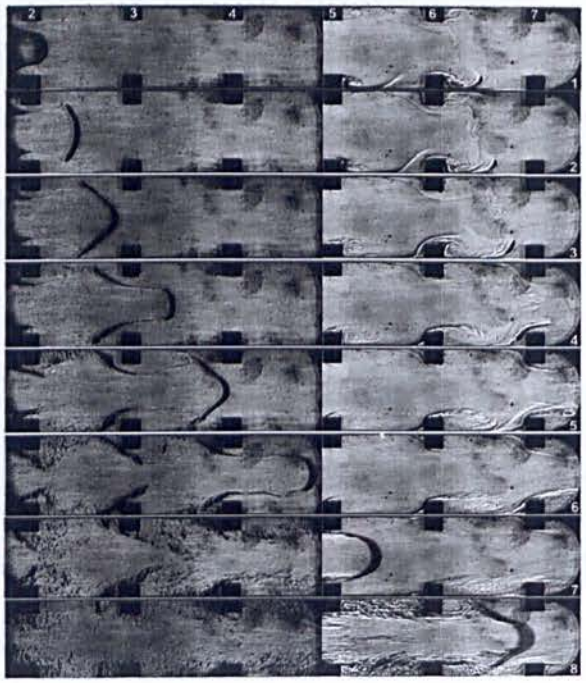

Figure 6.13. Experimental schlieren images of development of the flame surface and the unburned gas flow field ahead for 0.33 BR, Inter-frame time 1 ms

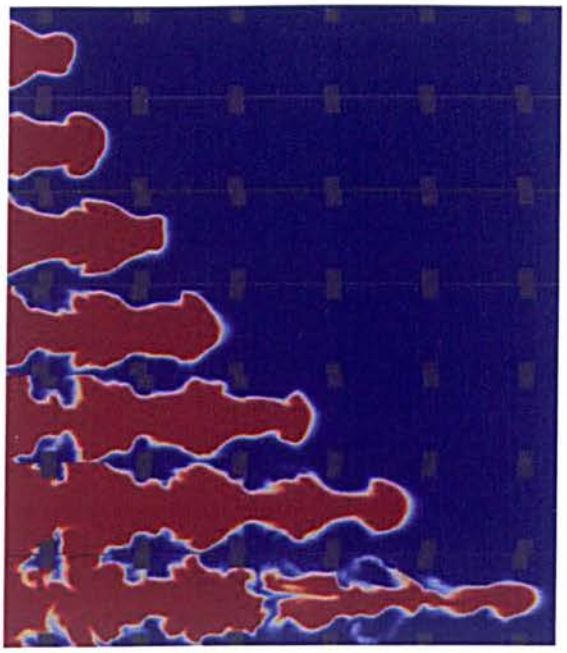

Figure 6.14. Progress variable plot of development of the flame for 0.33 BR, Inter-frame time of 1ms

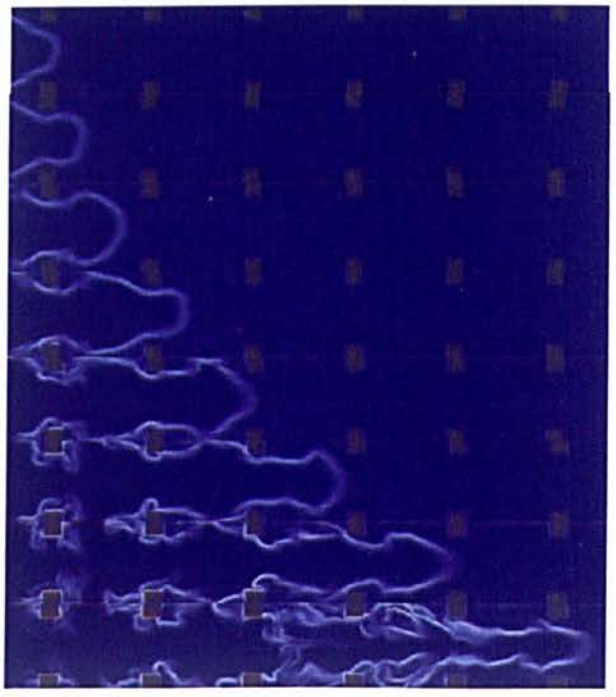

Figure 6.15. Numerical schlieren plots of development of the flame surface for 0.33 BR, Inter-frame time is 1 ms.

3) Case 3 : with BR = 0.50

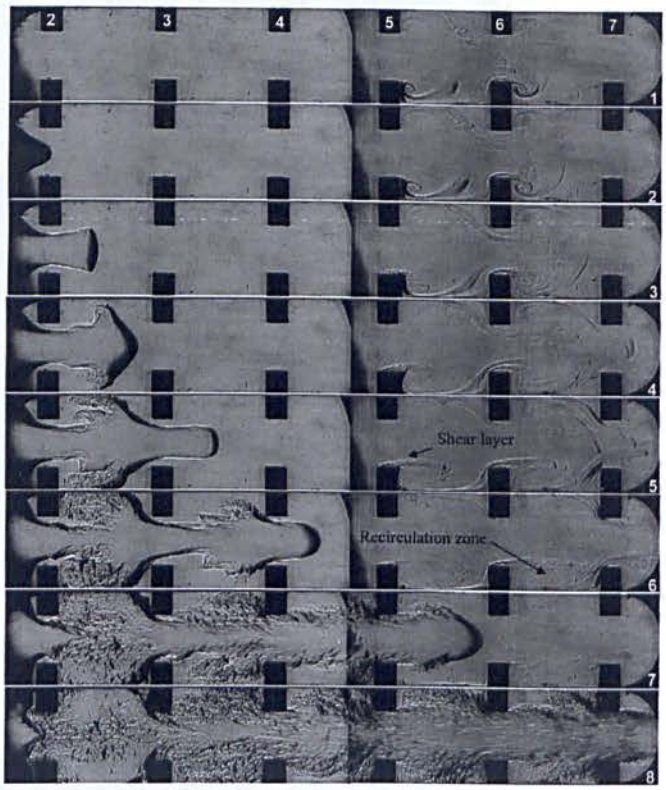

Figure 6.16. Experimental schlieren images of development of the flame surface and the unburned gas flow field ahead for 0.5 BR, Inter-frame time is 1 ms.

The experimental schlieren images of flame surface development and the unburned gas flow field ahead for 0.50 BR, Inter-frame time 1 ms are presented in figure 6.16. The numerical results in the same inter-frame time of 1 ms are shown in figure 6.17, using numerical schlieren variable and in figure 6.18, using progress variable for 0.50 BR. The numerical schlieren plot is computed as gradient of the density field. The fine fluctuations in the density field are discernible in the present LES simulation as that in the experiments.

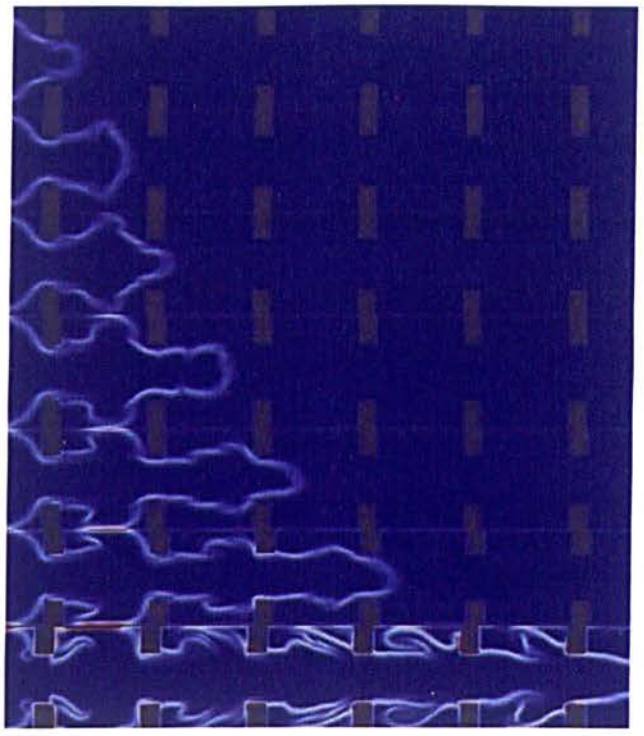

Figure 6.17. Numerical schlieren images of development of the flame surface for 0.5 BR, Inter-frame time is 1 ms.

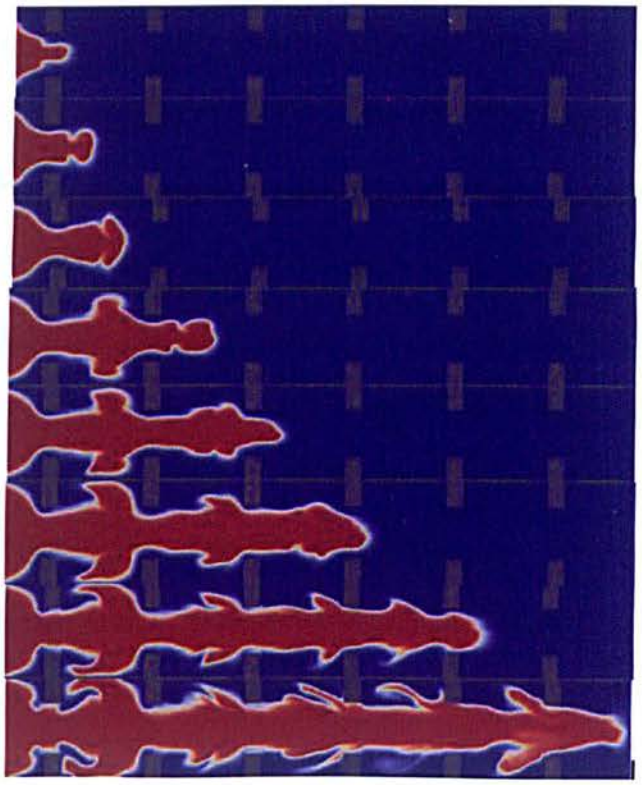

Figure 6.18. Progress variable plot of development of the flame for 0.50 BR, Inter-frame time of 1ms

Considering the numerical results for flame propagation in three case of BR=0.33, 0.50 and 0.67, establish that the modification for wall interaction in the combustion model have improved the results. In all three cases, the initial flame propagation was laminar and later once influenced by the obstacles; interact with varying level of turbulence leading to different flame accelerations.

6.2.4 Conclusions

The turbulent flame deflagrations have been carried out in repeated obstacle channel for three blockage ratios 0.33, 0.5 and 0.67. The flame–wall interactions are shown in figures for BR=0.67 case. The flame tip remains laminar initially and later changes to turbulent. The heat loss at the flame tip is negligible. The major heat loss is happening at the flame front spreading in the obstacle chambers. The early development of the unburnt gas flow field and flame shapes appears to be universal in three cases. However the rate at which the flame evolves later is different, which is evident of the fact that the surface flame area generation was different in the three cases. The CFM-LES is able to predict the different rates of the flame generation due to different blockage ratio, hence the different rate of flame accelerations. The flame-wall interactions were mainly playing the role in controlling the heat loss once the flame spreads in the obstacle chambers. The numerical schlieren plot compare well with trends of experimental schlieren plot, therefore validate CFM-LES solver for flame acceleration studies.

6.4 Large scale hydrogen flame deflagrations

6.4.1. Introduction

Hydrogen as fuel has the highest energy content by mass but the lowest by volume. To have higher energy density, hydrogen is typically stored under higher pressures (30-300 bars) in comparison to other gaseous fuels. Accidental release of hydrogen during its handling can lead to formation of ignitable mixture in a very short time. Future wide use of hydrogen as vehicle fuel demands safe handling guidelines and insight of explosion hazards in hydrogen installations as well as during its production and transportation. One of the major potential applications of hydrogen is in hydrogen fuel cells vehicles, which could result in the need for the general public to handle high pressure hydrogen during the refuelling process. It is hence recognized that these hydrogen refuelling stations would need to have a higher level of safeguards and integrity than those currently used in chemical industries where only a limited number of highly trained personnel are involved. This would call for the provision of safe infrastructure of hydrogen refuelling stations. To address these issues considerable amount of experimental and numerical work has been done in refuelling and storage environments. One of such experiments was conducted by shell global solution (UK) and HSL (UK) reported in (Roberts et al., 2005). Tests were done to study the maximum overpressures generated in an ignited downwards facing high pressure jet release and ignition in a premixed hydrogen-air cloud in a mock hydrogen storage facility.

In the present study, the worst case scenario where entire hydrogen storage cylinders are enveloped by a premixed hydrogen-air cloud is

numerically simulated. The computational domain mimics the experimental setup for premixed hydrogen-air cloud in a storage facility experimentally tested by (Roberts et al., 2005). This large scale storage facility experiment is of particular interest as to test the CFM-LES predictions in realistic scenarios.

6.4.2 Experimental setup

The experimental setup of the premixed hydrogen vapour cloud deflagration is shown in figure 6.19 and the details of the hydrogen storage cylinder are 0.80 m diameter and 0.25 m long, shown in figure 6.20.

The layouts of the experimental setup along with pressure monitoring points are shown in elevation view in figure 6.21 and in plan view in figure 6.22. Two experiments scenarios of different ignition locations are considered in the present study, Case A – location (P1) close to high wall and another Case B- location (P4) close to low wall. The basic details of the two cases studied are summarized in Table 6.1.

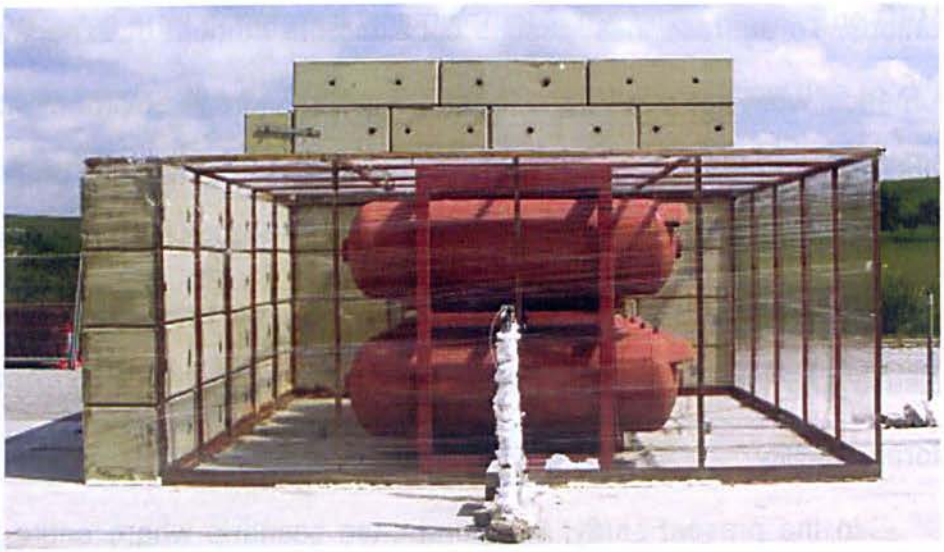

Figure 6.19. Experimental setup showing premixed vapor cloud enclosure

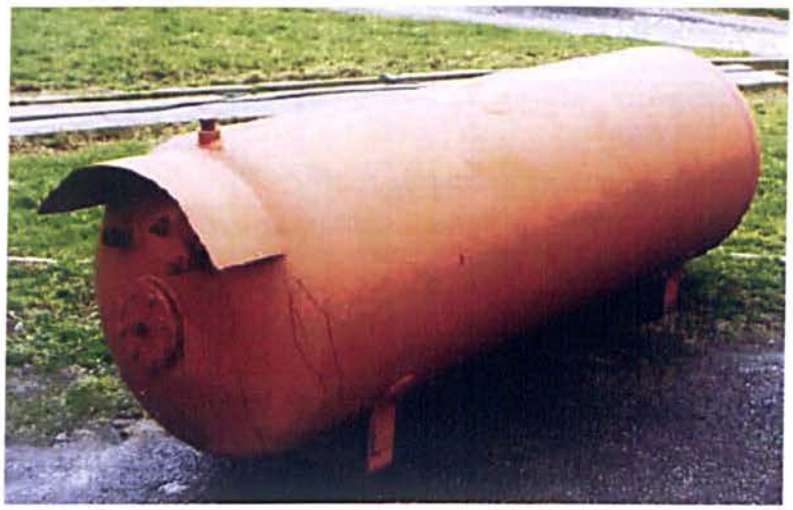

Figure 6.20. Storage cylinder details (0.80 m diameter and 0.25 m long)

The ignition location P1 and P4 are star mark in the plan view of the experimental setup (figure 6.22). The ignition in experiments is initiated using spark plug at the ignition location.

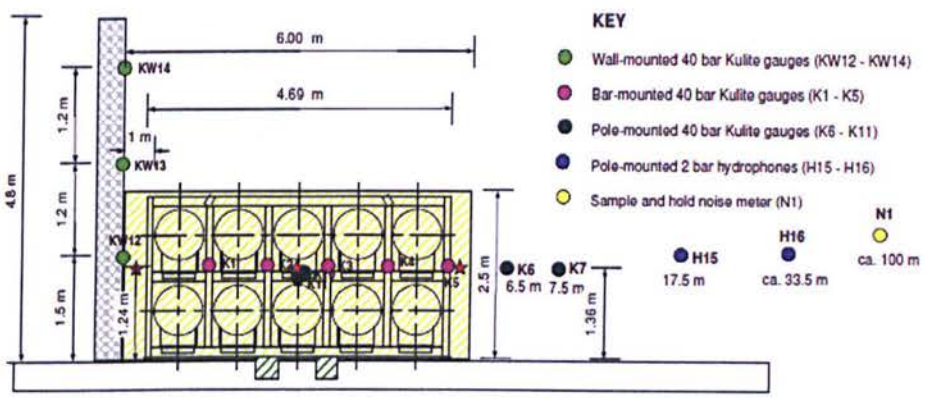

Figure 6.21. Experimental pressure (sensors) monitoring point locations (elevation view)

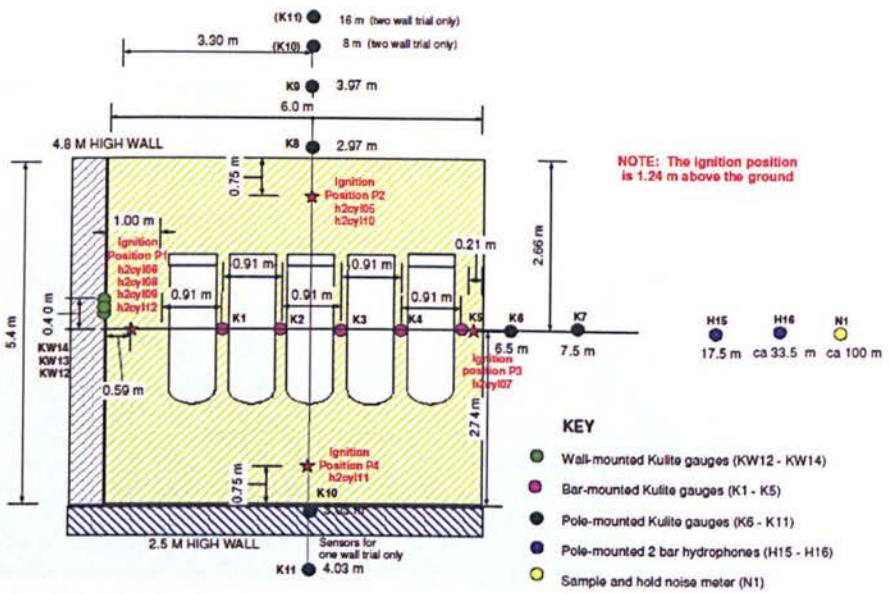

Figure 6.22. Experimental pressure (sensors) monitoring point locations (plan view)

The monitoring points which are laying within the computational domain size shown in figure 6.23 are only considered, hence outside the premixed cloud only next two monitoring location are present in numerical simulations. The list of pressure (sensors) monitoring point to measure the overpressures along with their locations are presented in table 6.2.

s. no	Parameter	Case A	Case B
1	Free volume (m3)	67.59	67.59
2	Ignition position (m)	P1 (0.59, 2.74, 1.24)	P4 (3.0, 0.75, 1.24)
3	Gas mixture temperature (K)	304.7	292.4
4	Mass of hydrogen (kg)	1.940	1.959
5	Stoichiometric ratio of mixture	1.27	1.22

Table 6.1. Experimental conditions

S. No	sensors	Location	Distance perpendicular to wall, (high, low) m	Distance above ground (m)	Position w.r.t premixed cloud
1	K1	Bar mounted	1.91 , 2.74	1.36	Inside
2	K2	Bar mounted	2.82 , 2.74	1.36	Inside
3	K3	Bar mounted	3.37 , 2.74	1.36	Inside
4	K4	Bar mounted	4.64 , 2.74	1.36	Inside
5	K5	Bar mounted	5.55 , 2.74	1.36	Inside
6	K6	Pole mounted	6.50 , 2.74	1.36	Outside
7	K7	Pole mounted	7.50 , 2.74	1.36	Outside
8	K8	Pole mounted	3.30 , 5.71	1.36	Outside
9	K9	Pole mounted	3.30 , 6.71	1.36	Outside
10	K12	Wall mounted	0.0 , 3.14	1.50	Inside
11	K13	Wall mounted	0.0 , 3.14	2.70	Outside
12	K14	Wall mounted	0.0 , 3.14	3.90	Outside

Table 6.2. Pressure probe locations (In each direction only next two monitoring points are considered outside the premixed cloud).

6.4.3 Numerical setup

Computational domain size considered is 16 m X 12 m X 10 m as shown in figure 6.23. and is discretized into structured mesh using multi block method. Total cell are around ~7.1 million. Initial velocity field is setup randomly with u' = 0.1 m/s and no wind velocity conditions at the boundary. The open boundaries are applied with 'waveTransmissive' pressure boundary condition and 'zeroGradient' boundary condition is applied for rest of the flow variables.

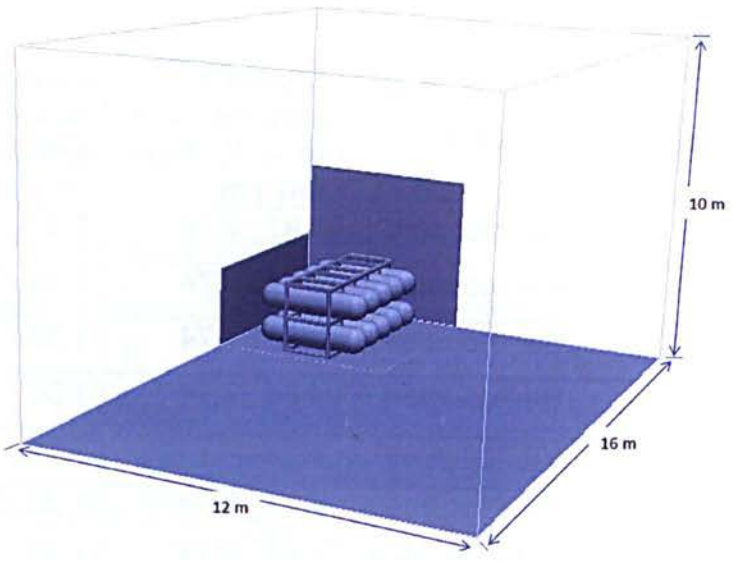

Figure 6.23. Computation domain enclosing the storage cylinders

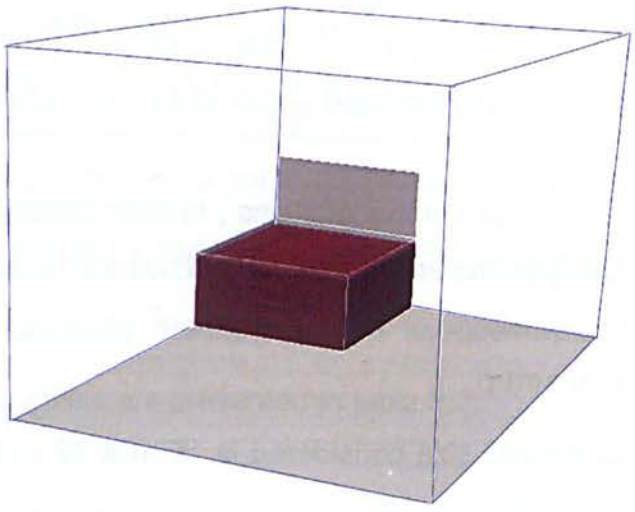

Figure 6.24. Initial premixed cloud enclosing the storage facility.

The premixed vapour cloud is initialized using 'setField' method in which the cell values of fuel mass fraction are updated to required value within the selected region. In the present case the selected region is of the dimensions of premixed vapour cloud shown in figure 6.24, which is 6 m X 5.4m X 2.5 m.

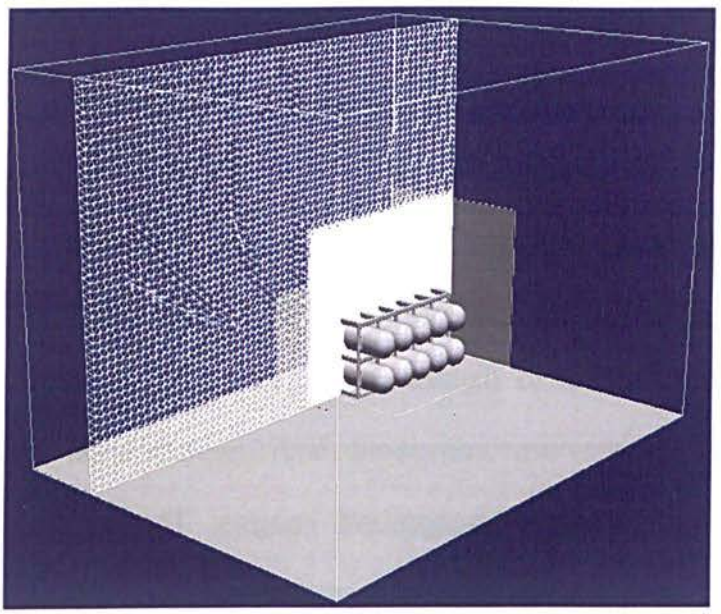

(a) Vertical cut plane

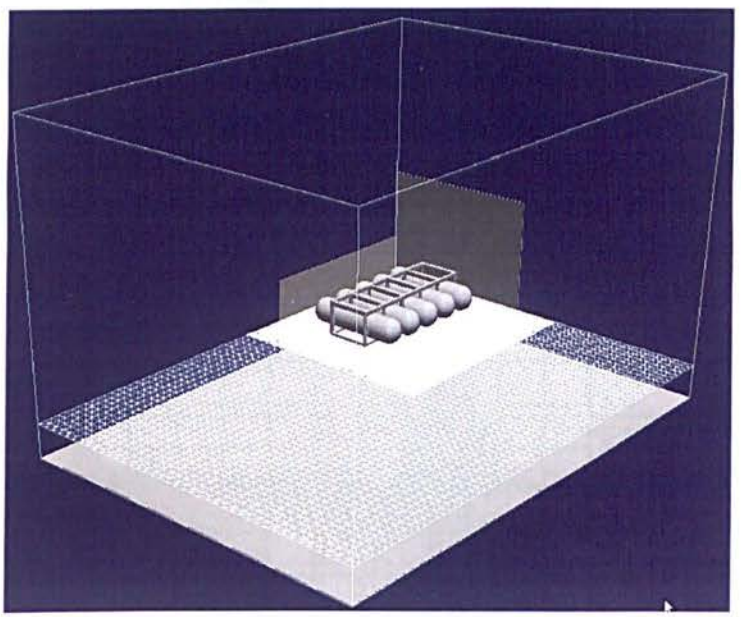

(b) Horizontal cut plane

Figure 6.25. Mesh distribution in vertical and horizontal plane.

The mesh distribution is been shown in figure 6.25, the mesh size within the initial premixed cloud is ~ 2-7 mm and outside the cloud is 20 cm. The flame

is initiated by applying patch of progress variable and flame surface density distribution using 'setField' method at the ignition location.

6.4.4 Numerical results

1) Case –A (High wall ignition – Two wall scenario)

It was not practical to digitize the experimental pressure trace plots, thus simulation results are compared with experimental data by using the experimental plots as background images. The legends for lines in the pressure trace plots are, Blue – Experimental results; Red – LES results. The numerical simulation results are moving averaged for 0.20 ms and plotted in the same scale as that of the experimental data to have one to one comparison with experimental data.

a) Monitoring points inside congestion

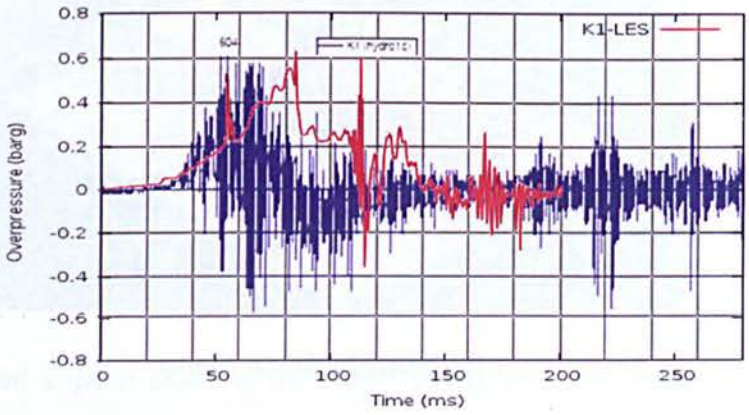

Figure 6.26. Pressure trace curve at K1

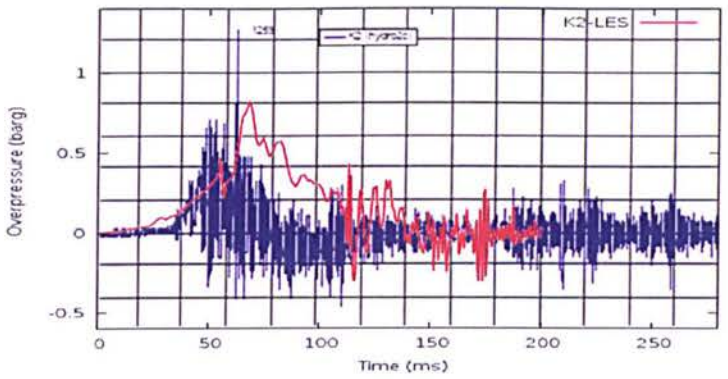

Figure 6.27. Pressure trace curve at K2

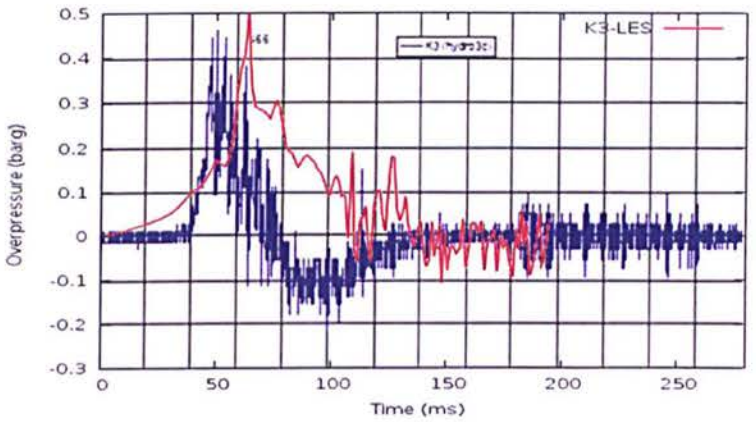

Figure 6.28. Pressure trace curve at K3

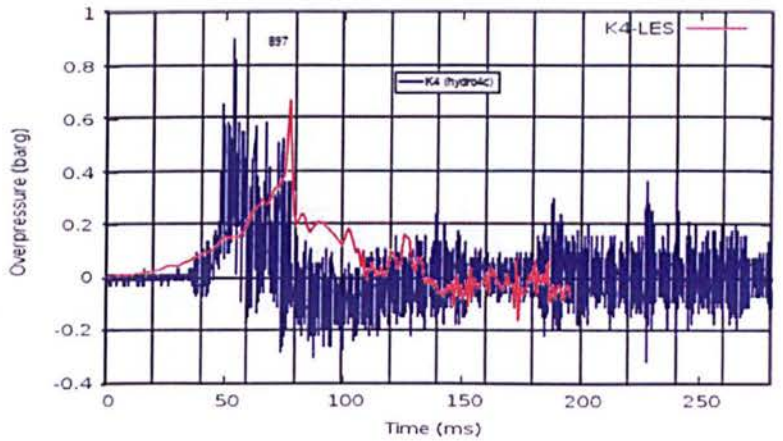

Figure 6.29. Pressure trace curve at K4

The numerical pressure trace curves at the monitoring points within the premixed cloud are shown in figure 6.26 to 6.29. It can be inferred from the pressure trace plots that the fluctuations in the pressure field are very high within the premixed cloud. The high fluctuations in the pressures field could be because of multiple reflections within the congestion of hydrogen storages cylinders.

b) Monitoring points outside congestion (opp. High wall)

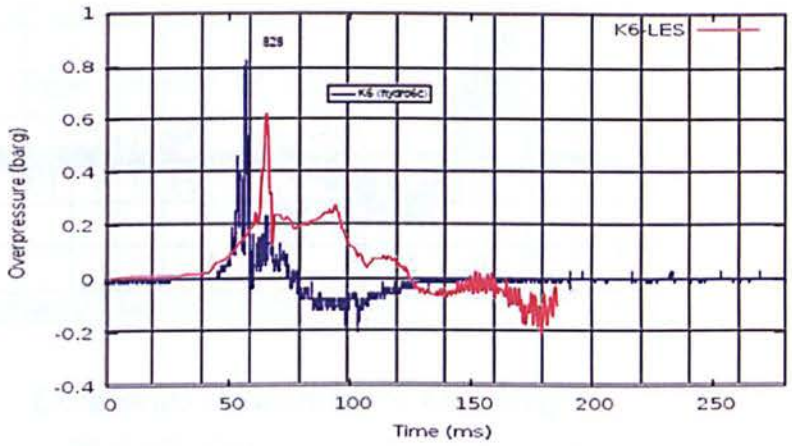

Figure 6.30. Pressure trace curve at K6

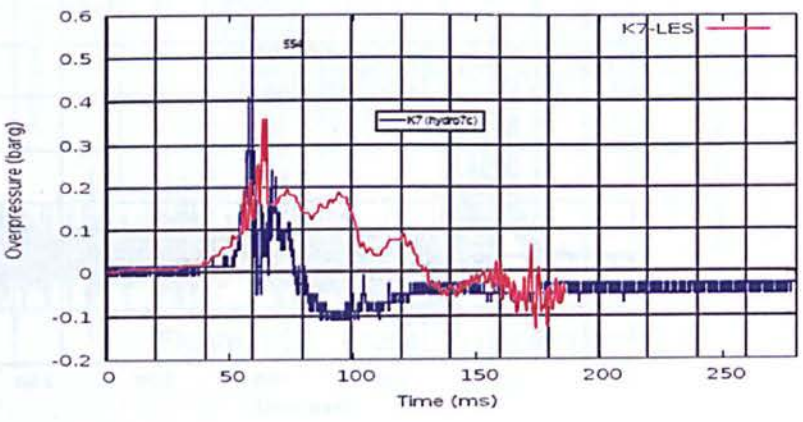

Figure 6.31. Pressure trace curve at K7

The numerical pressure trace curves at the monitoring points outside the premixed cloud and opposite in direction to high rise wall are shown in figure 6.30 and 6.31. Pressure traces are comparatively becoming less fluctuating outside the vapour cloud.

c) Monitoring points outside congestion (opp. Low wall)

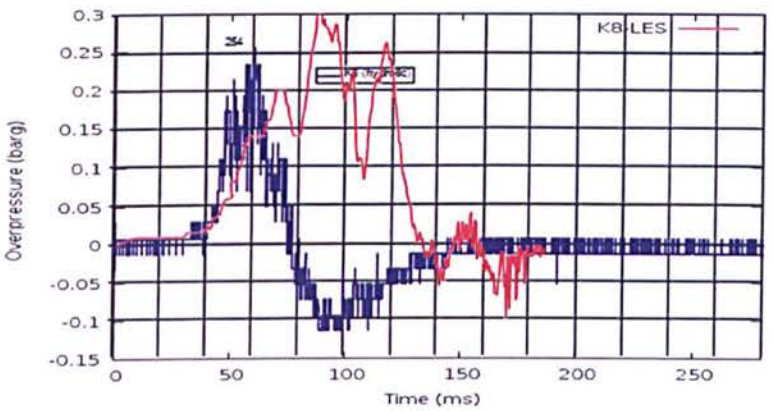

Figure 6.32. Pressure trace curve at K8

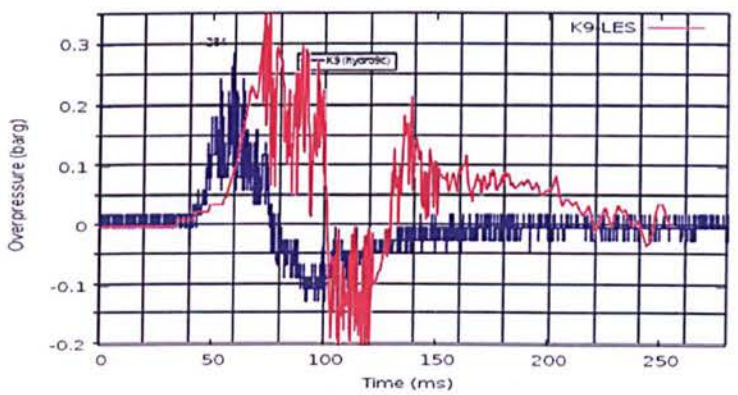

Figure 6.33. Pressure trace curve at K9

The numerical pressure trace curves at the monitoring points outside the premixed cloud and opposite in direction to low raise wall are shown in figure

6.32 and 6.33. Pressure traces are consistently over predicted in the direction opposite to the low rise wall boundary.

d) Monitoring points on the High wall

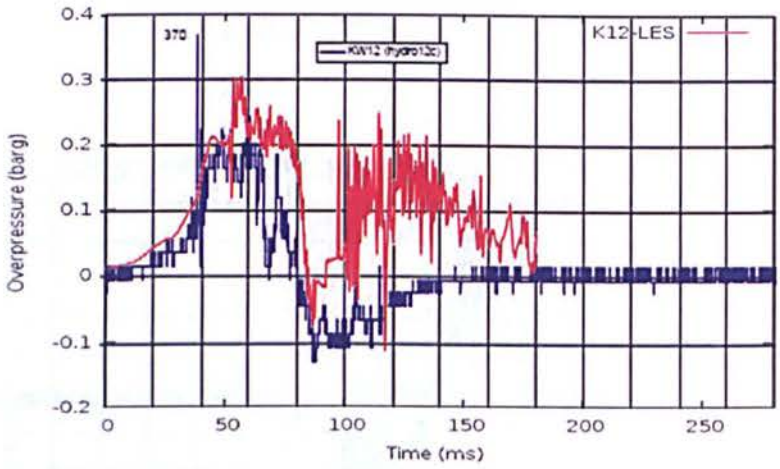

Figure 6.34. Pressure trace curve at K12

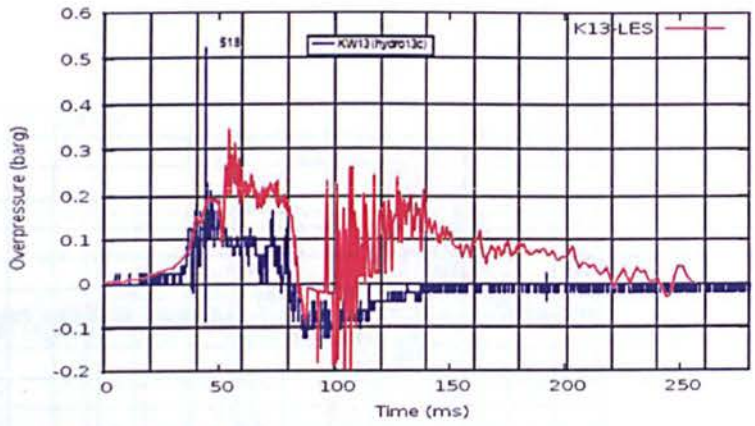

Figure 6.35. Pressure trace curve at K13

The numerical pressure trace curves at the monitoring points on the high rise wall are shown in figure 6.34 and 6.35. Pressure traces are having low fluctuations levels similar to that obtained outside the premixed cloud. The

instant peak pressure values for less than < 1ms obtained in experiments are not predicted in the numerical simulations. Whereas the initial trend of rise in overpressures wave is well predicted in numerical results.

S. no.	Sensor (Monitoring points)	Distance (m)	Expt. (barg)	Numerical (barg)
From High Wall				
1	K1	1.8	0.38	0.63
2	K2	2.7	0.42	0.82
3	K3	3.6	0.37	0.51
4	K4	4.5	0.56	0.67
5	K5	5.4	0.65	0.52
6	K6	6.5	0.73	0.62
7	K7	7.5	0.35	0.36
From Low wall				
8	K8	5.74	0.21	0.32
9	K9	6.74	0.23	0.41
Up wall from ground				
10	K12	1.5	0.25	0.31
11	K13	2.7	0.17	0.35

Table 6.3. Overpressure comparison at respective monitoring points

The peak overpressure values predicted in the numerical simulation at various monitoring points are summarized in table 6.3 along with experimental peak overpressure values and plotted in figure 6.36 for away from high wall direction.

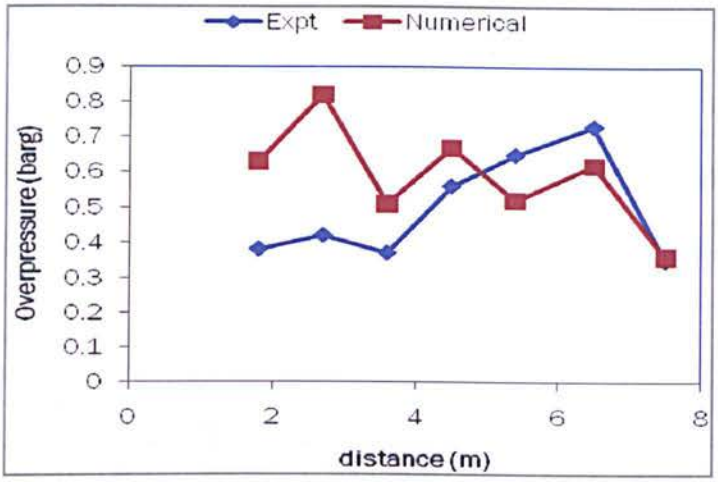

Figure 6.36. Overpressure comparison (distance away from High wall)

Case – B (low wall ignition – Two wall scenario)

The numerical simulation results are moving averaged for 0.25 ms and plotted in the same scale as that of the experimental data to have one to one comparison with experimental results.

a) Monitoring points inside congestion

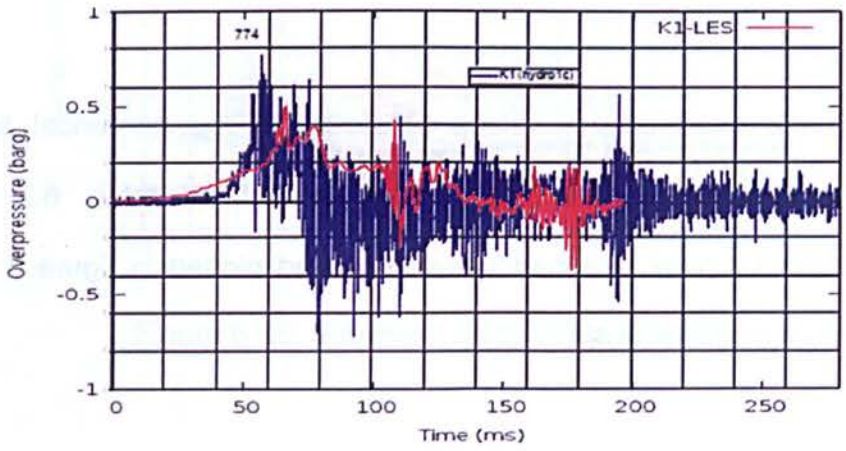

Figure 6.37. Pressure trace curve at K1

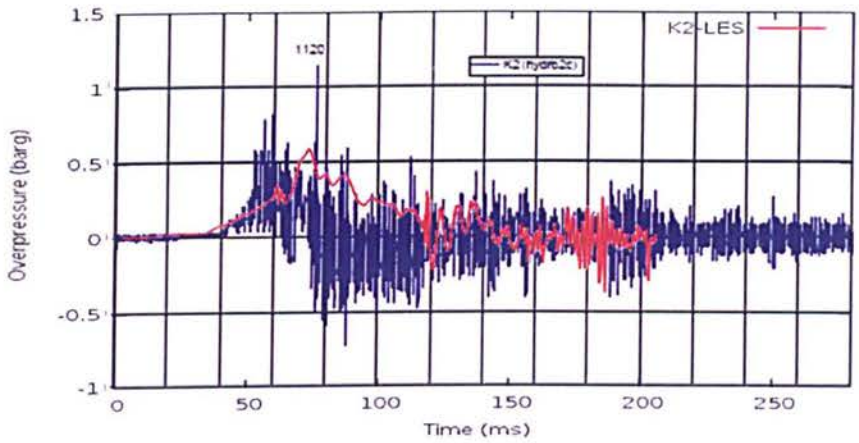

Figure 6.38. Pressure trace curve at K2

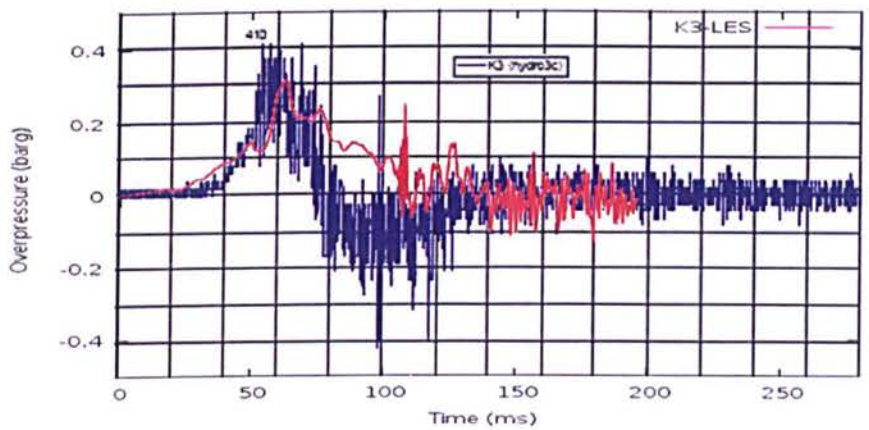

Figure 6.39. Pressure trace curve at K3

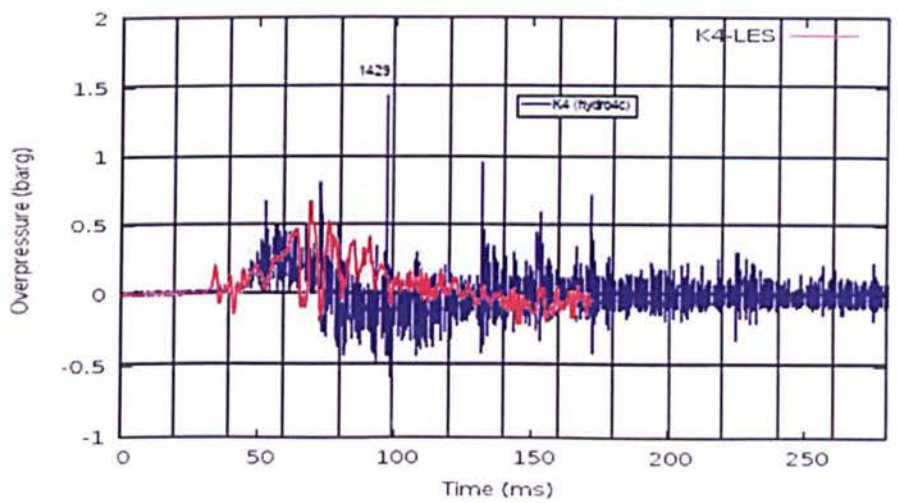

Figure 6.40. Pressure trace curve at K4

The numerical pressure trace curves at the monitoring points within the premixed cloud are shown in figure 6.37 to 6.40. It can be discerned from the pressure trace plots that the fluctuations in the pressure field are very high within the premixed cloud. The high fluctuations in the pressures field could be because of multiple reflections within the congestion of hydrogen storages cylinders. The instant peak pressure values for less than < 1ms obtained in experiments are not predicted in the numerical simulations.

b) Monitoring points outside congestion (opp. High wall)

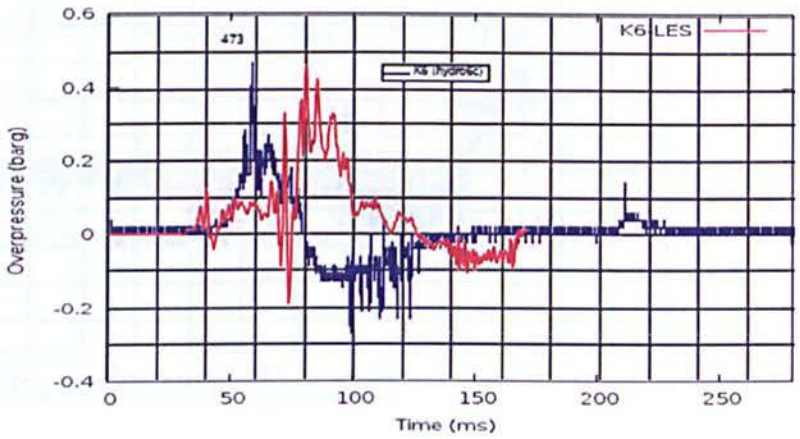

Figure 6.41. Pressure trace curve at K6

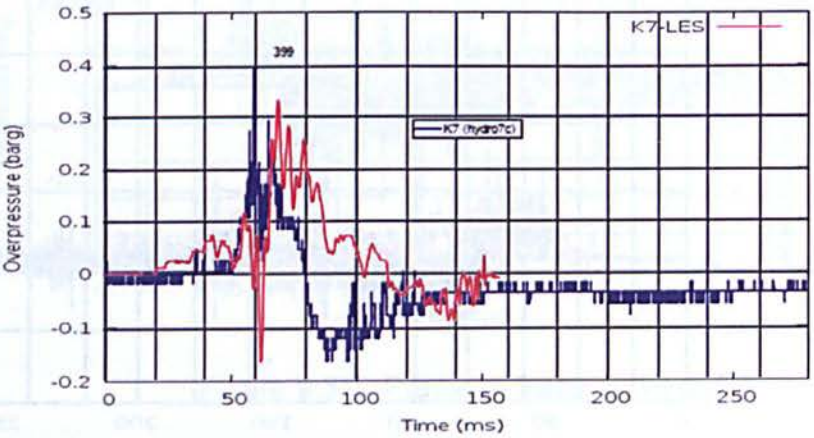

Figure 6.42. Pressure trace curve at K7

The numerical pressure trace curves at the monitoring points outside the premixed cloud and opposite in direction to high rise wall are shown in figure 6.41 and 6.42. Pressure traces are comparatively becoming less fluctuating outside the vapour cloud.

c) Monitoring points outside congestion (opp. Low wall)

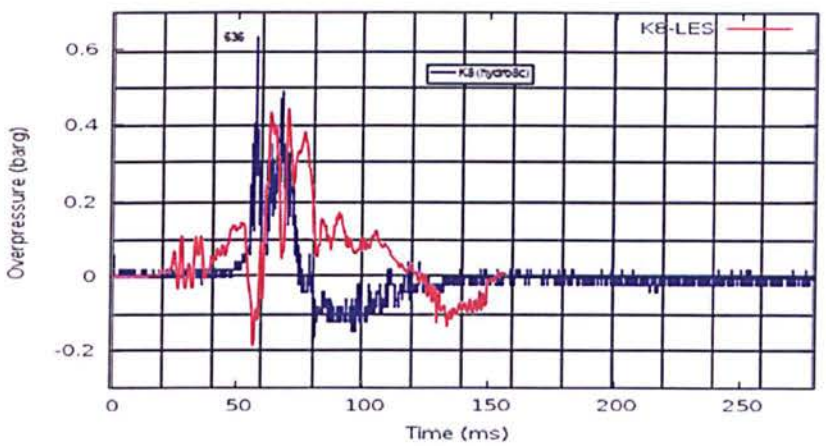

Figure 6.43. Pressure trace curve at K8

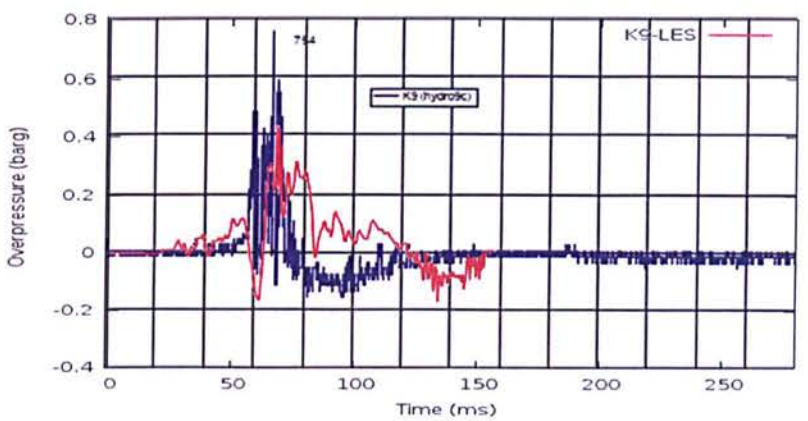

Figure 6.44. Pressure trace curve at K9

The numerical pressure trace curves at the monitoring points outside the premixed cloud and opposite in direction to low raise wall are shown in figure 6.43 and 6.44. The occurrence of the negative pressure phase is numerical results is delayed as compared to experiments. Overall the numerical predictions satisfactorily trace the experimental results.

d) Monitoring points on the High wall

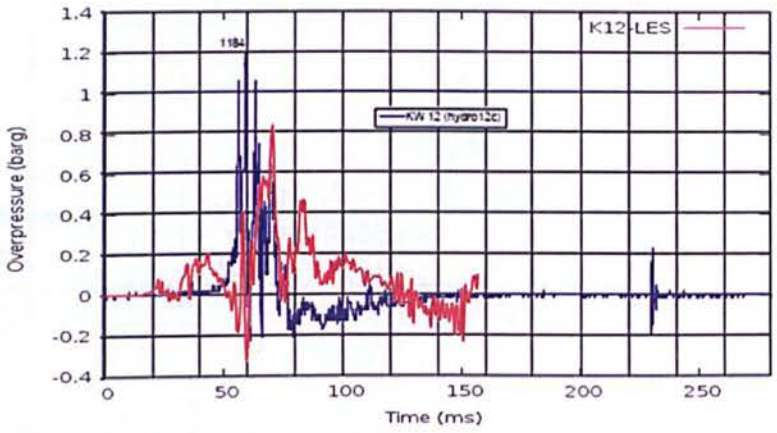

Figure 6.45. Pressure trace curve at K12

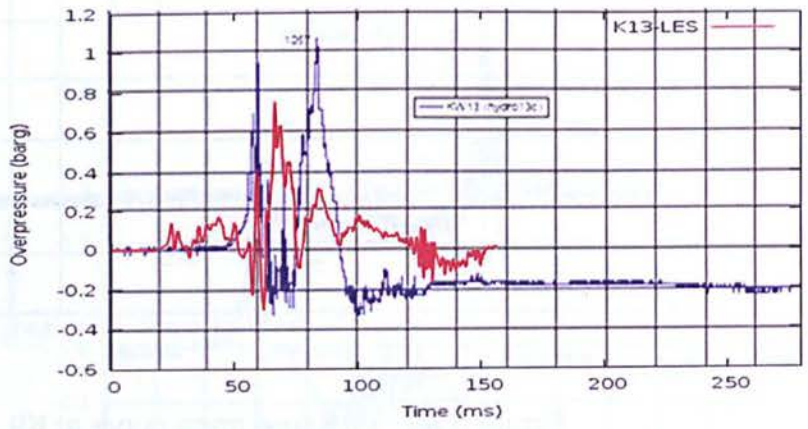

Figure 6.46. Pressure trace curve at K13

The numerical pressure trace curves at the monitoring points on the high rise wall are shown in figure 6.45 and 6.46. Pressure traces are having low fluctuations levels similar to that obtained outside the premixed cloud. The instant peak pressure values for less than < 1ms obtained in experiments are not predicted in the numerical simulations. Whereas the trends of rise in overpressures wave is well predicted in numerical results.

S. no.	Sensor (Monitoring points)	Distance (m)	Expt. (barg)	Numerical (barg)
From High Wall				
1	K1	1.8	0.51	0.50
2	K2	2.7	0.43	0.59
3	K3	3.6	0.36	0.32
4	K4	4.5	0.40	0.67
5	K5	5.4	0.43	0.51
6	K6	6.5	0.42	0.46
7	K7	7.5	0.30	0.33
From Low wall				
8	K8	5.74	0.49	0.44
9	K9	6.74	0.54	0.43
Up wall from ground				
10	K12	1.5	1.11	0.84
11	K13	2.7	1.04	0.75

Table 6.4. Overpressure comparison at respective monitoring points

The peak overpressure values predicted in the numerical simulation at various monitoring points are summarized in table 6.4 along with experimental peak overpressure values and plotted in figure 6.47 for away from high wall direction.

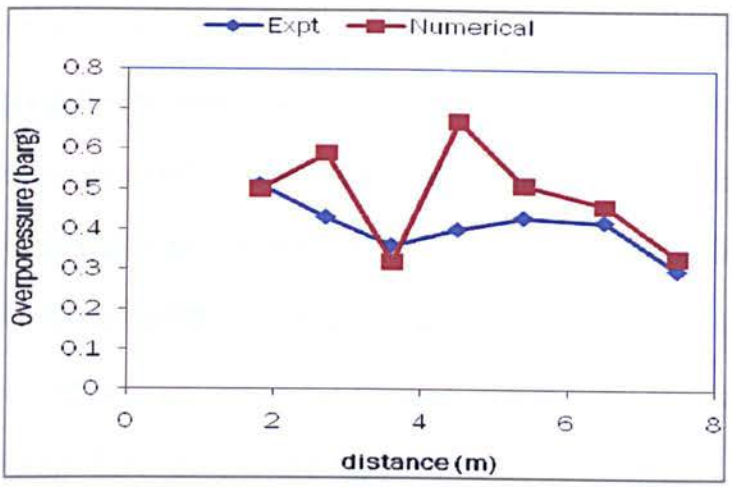

Figure 6.47. Overpressure comparison (distance away from High wall)

6.4.5. Conclusion

The large eddy simulations of turbulent flame deflagrations in hydrogen cylinder storage facility engulfed in the fuel-air vapour cloud at equivalence ratio 1.2 are carried out using CFM-LES solver with wall interactions. Two experiments scenarios of different ignition locations are considered in the present study, Case A – location (P1) close to high wall and another Case B- location (P4) close to low wall. Within the congestion the numerical predicted the high fluctuations in the pressure field due to multiple reflections with the obstacles. The instantaneous peaks in the overpressure (< 1 ms) are not predicted in the numerical simulations but overall the trend in the pressure trace curves is quite similar to that of the experiments. From the pressure trace plots within the congestion, it can be inferred that the overpressure generated inside the cylinder storage congestion were very frequent and instantaneous. Outside the congestion (after 6 m distance from the high wall) the overpressure trends are less fluctuating and comparatively smooth in profile. The overall peak overpressure plotted in the distance away from High

wall at respective monitoring points for the two experimental scenarios are shown in figures 6.36 & 6.47, show good match outside the congestion. Large eddy simulations well predicted the unsteadiness in the pressure field and also the CFM-LES model along with wall interaction performed well in predicting the overpressures of large scale turbulent deflagrations.

Chapter 7

CONCLUSION AND FUTURE WORK

7.1 Conclusion

The primary goal of this thesis was to develop an improved premixed combustion modeling for numerical simulation of turbulent deflagrations in confinements has been achieved. The numerical solver was developed in open source CFD toolkit - OpenFOAM based on Coherent Flame Model in the context of large eddy simulations. Turbulence and occurrence of instabilities due to heat release, hydrodynamic flow fields and acoustics are well predicted by large eddy simulations method. LES approach of resolving large scale motions and model small scales is proving to be very promising technique for simulating reacting flow.

The turbulent flow governing equations, numerics and the boundary conditions together defining the CFD solver are validated by simulating a well known LES test case : the turbulent channel flow case, based on DNS work of (Kim et al., 1987). The LES compressible channel flow results are compared with the incompressible DNS channel flow results under Morkovin hypothesis. This hypothesis suggest that the compressible turbulent boundary layer essentially follow incompressible turbulent boundary layer when the free stream Mach number is less than or equal to 5. Good match of density weighted LES results with the DNS results validated the numerical solvers functioning in OpenFOAM.

Coherent Flame Model is adopted with transport equation closure for simulating turbulent deflagrations. Coherent flame model has been widely used in RANS and extended to LES, is particularly attractive as the modeling parameters - Flame Surface Density and laminar flame speed are physically well defined quantities which can be extracted from DNS or experiments. The balanced FDS transport equation can cater to non-equilibrium nature of source terms which are true in complex geometry flows thereby improve predictions of flame propagations.

In the near wall modeling emphasis was to capture the proper flame behaviour i.e. quenching and acceleration close to the obstacles/solid surfaces. Additional models namely, Flame-wall and Flow-wall interactions are adopted in the present study to improve the numerical predictions of CFM-LES in the near wall region.

The Flow-wall interaction is modelled based on the improvements in wall layer model proposed by (Duprat et al., 2011). The model is based on the simplified thin-boundary-layer equations and on extension of turbulent viscosity coefficient originally proposed by (Balaras et al., 1996). The inner scaling is extended to take into account both wall shear stress and streamwise pressure gradient. The model implementation in OpenFOAM is verified by simulating the flow in a periodic hill obstructed channel. The results clearly demonstrated the importance of taking into accounts both streamwise pressure gradient and shear stresses in the wall modeling. The Flow-wall interaction modeling is able to reproduce flow separation zones even when very coarse grids are considered. In particular the inclusion of streamwise

pressure gradient in near wall velocity scaling has considerably improved the model predictions for flows with adverse pressure gradients.

The flame-wall interactions were adopted in LES context, based on RANS analysis of flame surface density by (Bruneaux et al., 1997). The CFM-LES governing equations are modified in the near-wall region to capture the turbulent flame-wall interactions. The modifications have incorporated changes for laminar flame speed, annihilation and propagation through a flame quenching factor which is a function of enthalpy loss, heat release factor & reduced activation energy, and changes in turbulent length scales using van-Driest damping coefficient for viscosity. A non-isobaric enthalpy loss factor was been adopted in the present study to delimit the near wall flame influenced zone. Finally a posteriori test of 'V'-flame stabilized in a channel flow based on DNS results of (Gruber et al., 2010) is analyzed to establish the two flame-wall interaction model constants. In particularly, the flame displacement speed and the wall heat flux of DNS results were matched in the LES simulations and model constants were assigned the values of γ_q = 15, and γ_d = 0.3 respectively.

The simulations of flame quenching in a quench mesh, turbulent flame deflagration in a repeated obstructed channel and a large scale deflagration in hydrogen storage facility were carried out using the CFM-LES along with Flow-wall and Flame-wall interactions to demonstrate the intended modeling improvements. The different test cases clearly validated the developed solver capabilities and conclude that the CFM-LES along with wall interaction models is able to improve the numerical prediction of flame propagations.

This also predicts the proper flame behaviour i.e. quenching and acceleration close to the obstacles/solid surfaces.

7.2 Future work

The Coherent Flame Model adopted in the present study is formulated assuming unity Lewis number. It's a known fact that the unity Lewis number formulation of combustion governing equation is not able to capture the influence of flame stretch on the flame front. Thus one of the possible extensions of this work would be to extend the present numerical solver to non-unity Lewis number formulation. This will also improve the numerical prediction considering the change in the fuel properties.

The model constants proposed for the Flame-wall interaction were tested for the low Reynolds numbers flows. It would be interesting to validate these model constants for high Reynolds number flows which are unavailable in the literature.

The combustion process in gas turbines and internal combustion engines is very much influenced by wall effects. Hence it will be interesting to assess the numerical predictions using the improved combustion model for hydrocarbon fuels. Therefore a more natural extension of the present research work will be to ascertain the Flame-wall model constants for most of the working fuels.

The applicability of these models will further increase by extending them to partially premixed combustion regime, so that both premixed and non-premixed modes of combustion flow problems can also be numerically simulated extending the usage of the present developed solver.

Appendix A

LAMINAR FLAME-WALL INTERACTION

A laminar flame wall interaction is simulated in a one-dimensional domain of size 2cm x 2cm (shown in figure A-1) using detailed hydrogen-air reaction mechanism by (Li et al., 2004), consisting of 9 species and 19 step reactions at equivalence ratio 1.5. The purpose of this laminar flame-wall interaction study is to provide laminar reference values to normalize the turbulent flame-wall interactions. In head-on quenching configuration, a planar laminar flame propagates towards the wall at a normal angle to the the solid surface. An open non-reflecting boundary is placed on three side of the domain with remaining one side as wall boundary. The domain is discretized into 10 micron size uniform grid, which is sufficient to resolve the flame structure with more than ten grid points within the flame front.

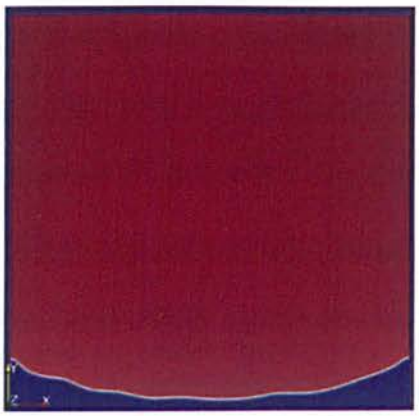

Figure A-1. Simulation 1D domain (bottom face is wall and remaining sides are open boundary)

Temperature, heat release and mass fraction plots are averaged flow quantities in the homogenous direction. The simulations are carried out at two wall temperatures: first one at which the laminar flame speed is more precisely known T=300K and second at an elevated temperature T=750 K to normalize the turbulent flame wall simulation results in chapter 5.

Case A : Isothermal wall temperature = 300 K

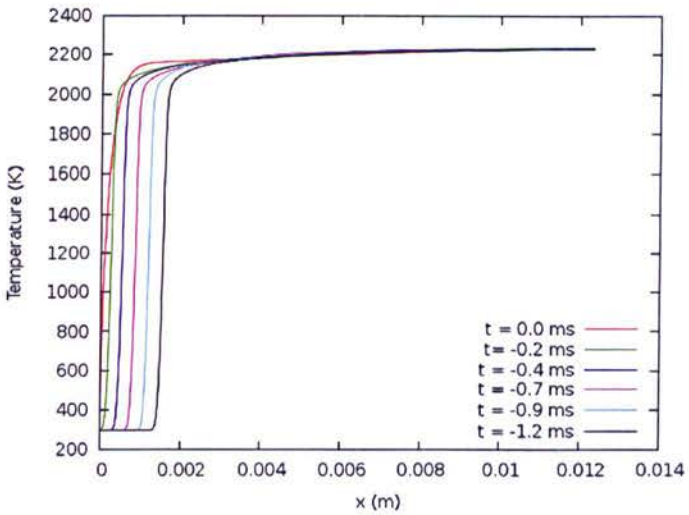

Figure A-2. Temperature plot in time sequence

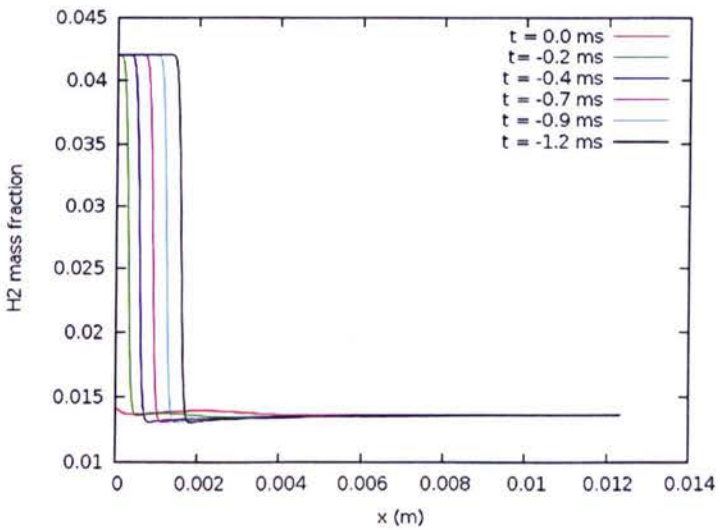

Figure A-3. H_2 mass fraction plot in time sequence

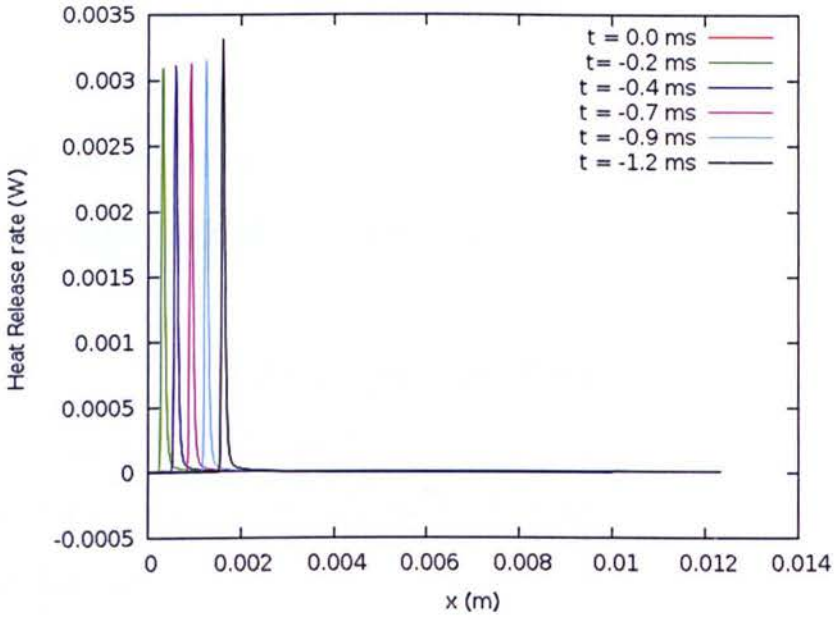

Figure A-4. Heat release rate plot in time sequence

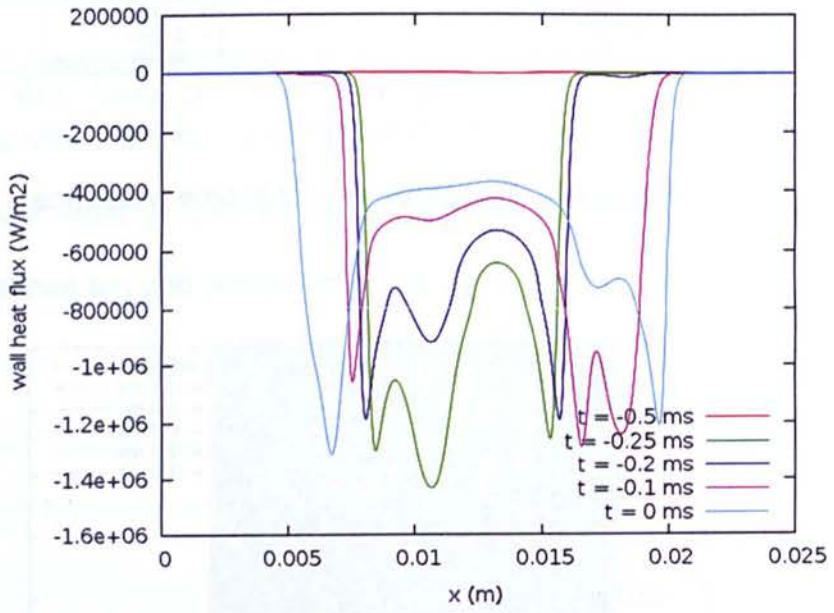

Figure A-5. Wall heat flux plot in time sequence at T_{wall} = 300 K

(peak value – green curve) .

Case B: Isothermal wall temperature = 750 K

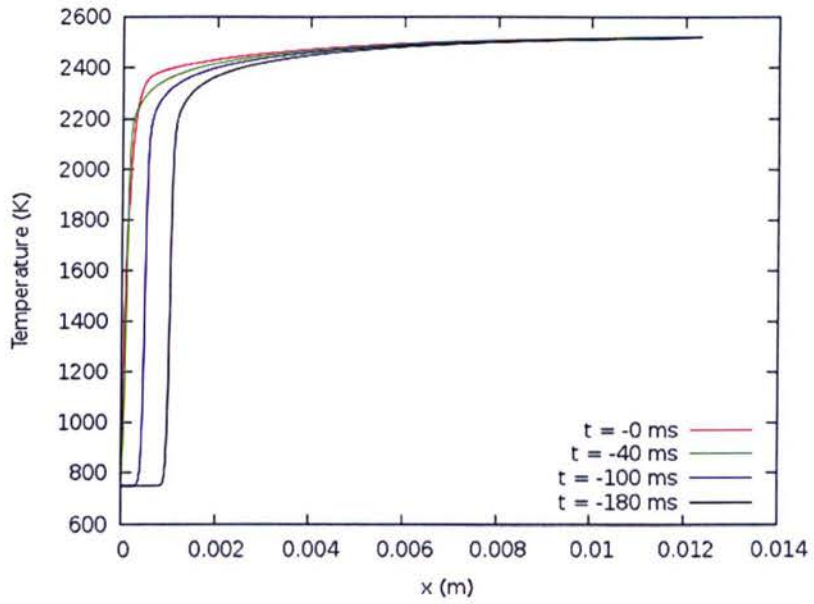

Figure A-6. Temperature plot in time sequence

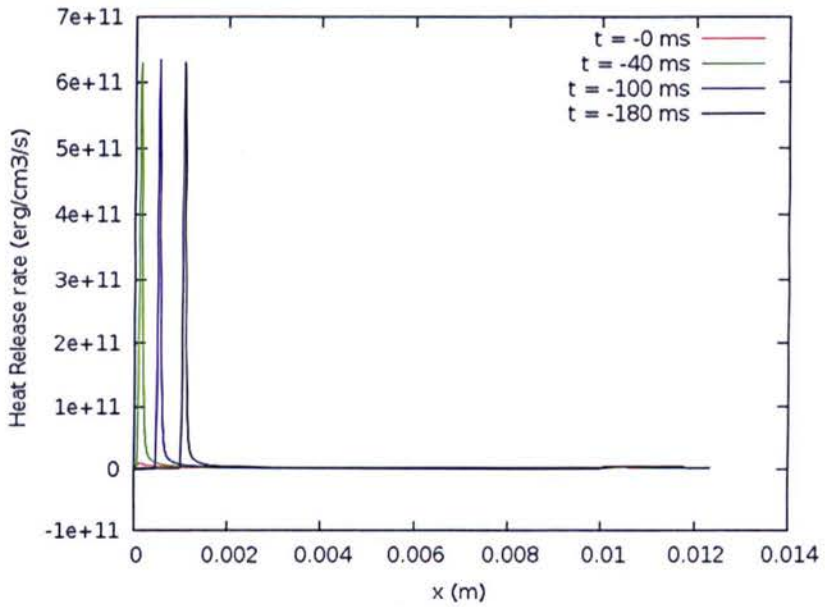

Figure A-7. Heat release rate plot in time sequence

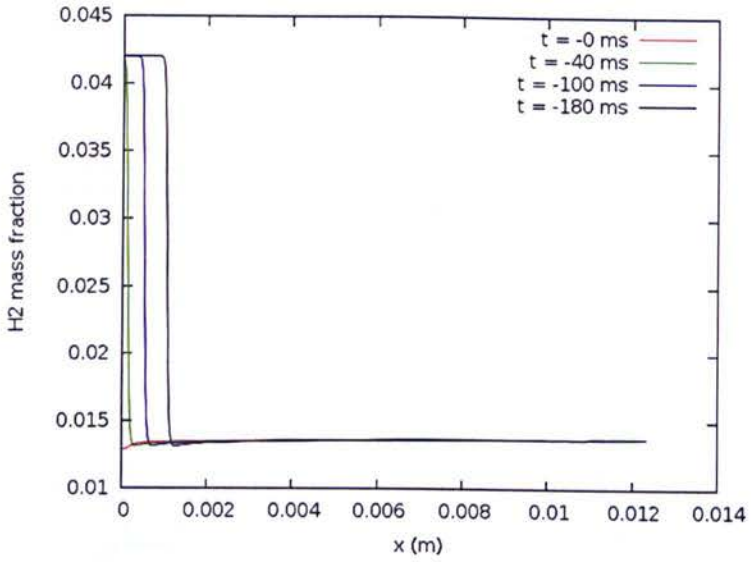

Figure A-8. H_2 mass fraction plot in time sequence

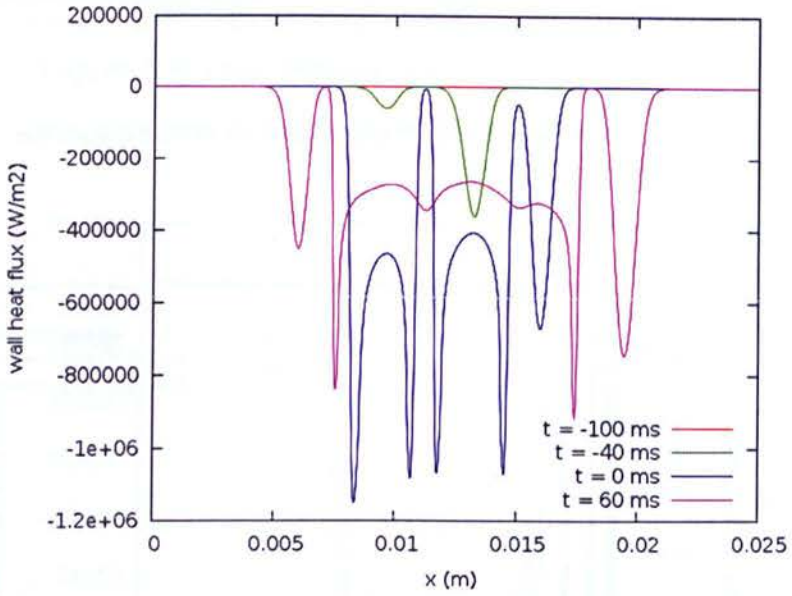

Figure A-9. Wall heat flux plot in time sequence at T_{wall} = 750 K (peak value – blue curve).

Figure A-10, are the time sequence plots for the laminar flame approaching the isothermal wall in Head-on flame-wall interaction at four different instance of time. The time at which the flame is completely quenched is set to reference value of zero.

(a) Heat release rate

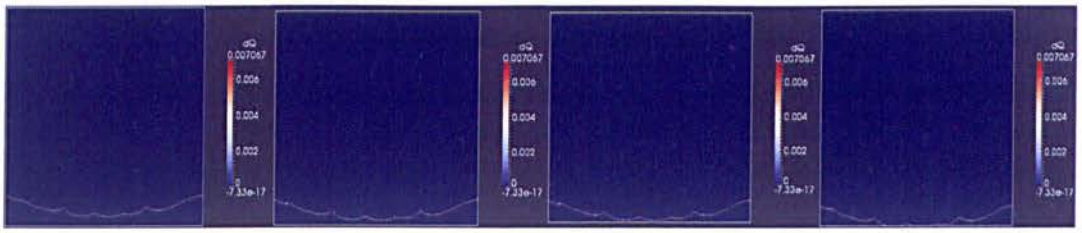

(i) at t = - 180 ms (ii) at t = - 100 ms (iii) at t = - 40 ms (iv) at t = 0 ms

(b) H_2 mass fraction

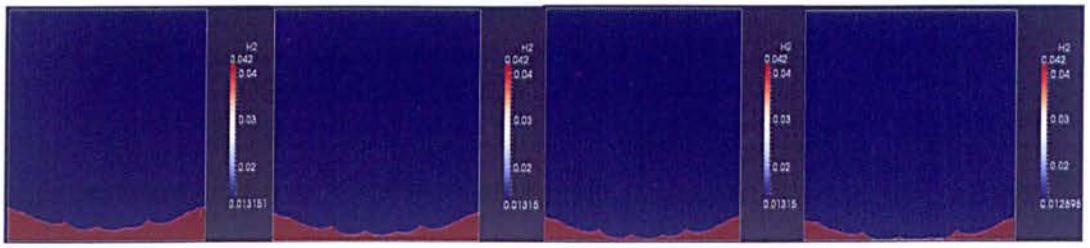

(i) at t = - 180 ms (ii) at t = - 100 ms (iii) at t = - 40 ms (iv) at t = 0 ms

(c) O_2 mass fraction

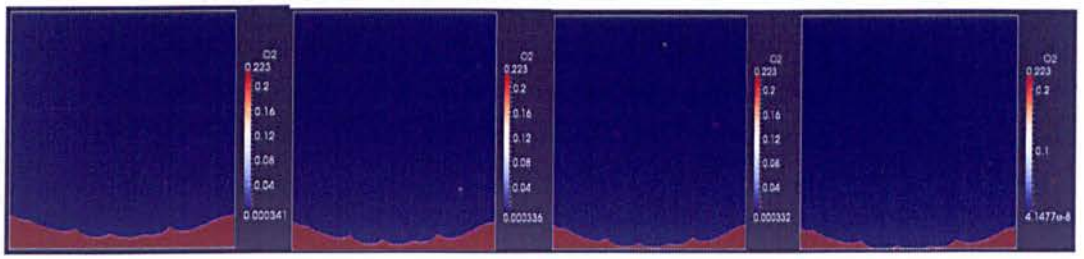

(i) at t = - 180 ms (ii) at t = - 100 ms (iii) at t = - 40 ms (iv) at t = 0 ms

(d) Temperature plot

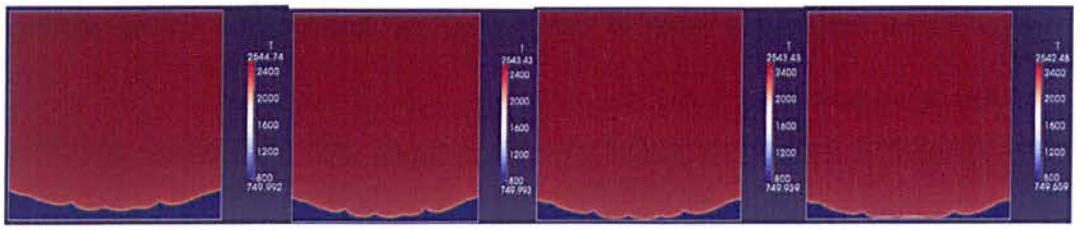

(i) at t = - 180 ms (ii) at t = - 100 ms (iii) at t = - 40 ms (iv) at t = 0 ms

Figure A-10. Time sequence of flame approaching isothermal wall

The laminar peak wall heat flux is used to normalize the turbulent wall heat flux in posteriori test (section 5.4). The normalized value is indicative of turbulence contribution in increasing the wall heat flux values. The peak average wall heat flux in case A & case B is found to be 1.22 MW/m^2 and 1.0 MW/m^2 respectively (figure A-5 & A-9).

Laminar Flame speed

The laminar flame speed can be estimated by power law correlations proposed by previous author, but they tend to provide cluster of values with no two values converging to each other. At first the computation method of extracting the laminar flame speed from 1D result is verified at the known conditions i.e. at 300K and then similar method was used to obtain results at elevated temperature of 750 K. Laminar flame speed is evaluated using the following equations

$$\rho_1 C_p S_l (T_2 - T_1) = -Q \int_{-l}^{+l} \dot{\omega}_F dx \qquad \text{(A-1)}$$

$$S_l = -\frac{Q \int_{-l}^{+l} \dot{\omega}_F dx}{\rho_1 C_p (T_2 - T_1)} \qquad \text{(A-2)}$$

The flame approach time is readjusted by setting the flame quenching instance all wall to t = 0 s.

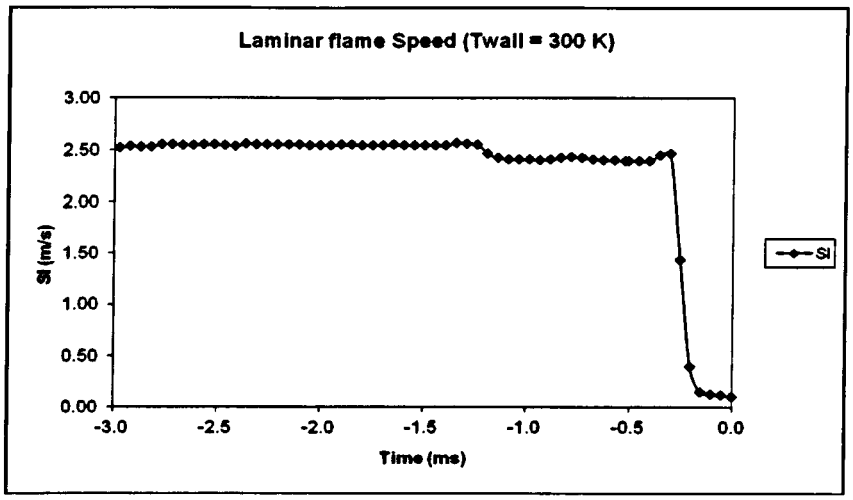

Figure A-11. Laminar flame speed with wall temperature 300 K

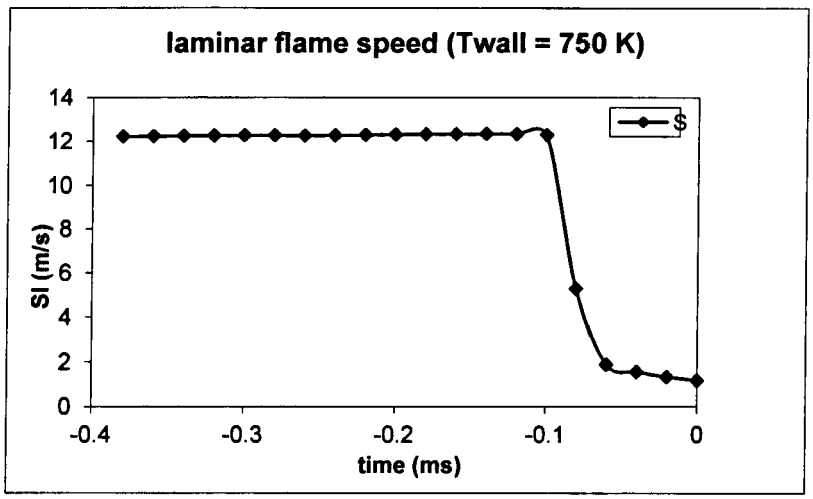

Figure A-12. Laminar flame speed with wall temperature 750 k

From the figure A-11 and figure A-12, it can be inferred that, initially the flame propagates freely undisturbed in region away from the wall. However, when the flame–wall distance becomes smaller than approximately ten times the flame thickness, the flame is affected by the presence of the wall, it start to decelerate and becomes increasingly thinner until quenching occurs at a

flame–wall distance of approximately two flame thicknesses. The quenching process involves a tenfold increase in the overall flame heat release rate (figure A-5 & A-11) due to the zero-activation-energy, exothermic, radical recombination reactions occur at the 'cold' wall surfaces. The laminar flame speed during quenching is found to be reducing exponentially, similar conclusion were also drawn in (Wichman and Bruneaux, 1995).

Appendix B

The digital filter method

The step by step procedure for generating turbulent inflow conditions using digital filter approach based on (Xie and Castro, 2008) for channel flow homogenous in streamwise direction are mentioned below. The streamwise direction is assumed to be along Cartesian x-direction, wall normal is y-direction and spanwise in z-direction respectively. Prerequisite information are the integral length scales (L_x, L_y, L_z) at the inlet plane and the Reynolds stress tensor (R_{ij}).

1) Based on the vertical (L_y) and lateral (L_z) integral length scale, the size of the filter are computed as, $N_y = 2L_y/\Delta y$, $N_z = 2L_z/\Delta z$ and the temporal filter size in the streamwise direction is computed as $N_x = 2L_x/U_x$, where U_x is x component of mean velocity.

2) Calculation of the filter coefficient $b_{jk} = b_j \times b_k$ with,

$$b_k = \frac{\exp\ -\pi|k|/N}{\sqrt{\sum_{j=-N}^{N} \exp\ -\pi|k|/N\ ^2}}, \qquad \text{(B.1)}$$

3) Computation of the amplification tensor $[a_{ij}]$ is shown in equation B.2 using the prescribed Reynolds stress tensor components (R_{ij}). Details on the derivation of this amplitude tensor can be found in (Lund et al., 1998).

$$[a_{ij}]=\begin{bmatrix} \sqrt{R_{11}} & 0 & 0 \\ R_{21}/a_{11} & \sqrt{R_{22}-a_{21}^2} & 0 \\ 0 & 0 & \sqrt{R_{33}} \end{bmatrix} \quad \text{(B.2)}$$

4) Generation of set of random numbers (r_k) of dimension p = ($2N_y$ + M_y) x ($2N_z$ + M_z) with zero-mean ($\overline{r_k}=\sum_{k=1}^{p} r_k/p=0$) and unit-variance ($\overline{r_k r_k}=\sum_{k=1}^{p} r_k^2/p=1$) is done, where M_y and M_z are the total grid dimensions in the y and z coordinate directions respectively. Box-Muller theorem is used of generating these random number sets. (If *a* and *b* are set of two independent numbers uniformly distributed in (0,1], then combining them as, $c=\sqrt{-2\ln(a)}*\cos(2\pi b)$ and $d=\sqrt{-2\ln(a)}*\sin(2\pi b)$, will give *c* and *d* as two independent number sets from the normal distribution with unit standard deviation).

5) Apply the discrete filter operation to the random numbers (r_k),

$$\upsilon_\alpha(t,y,z)_{\alpha=1,2,3}=\sum_{j'=-N_y}^{N_y}\sum_{k'=N_z}^{N_z} b_{j'k'} r_{\alpha,j+j',k+k'} \quad \text{(B.3)}$$

6) Correlating the newly computed υ_α field with previous time step υ_α^{old} field, enforcing the two point correlation and also the streamwise auto-correlation,

$$\rho_{\alpha=1,2,3}=\upsilon_\alpha^{old}\exp\left(\frac{-\pi\Delta t}{2\tau}\right)+\upsilon_\alpha\sqrt{1-\exp\left(\frac{-\pi\Delta t}{\tau}\right)} \quad \text{(B.4)}$$

where, $\tau=\frac{L_x}{U_x}$ is longitudinal lagrangian time scale, L_x is prescribed longitudinal integral length scale, U_x is the mean streamwise velocity profile.

7) Finally the velocity field at time ' t ' is computed as,

$$u_\alpha(0,y,z,t)_{|k=1,2,3}=[<u_\alpha(0,y,z,t)>]_{|\alpha=1,2,3}+[a_{ij}][\rho_\alpha]_{|\alpha=1,2,3} \quad \text{(B.5)}$$

where $[<u_\alpha(0,y,z,t)>]$ is mean velocity and hence $u'=[a_{ij}][\rho_\alpha]_{|\alpha=1,2,3}$.

8) For consecutive time steps, process is iterated from steps 4 to step 7, resulting in generation of time and spatial dependent velocity field at the inflow plane. For the remaining flow variables, the pressure (P) is assumed uniform at the inlet boundary and temperature (T) is approximated assuming strong Reynolds Analogy (Touber and Sandham, 2009)

$$\frac{T'}{\overline{T}}=-(\gamma-1)Ma^2\frac{u'}{U} \quad \text{(B.6)}$$

where, Ma is Mach number, u' is velocity fluctuations computed from the digital filter method and U is mean flow velocity.

The synthetic boundary condition specified at the inlet boundary requires an additional length of domain downstream of the inlet to develop realistic turbulence. Hence this makes the channel length longer in the streamwise direction than the actual required channel dimensions.

The integral length scales (L_x, L_y, L_z) computed by integrating the two-point correlation curves for the turbulent channel flow at Re_t =180 (discussed in section 2.4) are shown in Figure B1 along half channel height. The Integral

length scales results are curve fitted and non dimensionalised using Half channel height (H).

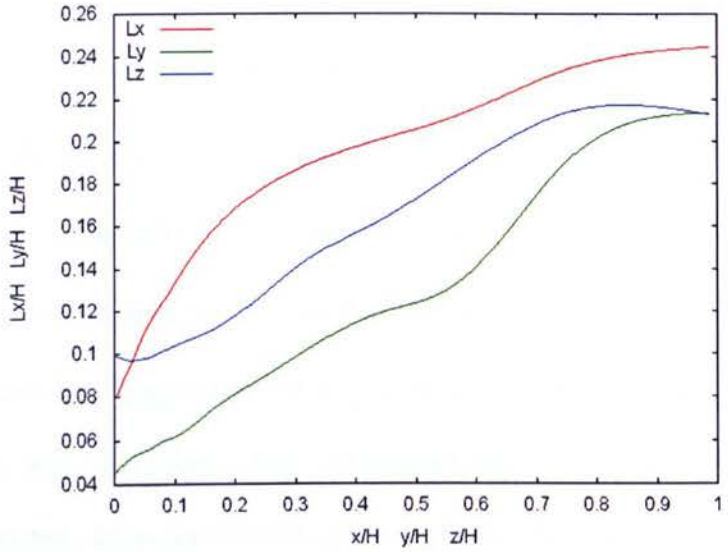

Figure B1. Integral length scale along half channel height for turbulent channel flow at Re_t =180.

Bibliography

ABDEL-GAYED, R. G., BRADLEY, D. & LUNG, F. K. K. 1989. Combustion regimes and the straining of turbulent premixed flames. *Combustion and Flame,* 76, 213-218.

ALMEIDA, G. P., DURAO, D. F. G. & HEITOR, M. V. 1993. Wake flows behind two-dimensional model hills. *Experimental Thermal and Fluid Science,* 7, 87-101.

ALSHAALAN, T. & RUTLAND, C. J. 2002. Wall heat flux in turbulent premixed reacting flow. *Combustion Science and Technology,* 174, 135-165.

ALSHAALAN, T. M. & RUTLAND, C. J. 1998. Turbulence, scalar transport, and reaction rates in flame-wall interaction. *Symposium (International) on Combustion,* 27, 793-799.

ANDRAE, J., BJÖRNBOM, P., EDSBERG, L. & ERIKSSON, L.-E. 2002. A numerical study of side wall quenching with propane/air flames. *Proceedings of the Combustion Institute,* 29, 789-795.

ANGELBERGER, C., POINSOT, T. J. & DELHAYE, B. 1997. Improving Near-Wall Combustion and Wall Heat Transfer Modeling in SI Engine Computations. *Int. Fall Fuels & Lub. Meeting & Exposition.* Tulsa: SAE Paper

BABA-AHMADI, M. H. & TABOR, G. 2009. Inlet conditions for LES using mapping and feedback control. *Computers & Fluids,* 38, 1299-1311.

BALARAS, E., BENOCCI, C. & PIOMELLI, U. 1996. Two-layer approximate boundary conditions for large-eddy simulations. *AIAA Journal,* 34, 1111-1119.

BALLAL, D. R. & LEFEBVRE, A. H. 1977. Flame quenching in turbulent flowing gaseous mixtures. *Symposium (International) on Combustion,* 16, 1689-1698.

BELL, J. B., ASPDEN, A. J., DAY, M. S. & LIJEWSKI, M. J. 2007. Numerical simulation of low Mach number reacting flows. *Journal of Physics: Conference Series,* 78, 012004.

BELLENOUE, M., KAGEYAMA, T., LABUDA, S. A. & SOTTON, J. 2003. Direct measurement of laminar flame quenching distance in a closed vessel. *Experimental Thermal and Fluid Science,* 27, 323-331.

BERSELLI, L. C., ILIESCU, T. & LAYTON, W. J. 2006. *Mathematics of Large Eddy Simulation of Turbulent Flows* Springer; 2006 edition.

BJERKETVEDT, D., BAKKE, J. R. & VAN WINGERDEN, K. 1997. Gas explosion handbook. *Journal of Hazardous Materials,* 52, 1-150.

BLINT, R. J. 1986. The Relationship of the Laminar Flame Width to Flame Speed. *Combustion Science and Technology,* 49, 79-92.

BOGER, M., VEYNANTE, D., BOUGHANEM, H. & TROUVÉ, A. 1998. Direct numerical simulation analysis of flame surface density concept for large eddy simulation of turbulent premixed combustion. *Symposium (International) on Combustion,* 27, 917-925.

BORGHI, R. 1985. On the structure and morphology of turbulent premixed flames. *Recent Advances in the Aerospace Sciences.*

BOUST, B., BERNARD, L., SOTTON, J., LABUDA, S. A. & BELLENOUE, M. 2009. A model of flame quenching in non-isothermal initial condition. *Proceedings of the European Combustion Meeting*

BOUST, B., SOTTON, J., LABUDA, S. A. & BELLENOUE, M. 2007. A thermal formulation for single-wall quenching of transient laminar flames. *Combustion and Flame,* 149, 286-294.

BRADSHAW, P. 1974. The effect of mean compression or dilatation on the turbulence structure of supersonic boundary layers. *Journal of Fluid Mechanics,* 63, 449-464.

BRADSHAW, P. 1985. *An Introduction to Turbulence and Its Measurement,* Pergamon.

BRAY, K. N. C. 1980. Turbulent fkows with premixed reactants in turbulent flows. *Topics in applied physics.*

BREUER, M., KNIAZEV, B. & ABEL, M. 2007. Development of wall models for LES of separated flows using statistical evaluations. *Computers & Fluids,* 36, 817-837.

BRUN, C., PETROVAN BOIARCIUC, M., HABERKORN, M. & COMTE, P. 2008. Large eddy simulation of compressible channel flow. *Theoretical and Computational Fluid Dynamics,* 22, 189-212.

BRUNEAUX, G., AKSELVOLL, K., POINSOT, T. & FERZIGER, J. H. 1996. Flame-wall interaction simulation in a turbulent channel flow. *Combustion and Flame,* 107, 27-44.

BRUNEAUX, G., POINSOT, T. & FERZIGER, J. H. 1997. Premixed flame–wall interaction in a turbulent channel flow: budget for the flame surface density evolution equation and modelling. *Journal of Fluid Mechanics,* 349, 191-219.

BUTLER, T. D. & O'ROURKE, P. J. 1977. A numerical method for two dimensional unsteady reacting flows. *Symposium (International) on Combustion,* 16, 1503-1515.

CABOT, W. & MOIN, P. 2000. Approximate Wall Boundary Conditions in the Large-Eddy Simulation of High Reynolds Number Flow. *Flow, Turbulence and Combustion,* 63, 269-291.

CANDEL, S. M. & POINSOT, T. J. 1990. Flame Stretch and the Balance Equation for the Flame Area. *Combustion Science and Technology,* 70, 1-15.

CANT, R. S. & BRAY, K. N. C. 1989. Strained laminar flamelet calculations of premixed turbulent combustion in a closed vessel. *Symposium (International) on Combustion,* 22, 791-799.

CHAKRABORTY, N. & CANT, R. S. 2006. Influence of Lewis number on strain rate effects in turbulent premixed flame propagation. *International Journal of Heat and Mass Transfer,* 49, 2158-2172.

CHAKRABORTY, N. & CANT, R. S. 2009. Effects of Lewis number on turbulent scalar transport and its modelling in turbulent premixed flames. *Combustion and Flame,* 156, 1427-1444.

CHAPMAN, D. K. 1979. Computatisnal Aerodynamics Development and Outlook. *AIAA Journal,* 17, 1293-1313.

CHARLETTE, F., MENEVEAU, C. & VEYNANTE, D. 2002a. A power-law flame wrinkling model for LES of premixed turbulent combustion Part I: non-dynamic formulation and initial tests. *Combustion and Flame,* 131, 159-180.

CHARLETTE, F., MENEVEAU, C. & VEYNANTE, D. 2002b. A power-law flame wrinkling model for LES of premixed turbulent combustion Part II: dynamic formulation. *Combustion and Flame,* 131, 181-197.

CHOI, H. & MOIN, P. 2012. Grid-point requirements for large eddy simulation: Chapman's estimates revisited. *Physics of Fluids,* 24, 011702-5.

CHOI, Y. H. & MERKLE, C. L. 1993. The Application of Preconditioning in Viscous Flows. *Journal of Computational Physics,* 105, 207-223.

CHOMIAK, J. & JAROSIŃSKI, J. 1982. Flame quenching by turbulence. *Combustion and Flame,* 48, 241-249.

CICCARELLI, G., JOHANSEN, C. T. & PARRAVANI, M. 2010. The role of shock–flame interactions on flame acceleration in an obstacle laden channel. *Combustion and Flame,* 157, 2125-2136.

COLEMAN, G. N., KIM, J. & MOSER, R. D. 1995. A numerical study of turbulent supersonic isothermal-wall channel flow. *Journal of Fluid Mechanics,* 305, 159-183.

COLIN, O., DUCROS, F., VEYNANTE, D. & POINSOT, T. 2000. A thickened flame model for large eddy simulations of turbulent premixed combustion. *Physics of Fluids,* 12, 1843-1863.

DAHOE, A. E. 2005. Laminar burning velocities of hydrogen–air mixtures from closed vessel gas explosions. *Journal of Loss Prevention in the Process Industries,* 18, 152-166.

DEARDORFF, J. W. 1970. A numerical study of three-dimensional turbulent channel flow at large Reynolds numbers. *Journal of Fluid Mechanics,* 41, 453-480.

DUCLOS, J. M., VEYNANTE, D. & POINSOT, T. 1993. A comparison of flamelet models for premixed turbulent combustion. *Combustion and Flame,* 95, 101-117.

DUPRAT, C., BALARAC, G., METAIS, O., CONGEDO, P. M. & BRUGIERE, O. 2011. A wall-layer model for large-eddy simulations of turbulent flows with/out pressure gradient. *Physics of Fluids,* 23, 015101-12.

ERCOFTAC & DATABASE. http://cfd.mace.manchester.ac.uk/ercoftac/ [Online]. [Accessed].

EZEKOYE, O., GREIF, R. & SAWYER, R. F. 1992. Increased surface temperature effects on wall heat transfer during unsteady flame quenching. *Symposium (International) on Combustion,* 24, 1465-1472.

FROHLICH, J., MELLEN, C. P., RODI, W., TEMMERMAN, L. & LESCHZINER, M. A. 2005. Highly resolved large-eddy simulation of separated flow in a channel with streamwise periodic constrictions. *Journal of Fluid Mechanics,* 526, 19-66.

FUREBY, C., TABOR, G., WELLER, H. G. & GOSMAN, A. D. 1997. A comparative study of subgrid scale models in homogeneous isotropic turbulence. *Physics of Fluids,* 9, 1416-1429.

GEURTS, B. 2003. *Elements of direct and large-eddy simulation,* Philadelphia, PA, R.T. Edwards.

GREENBERG, J. B. & RONNEY, P. D. 1993. Analysis of Lewis number effects in flame spread. *International Journal of Heat and Mass Transfer,* 36, 315-323.

GRUBER, A., SANKARAN, R., HAWKES, E. R. & CHEN, J. H. 2010. Turbulent flame–wall interaction: a direct numerical simulation study. *Journal of Fluid Mechanics,* 658, 5-32.

GÜLDER, Ö. L. 1984. Correlations of Laminar Combustion Data for Alternative S.I. Engine Fuels. *SAE Technical Paper,* 841000.

H. JASAK, H. G. WELLER & GOSMAN, A. D. 1999. High resolution NVD differencing scheme for arbitrarily unstructured meshes. *International Journal for Numerical Methods in Fluids,* 31, 431-449.

HAWKES, E. R. & CANT, R. S. 2000. A flame surface density approach to large-eddy simulation of premixed turbulent combustion. *Proceedings of the Combustion Institute,* 28, 51-58.

HUANG, P. G., COLEMAN, G. N. & BRADSHAW, P. 1995. Compressible turbulent channel flows: DNS results and modelling. *Journal of Fluid Mechanics,* 305, 185-218.

HUNT, J. C. R., WRAY, A. A. & MOIN, P. 1988. Eddies, stream, and convergence zones in turbulence. *Center for Turbulence Report CTR-88,* 193–208.

ISSA, R. I. 1986. Solution of the implicitly discretised fluid flow equations by operator-splitting. *Journal of Computational Physics,* 62, 40-65.

JEONG, J. & HUSSAIN, F. 1995. On the identification of a vortex. *Journal of Fluid Mechanics,* 285, 69-94.

JIMENEZ, J. & MOIN, P. 1991. The minimal flow unit in near-wall turbulence. *Journal of Fluid Mechanics,* 225, 213-240.

JOHANSEN, C. T. & CICCARELLI, G. 2009. Visualization of the unburned gas flow field ahead of an accelerating flame in an obstructed square channel. *Combustion and Flame,* 156, 405-416.

KEATING, A., PIOMELLI, U., BALARAS, E. & KALTENBACH, H.-J. 2004. A priori and a posteriori tests of inflow conditions for large-eddy simulation. *Physics of Fluids,* 16, 4696-4712.

KEMPF, A., KLEIN, M. & JANICKA, J. 2005. Efficient Generation of Initial- and Inflow-Conditions for Transient Turbulent Flows in Arbitrary Geometries. *Flow, Turbulence and Combustion,* 74, 67-84.

KERSTEIN, A. R., ASHURST, W. T. & WILLIAMS, F. A. 1988. Field equation for interface propagation in an unsteady homogeneous flow field. *Physical Review A,* 37, 2728-2731.

KIM, J., MOIN, P. & MOSER, R. 1987. Turbulence statistics in fully developed channel flow at low Reynolds number. *Journal of Fluid Mechanics,* 177, 133-166.

KIM, K. T., LEE, D. H. & KWON, S. 2006. Effects of thermal and chemical surface–flame interaction on flame quenching. *Combustion and Flame,* 146, 19-28.

KLEIN, M., SADIKI, A. & JANICKA, J. 2003. A digital filter based generation of inflow data for spatially developing direct numerical or large eddy simulations. *Journal of Computational Physics,* 186, 652-665.

KNIKKER, R., VEYNANTE, D. & MENEVEAU, C. 2002. A priori testing of a similarity model for large eddysimulations of turbulent premixed combustion. *Proceedings of the Combustion Institute,* 29, 2105-2111.

LAW, C. K. 1989. Dynamics of stretched flames. *Symposium (International) on Combustion,* 22, 1381-1402.

LAW, C. K. 2006. *Combustion physics,* Cambridge, Cambridge University Press.

LAW, C. K., ZHU, D. L. & YU, G. 1988. Propagation and extinction of stretched premixed flames. *Symposium (International) on Combustion,* 21, 1419-1426.

LEE, S., LELE, S. K. & MOIN, P. 1992. Simulation of spatially evolving turbulence and the applicability of Taylor's hypothesis in compressible flow. *Physics of Fluids A: Fluid Dynamics,* 4, 1521-1530.

LENORMAND, E., SAGAUT, P. & TA PHUOC, L. 2000. Large eddy simulation of subsonic and supersonic channel flow at moderate Reynolds number. *International Journal for Numerical Methods in Fluids,* 32, 369-406.

LI, J., ZHAO, Z., KAZAKOV, A. & DRYER, F. L. 2004. An updated comprehensive kinetic model of hydrogen combustion. *International Journal of Chemical Kinetics,* 36, 566-575.

LIBBY, P. A. & WILLIAMS, F. A. 1994. *Turbulent reacting flows,* London, Academic.

LUND, T. S., WU, X. & SQUIRES, K. D. 1998. Generation of Turbulent Inflow Data for Spatially-Developing Boundary Layer Simulations. *Journal of Computational Physics,* 140, 233-258.

MADHAVRAO, V. C., J. X. WEN & LUO, K. H. 2011. Numerical modelling of flamelet – wall interaction in combustion large eddy simulation. *European Combustion Meeting 2011.* Cardiff.

MAJDA, A. & SETHIAN, J. 1985. The Derivation and Numerical Solution of the Equations for Zero Mach Number Combustion. *Combustion Science and Technology,* 42, 185-205.

MANHART, M., PELLER, N. & BRUN, C. 2008. Near-wall scaling for turbulent boundary layers with adverse pressure gradient. *Theoretical and Computational Fluid Dynamics,* 22, 243-260.

MARBLE, E. F. & BROADWELL, E. J. 1977. The Coherent Flame Model for Turbulent Chemical Reactions. TRW-29314-6001-RU-00. Project SQUID (Purdue University).

MATHEY, F., COKLJAT, D., BERTOGLIO, J. P. & SERGENT, E. 2006. Assessment of the vortex method for Large Eddy Simulation inlet conditions. *Progress in Computational Fluid Dynamics, an International Journal,* 6, 58-67.

MELLEN, C. P., FROHLICH, J. & RODI, W. 2000. Large eddy simulation of the flow over a periodic hill. *16th IMACS World Congress.* Lausanne.

MENEVEAU, C. & POINSOT, T. 1991. Stretching and quenching of flamelets in premixed turbulent combustion. *Combustion and Flame,* 86, 311-332.

METGHALCHI, M. & KECK, J. C. 1980. Laminar burning velocity of propane-air mixtures at high temperature and pressure. *Combustion and Flame,* 38, 143-154.

MOIN, P. & KIM, J. 1982. Numerical investigation of turbulent channel flow. *Journal of Fluid Mechanics,* 118, 341-377.

MÖLLER, S. I., LUNDGREN, E. & FUREBY, C. 1996. Large eddy simulation of unsteady combustion. *Symposium (International) on Combustion,* 26, 241-248.

MOSER, R. D., KIM, J. & MANSOUR, N. N. 1999. Direct numerical simulation of turbulent channel flow up to Re[sub tau] = 590. *Physics of Fluids,* 11, 943-945.

MUCKETT, M. & FURNESS, A. 2007. *Introduction to Fire Safety Management*, Taylor & Francis.

OPENFOAM. 2014. www.openfoam.org [Online]. [Accessed].

PATANKAR, S. V. 1980. *Numerical heat transfer and fluid flow,* Washington : New York, Hemisphere Pub. Corp. ; McGraw-Hill.

PERIC, M. & FERZIGER, J. H. 2002. *Computational methods for fluid dynamics,* Berlin ; New York, Springer.

PETERS, N. 1988. Laminar flamelet concepts in turbulent combustion. *Symposium (International) on Combustion,* 21, 1231-1250.

PETERS, N. 1999. The turbulent burning velocity for large-scale and small-scale turbulence. *Journal of Fluid Mechanics,* 384, 107-132.

PETERS, N. 2000. *Turbulent combustion,* Cambridge, Cambridge University Press.

PIOMELLI, U. 2008. Wall-layer models for large-eddy simulations. *Progress in Aerospace Sciences,* 44, 437-446.

PIOMELLI, U. & BALARAS, E. 2002. WALL-LAYER MODELS FOR LARGE-EDDY SIMULATIONS. *Annual Review of Fluid Mechanics,* 34, 349-374.

POINSOT, T. & VEYNANTE, D. 2005. *Theoretical and numerical combustion,* Philadelphia, Edwards.

POINSOT, T., VEYNANTE, D. & CANDEL, S. 1991. Quenching processes and premixed turbulent combustion diagrams. *Journal of Fluid Mechanics,* 228, 561-606.

POINSOT, T. J., HAWORTH, D. C. & BRUNEAUX, G. 1993. Direct Simulation and Modeling of Flame-Wall interaction for premixed turbulent combustion. *Combustion and Flame,* 95, 118-132.

POINSOT, T. J. & LELEF, S. K. 1992. Boundary conditions for direct simulations of compressible viscous flows. *Journal of Computational Physics,* 101, 104-129.

POPE, S. B. 1988. The evolution of surfaces in turbulence. *International Journal of Engineering Science,* 26, 445-469.

POPE, S. B. 2000. *Turbulent Flows.*

RHIE, C., M., & CHOW, W., L. 1983. A Numerical Study of the Turbulent Flow Past and Isolated Airfoil with Tailing Edge Separation. *AIAA Journal,* Vol 21, p1525-1532, 1983.

RICHARD, S., COLIN, O., VERMOREL, O., BENKENIDA, A., ANGELBERGER, C. & VEYNANTE, D. 2007. Towards large eddy simulation of combustion in spark ignition engines. *Proceedings of the Combustion Institute,* 31, 3059-3066.

RIVAS, M., HIGELIN, P., CAILLOL, C., SENAME, O., WITRANT, E. & TALON, V. 2011. Validation and Application of a New 0D Flame/Wall Interaction Sub Model for SI Engines. *SAE Int. J. Engines 5(3).* Society of Automotive Engineers.

ROBERTS, T. A., M. ROYLE, D. WILLOUGHBY & KERR, D. 2005. Hazards associated with dispensing hydrogen fuel at retail service stations: Premixed hydrogen-air with cylinder congestion and wall confinement. Derbyshire: Health and Safety Laboratory.

RUDY, D. H. & STRIKWERDA, J. C. 1981. Boundary conditions for subsonic compressible Navier-Stokes calculations. *Computers & Fluids,* 9, 327-338.

RYMER, G. 2001. *Analyse et modelisation du taux de réaction moyen et des mécanismes de transport en combustion turbulente premelangee.* Phd thesis.

SCHOPPA, W. & HUSSAIN, F. 2000. Coherent structure dynamics in near-wall turbulence. *Fluid Dynamics Research,* 26, 119-139.

SCHUMANN, U. 1975. Subgrid scale model for finite difference simulations of turbulent flows in plane channels and annuli. *Journal of Computational Physics,* 18, 376-404.

SEHGAL, B. R. 2012. *Nuclear Safety in Light Water Reactors: Severe Accident Phenomenology*, Elsevier/Academic Press.

SIMPSON, R. L. 1983. A model for the backflow mean velocity profile. *AIAA Journal,* 21, 142-143.

SLOANE, T. M. & RATCLIFFE, J. W. 1982. A molecular beam mass spectrometer study of side-wall flame quenching at low pressure by cooled noncatalytic and catalytic surfaces. *Combustion and Flame,* 47, 83-92.

SPALART, P. R. 2000. Strategies for turbulence modelling and simulations. *International Journal of Heat and Fluid Flow,* 21, 252-263.

SPALDING, D. B. 1961. A Single Formula for the "Law of the Wall". *Journal of Applied Mechanics,* 28, 455-458.

TABOR, G. & WELLER, H. G. 2004. Large Eddy Simulation of Premixed Turbulent Combustion Using e Flame Surface Wrinkling Combustion Model. *Flow, Turbulence and Combustion,* 72, 1-27.

TABOR, G. R. & BABA-AHMADI, M. H. 2010. Inlet conditions for large eddy simulation: A review. *Computers & Fluids,* 39, 553-567.

TAYEBI, B., GALIZZI, C., LEONE, F. J. & FESCUDIE, D. 2007. Experimantal study of the flame-wall interaction. *Third European Combustion Meeting (ECM).*

TEMMERMAN, L., LESCHZINER, M. A., MELLEN, C. P. & FRÖHLICH, J. 2003. Investigation of wall-function approximations and subgrid-scale models in large eddy simulation of separated flow in a channel with streamwise periodic constrictions. *International Journal of Heat and Fluid Flow,* 24, 157-180.

TOUBER, E. & SANDHAM, N. 2009. Large-eddy simulation of low-frequency unsteadiness in a turbulent shock-induced separation bubble. *Theoretical and Computational Fluid Dynamics,* 23, 79-107.

TROUVE, ARNAUD & POINSOT, T. 1994. The evolution equation for the flame surface density in turbulent premixed combustion. *Journal of Fluid Mechanics,* 278, 1-31.

VELOUDIS, I., YANG, Z., MCGUIRK, J. J., PAGE, G. J. & SPENCER, A. 2007. Novel Implementation and Assessment of a Digital Filter Based Approach for the Generation of LES Inlet Conditions. *Flow, Turbulence and Combustion,* 79, 1-24.

VENDRA, C. M. R., WEN, J. X. & TAM, V. H. Y. 2013. Numerical simulation of turbulent flame–wall quenching using a coherent flame model. *Journal of Loss Prevention in the Process Industries,* 26, 363-368.

WELLER, H. G., TABOR, G., GOSMAN, A. D. & FUREBY, C. 1998a. Application of a flame-wrinkling les combustion model to a turbulent mixing layer. *Symposium (International) on Combustion,* 27, 899-907.

WELLER, H. G., TABOR, G., JASAK, H. & FUREBY, C. 1998b. A tensorial approach to computational continum mechanics using object oriented techniques. *Computers in Physics,* 12.

WERNER, H. & WENGLE, H. 1993. Large-Eddy Simulation of Turbulent Flow Over and Around a Cube in a Plate Channel. *In:* DURST, F., FRIEDRICH, R., LAUNDER, B., SCHMIDT, F., SCHUMANN, U. & WHITELAW, J. (eds.) *Turbulent Shear Flows 8.* Springer Berlin Heidelberg.

WICHMAN, I. S. & BRUNEAUX, G. 1995. Head-on quenching of a premixed flame by a cold wall. *Combustion and Flame,* 103, 296-310.

WILLIAMS, F. A. 1985. *Combustion theory : the fundamental theory of chemically reacting flow systems,* Menlo Park, Calif., Benjamin/Cummings Pub. Co.

XIE, Z.-T. & CASTRO, I. 2008. Efficient Generation of Inflow Conditions for Large Eddy Simulation of Street-Scale Flows. *Flow, Turbulence and Combustion,* 81, 449-470.

YOSHIZAWA, A. & HORIUTI, K. 1985. A Statistically-Derived Subgrid-Scale Kinetic Energy Model for the Large-Eddy Simulation of Turbulent Flows. *Journal of the Physical Society of Japan,* 54, 2834-2839.